

Structural determination of molecular adsorbates and 2D materials on metal surfaces using X-ray Standing Waves and Photoelectron Diffraction

Leon B. S. Williams

School of Chemistry
College of Science and Engineering



diamond



**University
ofGlasgow**

Placement Supervisor: Dr. David A. Duncan
University Supervisor: Prof. Malcolm Kadodwala

September 15 , 2022

Abstract

Two-dimensional (2D) materials have been at the forefront of materials research, owing to their unique and potentially powerful properties that have promise in fields ranging from nanoscale electronics, to single atom catalysis. The I09 beamline at Diamond Light Source is a one-of-a-kind laboratory, exploiting synchrotron radiation to study the various properties and structures of surfaces and interfaces under ultra-high vacuum (UHV) conditions. The work described in this report involved the investigation of epitaxial growth of azupyrene and pyrene on Cu(111) for the synthesis of graphene, and epitaxially grown molybdenum disulfide (MoS_2) on Au(111), using various surface analytical techniques including: low energy electron diffraction (LEED), normal incidence X-ray standing waves (NIXSW), energy-scanned photoelectron diffraction (PhD), scanning tunneling microscopy (STM), and X-ray photoelectron spectroscopy (XPS). The data for this was acquired by the Surfaces and Interfaces group with the I09 beamline at Diamond Light Source, some of which was taken during my time working there.

The study of the growth of azupyrene and pyrene on Cu(111) single crystal at varying crystal temperatures compares the differences in growth mechanism between an alternant (pyrene) and a non-alternant (azupyrene) reagent. LEED analysis revealed synthesis of graphene at 970 K for azupyrene, and 870 - 1070 K for pyrene. Furthermore, the study allowed for categorisation of growth stages for azupyrene into molecular (~ 300 K), dendritic (~ 820 K), 2D islands (~ 870 K), and ideal graphene (~ 970 K). Preparations of pyrene at similar crystal temperatures were also produced. The two sets of preparations were then compared using NIXSW, STM, and XPS, revealing key differences in the growth mechanisms of the two molecules. Key differences between the two include include; large changes in electronic structure and adsorption height for azupyrene, but minimal changes in these properties during the growth of pyrene. Furthermore, the existence of suspected pyrene trimers in high crystal temperature preparations was seen.

The investigation of epitaxially grown MoS_2 on Au(111) applied PhD for structural determination. This study revealed a lack of substantial correlation between full structure models of 1T and 1H configuration MoS_2 with the experimental PhD spectra; indicating an incomplete-

ness in the model. This was suggested to be a consequence of not including any corrugation of the surface within the model. This corrugation was identified in a separate study investigating the existence of a Moire superstructure in this system[1]. Further improvements in correlation were made through simplification of the model to trimer and hexamer base units, in an attempt to understand the fundamental structural parameters (i.e. bond lengths, and angles). These revealed an inconsistency between the models and literature values; implying the models did not match the reality of the system, and may be too simplistic. Possible constraints that may be preventing models from matching the experimental system include: existence of heterostructures, composed of varying configuration of MoS_2 within the sample; the aforementioned Moire superstructures; and other restrictions placed on the model erroneously.

Acknowledgements

Over the past 12 months working at Diamond Light Source, I have had the pleasure of meeting and working with a number of brilliant and supportive people who have helped make the time I spent here invaluable to both my personal growth and career. Specifically, I'd like to thank:

- David Duncan for his fundamental contribution in all the research I was involved in, and acting as a bank of knowledge for my scientific questions and many other areas.
- Matthew Stoodley, and Benedikt Klein who took part in all of the experimental work I was involved in, for showing me the ropes of the various techniques and UHV, for helping redraft reports and advise on various topics, and finally for supporting me throughout the numerous long and late beamtimes spent at Harwell.
- Tien Lin Lee who designed and pioneered the I09 beamline, and who remained cheerful on all occasions
- The technicians, Dave and Dave, for maintaining the most well kept beamline at Diamond Light Source
- The rest of the Solids and Surfaces research group who made me feel welcome and took the time out of their working hours to teach me how everything worked and for being patient with a newcomer to their field.
- The students in the Solids and Surfaces student office who provided endless entertainment, support, and friendship over the year.
- The student engagement team, who made the transition from student to working employee much more comfortable, and supported all the students throughout the year with any problems that arose.

In addition to those who have helped enrich my experience at Diamond, I would also like to thank those that made my year, living in Oxford, so enjoyable. These include the Ultimate frisbee team that I trained, and made life-long friends with in Oxford, my uncle, Peter, and his partner, Lynn, who supported me throughout the year and made Oxford feel like home, and

last but certainly not least, the other placement students who were my companions throughout the year.

Declarations

The work presented in this thesis was performed at Diamond Light Source with the Surfaces & Interfaces group, at I09 specifically; concerning the analysis and interpretation of XPS, NIXSW, STM, and LEED experimental data measured by Dr. David A. Duncan¹, Dr. Benedikt Klein^{1,2}, Matthew Stoodley^{1,2} and I^{1,3}, also with collaborators. The data, conclusions and procedures described in **Chapter 4** are the accumulation of 2.5 years of research in an ongoing project involving the aforementioned staff at I09, and collaborators, some of which was acquired during my time working with this group. The data that was measured outwith my time includes: the data of XPS spectrum a) of **Figure 4.8 & 4.9**, and NIXSW spectra a), b), and c) of **Figure 4.10**. Furthermore, the data being studied in **Chapter 5** was acquired before my time at Diamond Light Source, in parallel to a separate study of *MoS₂* [1].

¹ - associated with Diamond Light Source Ltd

² - associated with University of Warwick

³ - associated with University of Glasgow

Leon Baiyu Shen Williams

Contents

1	Introduction	3
1.1	2D Materials/Nanomaterials	3
2	Theory	5
2.1	Ultra High Vacuum	5
2.1.1	Pressure Gauges	8
2.1.2	Pumping	8
2.2	I09	10
2.2.1	I09 End-station	11
3	Experimental and Supporting techniques	13
3.0.1	Inelastic Mean Free Path and the Universal Curve	13
3.1	Low Energy Electron Diffraction	15
3.2	X-ray Photoelectron Spectroscopy	17
3.2.1	Quantum Mechanical Approach	19
3.2.2	Data Acquisition and Reduction	22
3.2.3	Photon source for XPS	25
3.3	Normal Incidence X-ray Standing Waves	27
3.3.1	Mechanism of XSW	29
3.3.2	Data Acquisition and Reduction of NIXSW	33
3.4	Energy-scanned Photoelectron Diffraction (PhD)	34
3.4.1	Principles of PhD	34
3.4.2	Qualitative Information	38
3.4.3	Multiple-Scattering Calculations	38
3.4.4	Data Acquisition & Processing	41
3.4.5	Assessing & Finding the best fit	42
3.4.6	Particle Swarm Optimisation (PSO)	44
3.5	Scanning Tunnelling Microscopy	45
3.5.1	Moire Patterns in STM	47

4 Azupyrene and Pyrene on Cu(111) for graphene	48
4.1 Introduction	48
4.2 Methods	56
4.2.1 Equipment	56
4.2.2 Synthesis Procedure	56
4.2.3 Analysis Techniques	57
4.3 Results & Discussion	58
4.3.1 Molecular	61
4.3.2 Dendritic	62
4.3.3 2D Islands/Intermediate	64
4.3.4 Ideal Graphene/Graphene	66
4.3.5 Conclusions	70
5 PhD Structure Determination of MoS_2 on Au(111)	72
5.1 Introduction	72
5.1.1 Molybdenum Disulfide	73
5.1.2 Polyptism of Molybdenum Disulphide	73
5.1.3 Synthesis of MoS_2	75
5.1.4 Epitaxial Growth of MoS_2 on Au(111)	76
5.2 Methods	76
5.2.1 Experimental Details	76
5.3 Results & Discussion	78
5.3.1 Previous Study	78
5.3.2 Computational Aspects	78
5.3.3 Qualitative Analysis	78
5.3.4 Particle swarm optimisation parameters	81
5.3.5 Full Structure with Au(111) Substrate	81
5.3.6 1T and 1H Full structure without Au(111) substrates	83
5.3.7 Simple Model - Trimer	85
5.3.8 Hexamers	87
5.3.9 Conclusions	92
A PhD Chapter Supporting Information	95

List of Figures

2.1	Diagram of mechanism of scroll pump. Depicting gas (blue) being compressed against the inner wall of the static spiral (dark grey) by the rotating spiral (light grey), eventually into the central release valve [2].	9
2.2	Partial schematic diagram depicting the fundamental components making up the I09 EH2 UHV chamber. Note that this only includes primary components of the system [3].	11
3.1	Universal curve depicting the IMFP for typical elements utilising equation 3.2, with A = 143, and B = 0.054 [4].	14
3.2	Setup of a LEED experiment depicting electron gun on (left) firing low energy electrons at a sample, off which the electrons diffract towards the hemispherical fluorescent screen which is shielded by EM grids, often used for retarding low energy electrons.	15
3.3	Image of LEED pattern of graphene on Cu(111), depicting copper lattice spots with characteristic graphene arc. Image was taken at 150 eV [5].	16
3.4	Diagram of the process of photoemission during XPS, depicting an incident photon of energy, $h\nu$, exciting a core level electron of binding energy, E_B , surpassing the work function, Ψ , between the vacuum level, E_v , and the fermi level, E_f , emitted with kinetic energy, KE.	17
3.5	Example C 1s XPS spectrum of monolayer naphthalene and azulene on copper(111)[6].	18
3.6	Diagram of Gaussian (blue), Lorentzian (green), and Voigt (red) lineshapes [7].	24
3.7	Energy level diagram depicting two types transitions involved in core hole filling. The left diagram depicts emission of a photon as a result of core hole filling, and the right diagram shows Auger emission.	26

3.8 Left diagram of X-ray standing wave pattern, showing nodal planes of plane waves for incoming and reflected X-ray waves with respect to the positions of the atoms in the bulk, along with the intensity of the resulting XSW wave pattern formed from the incident and reflected waves. The right hand diagram depicts the reflectivity curve of a bulk crystal, also known as a Darwin curve, and the absorption profiles one would measure for species sitting at bulk and interstitial sites within the lattice as one scans through Bragg condition [8].	27
3.9 Diagram depicting the reflectivity profile for bulk absorption (red) and absorption profiles for atoms located at various points relative to scattering planes of a Cu(111) crystal. Instrumental broadening effects are not included in calculations [8]	30
3.10 Diagram of various scattering pathways involved in PhD scattering calculations, depicting an incident photon the emitter atom (purple), and the various scattering pathways of the photoemitted electron by neighbouring atoms(yellow) [9].	35
3.11 Diagram showing the a) 180° backscattering geometry between the Detector, emitter atom (blue), and the scatterer atom (grey), along with a PhD modulation for that geometry and b) highlighting the effect of a slight 20° skew on this geometry on the shape of the resulting PhD modulation.	37
3.12 Plot of EDC intensity with respect to photoelectron kinetic energy. This being the first step in processing of raw PhD data[10].	39
3.13 Plot of background-adjusted PhD modulation with fitted stiff spline (upper diagram), and final PhD modulation with spline subtracted depicting only diffractive effects [10].	41
3.14 Diagram of the measurement of an STM linescan in a) constant height mode, and in b) constant current mode, along with the resulting plot of the 2D linescan from the respective method to their right.	46
4.1 Plot depicting specific reactivity of catalyst versus catalyst dispersion, alongside the relationship between dispersion of catalyst with influence of substrate [11].	49
4.2 The Fermi surface of graphene in a nearest neighbour tight-binding model [12, 13]	50
4.3 Diagrams of the structures of azupyrene and pyrene molecules.	51
4.4 Depiction of different types of some of the types of possible defects in graphene. a) Single Vacancy. b) Stone-Wales Defect. c) 5-8-5 MV. d) 555-777 MV. e) 5555-6-7777 MV [14]	54

4.5 LEED images of azupyrene and pyrene produced graphene displaying the characteristic graphene arc surrounding the Cu (111) reciprocal lattice points [5].	58
4.6 STM of a 2D Island preparation of graphene from Azupyrene at 870 K. Image was taken at 1 V, with a current of 1 nA. a) Improved contrast image of moire pattern from graphene.	59
4.7 STM of a molecular preparation of graphene from pyrene between 870 K and 1070 K. Image was taken at 1.5 V, with a current of 0.3 nA.	60
4.8 Comparison of soft XPS C 1s peaks and their sub-peaks for different temperature preparations at different stages of growth of graphene from azupyrene.	63
4.9 Comparison of soft XPS C 1s peaks and their sub-peaks for different temperature preparations at different stages of growth of graphene from pyrene.	64
4.10 NIXSW of different stages of growth of graphene from Azupyrene. a) Molecular sample peak 1(Room Temperature). b) Molecular sample peak 2(Room Temperature). c) Dendritic sample (820 K). d) 2D Island (870 K). e) Ideal graphene (973 K).	68
4.11 NIXSW of different stages of growth of graphene from Azupyrene. a) Molecular sample (Room Temperature). b) Dendritic sample (820 K). c) 2D Island (870 K).	69
5.1 Diagrams of 1H and 1T configurations of MoS_2	74
5.2 Bandgap diagrams for 1H and 1T configurations of MoS_2	75
5.3 Pure PhD modulations for S 1s emission. Polar angle is denoted along the y axis of each modulation, whilst the azimuthal angle/crystallographic direction is denoted atop the columns of the plots.	79
5.4 Pure PhD modulations for Mo 2p emission. Polar angle is denoted along the y axis of each modulation, whilst the azimuthal angle/crystallographic direction is denoted atop the columns of the plots.	79
5.5 Pure PhD modulations for Mo 2p emission with 40 - 150 eV removed. Polar angle is denoted along the y axis of each modulation, whilst the azimuthal angle/crystallographic direction is denoted atop the columns of the plots.	80
5.6 Example rhombohedral unit cell with side lengths a, b, and c, with angles α , β , and γ between them. This type of unit cell was used to define the full structure models for MoS_2 1H and 1T, as well as the gold substrate.	81
5.7 PSO optimised structure of 1H full structure on Au(111) substrate from different perspectives: a) Vertical, b) Side	82

5.8 PhD modulations of PSO optimised structure of 1H full structure on Au(111) substrate overlayed onto experimental modulations of S (yellow) and Mo (blue) at varying polar angle (y label) and crystallographic direction (x label).	83
5.9 Optimised full structures of 1T and 1H configurations of MoS_2	84
5.10 Diagram of trimer model, along with key parameters of the model: Upper sulfur bond length, R_1 , lower sulfur bond length, R_2 , and bond angle, θ	85
5.11 PSO optimised structure of trimer model from different perspectives a) Rear, b) Vertical, c) Side	86
5.12 Diagram of hexamer 1H model, with perspectives from the a) Z axis (Vertical), b) Y axis (Side), and c) X axis (End), denoting key parameters of the model.	87
5.13 PSO optimised structure of 1H hexamer structure from different perspectives: a) End, b) Side, c) Vertical.	88
5.14 2D colour map of R-factors for angles of upper and lower S atoms for the 1H hexamer model, where theta of the upper S atom is θ_1 , and for the lower S atom, θ_2 , in the 1H hexamer model diagram of Figure 5.12 . 2D slices at the minimum R-factor of the two angles can be found in the Appendix. The other parameters for this model were that of the PSO optimised values including: a Mo-Mo separation of 3.34 Å, and bond lengths of 1.70 Å and 1.66 Å for lower and upper sulfurs, respectively	90
5.15 2D colour map of R-factors for radii of upper and lower S atoms for the 1H hexamer model, where the radii for the upper S is R_1 , and the lower S R_2 in the hexamer model diagram of Figure 5.12 . 2D slices at the minimum R-factor of the two radii can be found in the Appendix. The other parameters for this model were that of the PSO optimised values including: a Mo - Mo separation of 3.34 Å, and a bond angle of 174°.	90
5.16 Plot of R-Factor with respect to Mo - Mo separation for the 1H hexamer model, where Mo-Mo separation is ΔMo in the hexamer model diagram of Figure 5.12 . The other parameters for this model were a bond angle of 174°, and bond lengths of 1.70 Å and 1.66 Å for lower and upper sulfurs, respectively	91
5.17 Diagram of hexamer 1T model, with perspectives from the a) Z axis (Vertical), b) Y axis (Side), and c) X axis (End), denoting key parameters of the model.	91
5.18 PSO optimised structure of 1T hexamer structure from different perspectives: a) End, b) Side, c) Vertical.	92

A.1	PhD modulations of PSO optimised structure of 1H full structure overlayed onto experimental modulations of molybdenum at varying polar angle (y label) and crystallographic direction (x label).	95
A.2	PhD modulations of PSO optimised structure of 1T full structure overlayed onto experimental modulations of molybdenum at varying polar angle (y label) and crystallographic direction (x label).	96
A.3	PhD modulations of PSO optimised structure of the <i>MoS₂</i> trimer overlayed onto experimental modulations of molybdenum at varying polar angle (y label) and crystallographic direction (x label).	96
A.4	PhD modulations of PSO optimised structure of 1H hexamer overlayed onto experimental modulations of molybdenum at varying polar angle (y label) and crystallographic direction (x label).	97
A.5	PhD modulations of PSO optimised structure of 1T hexamer overlayed onto experimental modulations of molybdenum at varying polar angle (y label) and crystallographic direction (x label).	97
A.6	Diagram showing the section of the 1H full structure that is modelled by the 1H hexamer	98
A.7	Diagram showing the section of the 1T full structure that is modelled by the 1T hexamer	98
A.8	Plot of R-Factor with respect to lower S radius for the 1H hexamer model, where S lower radius is R_2 within the hexamer model diagram of Figure 5.12 . The other parameters for this model were a bond angle of 174°, a Mo - Mo separation of 3.34 Å, and a bond length of 1.70 Å for upper sulfurs.	98
A.9	Plot of R-Factor with respect to upper S radius for the 1H hexamer model, where S lower radius is R_2 within the hexamer model diagram of Figure 5.12 . The other parameters for this model were a bond angle of 174°, a Mo - Mo separation of 3.34 Å, and a bond length of 1.66 Å for lower sulfurs.	99
A.10	Plot of R-Factor with respect to lower S angle for the 1H hexamer model, where theta lower is θ_2 within the hexamer model diagram of Figure 5.12 . The other parameters for this model were a upper S angle of 95°, a Mo - Mo separation of 3.34 Å, and a bond length of 1.66 Å for lower sulfurs.	99
A.11	Plot of R-Factor with respect to upper S angle for the 1H hexamer model, where theta upper is θ_1 within the hexamer model diagram of Figure 5.12 . The other parameters for this model were a lower S angle of 280°, a Mo - Mo separation of 3.34 Å, and a bond length of 1.66 Å for lower sulfurs.	100

List of Tables

4.1	Table of fitted azupyrene XPS peak parameters. The respective spectra and peaks can be found in Figure 4.8	65
4.2	Table of fitted pyrene XPS peak parameters. The respective spectra and peaks can be found in Figure 4.9	65
4.3	Table of azupyrene XSW Results for different growth stages.	67
4.4	Table of Pyrene XSW Results for different growth stages.	67
5.1	Table of model parameters from optimisation of PhD modulations of full structure 1H on Au(111) compared to literature values from various sources. No literature parameters are of MoS_2 on gold(111) substrate.	82
5.2	Table of model parameters from optimisation of PhD modulations of full structure 1H compared to literature values from various sources. No literature parameters are of MoS_2 on gold(111) substrate.	84
5.3	Table of model parameters from optimisation of PhD modulations of full structure 1T compared to literature values from various sources. No literature parameters are of MoS_2 on gold(111) substrate.	85
5.4	Table of model parameters from optimisation of PhD modulations of trimers compared to literature values from various sources. No literature parameters are of MoS_2 on gold(111) substrate.	86
5.5	Table of model parameters from optimisation of PhD modulations of 1H hexamer compared to literature values from various sources. No literature parameters are of MoS_2 on gold(111) substrate.	88
5.6	Table of model parameters from optimisation of PhD modulations of 1T hexamer compared to literature values from various sources. No literature parameters are of MoS_2 on gold(111) substrate.	92

Abbreviations

- ARPES: Angle resolved photoelectron spectroscopy

- DCM: Double-crystal monochromator
- DFT: Density functional theory
- DLS: Diamond Light Source Ltd
- EXAFS: Extended X-ray absorption fine structure
- FWHM: Full width half maximum
- HAXPES: Hard X-ray photoelectron spectroscopy
- IMFP: Inelastic mean free path
- LEED: Low energy electron diffraction
- MBE: Molecular beam epitaxy
- ML: Mono-layer
- NIXW: Normal incidence X-ray standing wave
- PhD: Photoelectron diffraction
- PSO: Particle swarm optimisation
- SAC: Single atom catalysis
- SEXAFS: Surface-extended X-ray absorption fine structure
- SPC: Surface preparation chamber
- STS: Scanning tunneling spectroscopy
- STM: Scanning tunneling microscopy
- SXPS: Soft X-ray photoelectron spectroscopy
- UHV: Ultra-high vacuum
- XPD: X-ray photoelectron diffraction
- XPS: X-ray photoelectron spectroscopy
- XSW: X-ray standing wave

Chapter 1

Introduction

1.1 2D Materials/Nanomaterials

Since the turn of the century, after the discovery of the existence 0 dimensional fullerenes[15] and 1D carbon nanotubes[16], then later success in producing 2D graphene[17], there has been an explosion of interest into 2D materials both in academia and industry. The fascination has been maintained with numerous developments both in discovery of new 2D materials such as Transition Metal Dichalcogenides (TMDCs)[18], Hexagonal boron nitride (HBN), and the X-enes[19]. What makes this class of material so attractive is their unique properties as a result of their restriction in 1D. For example, in 2D materials, electrons become confined to in-plane movement, and their band structures are altered by lack of interlayer interactions that exist in their bulk and, to a lesser extent multilayer forms. This substantially alters their optical and electronic properties relative to these alternate forms[20], providing properties unique to this type of structure. Furthermore, 2D materials have differing geometry, and significantly greater surface to bulk ratio, that can also have a strong effect on their chemical properties[21].

The majority of 2D material research has been carried out on graphene, due to its remarkable electronic, mechanical, and chemical properties. Many proponents propose to replace the prominent silicon semiconductor technology, with the aim of utilising graphene's high carrier mobility, which could substantially speed up computing times through low loss, high frequency operation[19]. However, without an intrinsic bandgap required for use in semiconductor electronics, such as transistors, it cannot replace silicon in this regard. One solution to this has been the possibility of functionalisation or other alterations to change the electronic band structure, for example, through application of strain or twisting [22]. Subsequent to graphene's discovery and realisation of existence of 2D materials, interest and research into other 2D materials blossomed. Many of these have widely varying band structures, whilst sharing some of the common features of 2D materials such as transparency, flexibility, and

mechanical strength. The band structures of many inorganic materials, when converted into single layers have shown intriguing changes in optical properties[18]; with shifts in properties with numbers of layers such as electronic band structure structure shifts, resulting in colour shifts, changes in photoluminescence and fluorescence to name a few. Another interesting aspect of 2D materials lies in the change in reactivity, and physico-chemical properties, such as the way molecules adsorb and bind to the surface, but also mechanisms of surface plasmon resonance. To exploit the properties of these materials, much more research is required; including that to understand their features and mechanisms and the methods used to synthesise them, with the purpose of providing knowledge to apply them effectively at later stages in their development [19, 23]. The aforementioned electronic structure and properties come part and parcel with the physical structure itself, thus it is vital to study these. These are the driving forces behind the research carried out in this thesis, involving structural analyses of various 2D materials utilising surface techniques including LEED, XPS, PhD, NIXSW, STM, some of which are unique to the I09 beamline at Diamond Light Source where the majority of this research was carried out.

Chapter 2

Theory

2.1 Ultra High Vacuum

The study of surface science utilises techniques that probe atomic scale structure and properties. This is dependent on a well-characterised interface of consistent structure and a clean environment to allow analytical techniques to function correctly. Electron spectroscopies, for example, are notably affected by higher pressures through higher impingement rate and shorter mean free path. To reduce impact of this, ultra high vacuum (UHV) systems are typically utilised. The effect of this can be understood by a fundamental analysis of flux of particles from atmosphere on a surface, through kinetic theory of gases [2, 24]. This gives a rate of arrival of these particles as:

$$r_a = \frac{1}{4} \rho \bar{v}, \quad (2.1)$$

where \bar{v} is average velocity of particles, and ρ is particle density. Taking the kinetic energy of the particle as $\frac{k_B T}{2}$ per degree of freedom, at temperature, T , and relating it to kinetic energy, one gets an expression for the root mean square velocity, v_{rms} , of:

$$v_{rms}^2 = \frac{3k_B T}{m}, \quad (2.2)$$

where m is the mass of the particle, and the particle has 3 degrees of freedom. This can be related to average velocity through:

$$\bar{v} = \sqrt{\frac{8}{3\pi}} v_{rms}. \quad (2.3)$$

Whilst pressure can also be defined as:

$$P = \rho k_B T, \quad (2.4)$$

which can be combined with **Equation 2.1**, one gets the expression:

$$r_a = P \sqrt{\frac{1}{2\pi k_B T m}}. \quad (2.5)$$

Assuming P in mbar, T in Kelvin, and converting m to molecular weight, M, one arrives at the expression for rate of arrival in $cm^{-2}s^{-1}$:

$$r_a = 4.67 \times 10^{22} \frac{P}{\sqrt{TM}}. \quad (2.6)$$

Considering a room temperature experimental chamber at relatively low pressure of 10^{-6} mbar of N_2 ; the predicted arrival rate is 4×10^{14} molecules $cm^{-2}s^{-1}$. Supposing that monolayer exposure is 10^{15} atoms cm^{-2} , then it would take several seconds for monolayer exposure. At lower pressures of 10^{-9} mbar, it would take 30 mins to do so, at atmospheric pressure of ≈ 1000 mbar, on the other hand, it would take 1 nanosecond. It is clear that interactions between the surface are inevitable to occur, even at relatively low pressures. It is for this reason that great effort must be made to maintain a UHV system, pressures of which tend to be around $10^{-9} - 10^{-11}$ depending on the requirements of the system [24, 25].

Initial UHV systems were made from glass due to its surprising strength to withstand low pressures and low outgassing, which, in fact, allowed lower pressures than the metal chambers used commonly today. These were severely flawed in their inherent fragility and single use capacity; a chamber was setup then encased in glass, having to be broken to make any substantial adjustments. As such, modern UHV systems are made from metal, often steel, or an alloy of steel with high magnetic shielding, μ metal, chambers and pipes connected with low vapor pressure rubber or soft metal gaskets paired with knife-edges to reduce leaks between chambers. Once built, the chambers are then pumped down to low pressures gradually with an array of pumps to get the chamber down to UHV pressures. Numerous pumps are attached to a vacuum chamber to acquire and maintain vacuum within the system, constantly pumping molecules out of a chamber until equilibrium between the pumps and the sources of pressure within the chamber. This process can take periods of up to several days due to factors such as outgassing from the chamber components, or worse, there can be leaks in the system that are often nanoscopic and cannot be seen with the human eye. Furthermore, there can exist pockets of gas which cannot be pumped efficiently due to the setup of the system, leaving a system unable to reach low pressures indefinitely. In these cases, easily pumped gases such as argon can be pumped into the system to flush out these pockets of gas. To speed up the pumping process and reach lower pressures more quickly, it is typical to "bake" the chamber. This involves heating the chamber to 100s of degrees C to increase the outgassing rate, from the various materials within the chambers, over the period of up to a few

days to accelerate this process.

In addition to UHV systems needing to be pumped down, the crystals/samples and evaporant (materials for deposition) that are studied within these systems must undergo a similar process. They must placed into a separate chamber, and that chamber must be pumped down to lower pressures, over the course of several hours or even days. After which, they can be opened up, through a valve, into the chamber. To transfer crystals/samples about in vacuum, intricately engineered manipulators must be utilised, whilst maintaining the vacuum. Once finally into the main UHV chamber, their surface must be cleaned from all the debris and contaminants picked up from atmosphere/higher pressures. This is mostly done *in situ* using techniques such as: mechanical cleaving, chemical processing, heating, or most commonly, ion bombardment.

Ion bombardment, typically with Ar^+ ions, is one of the most prominent UHV cleaning methods due to its repeatability, ease-of-use, speed, and ability to remove even strongly bound adsorbates. The process involves opening a clean source of the gas into the UHV, ionising the atoms by colliding them with electrons, then accelerating the resulting ions with an electric field, onto the crystal surface. These high velocity ions then collide with adsorbate and the surface, knocking atoms and molecules off, including those of the surface. This leads to a relatively rough surface that must then be annealed to high temperatures to repair the surface, desorb the impinged argon ions and to outgas the crystal. One might also expect that introducing particles into the vacuum would be harmful to the pressures, however, ions used for this are typically suited for easy pumping by typical UHV pumps.

Regimes of flow

Levels of vacuum are often referred to by their regimes of flow, which describes the kinetic regime that gas particles are in, at different pressures. This is useful to describe the pressures at which different UHV components (e.g. pumps and gauges) are used. The regime of flow is measured by the ratio of the mean free path of an atom, L , and the dimension of the vessel, D . Where $L \ll D$ then flow is described as viscous, as particles are restricting and interacting with each other much more than the vessel. This typically includes pressures of between 1000 and 1 mbar. Whereas, where $L \gg D$ flow is described as molecular, at pressures lower than 10^{-6} . At these pressures, collisions between particles and the sides of a chamber are more prominent than with each other. Between these two regimes is transitional flow where $L \approx D$, with pressures of around 0.1 mbar [2, 24]. It is important to have the distinction as various vacuum equipment functions best or doesn't function at all in different regimes of flow.

2.1.1 Pressure Gauges

Whilst at atmospheric and higher pressures, pressure is typically measured through force as a result of pressure differentials. In vacuum it is not possible to measure pressure this way, due to the much lower number of particles in the atmosphere. Even in different levels of vacuum, pressure must be measured using different types of gauges as there are regimes of flow in which they can function safely and remain accurate. From viscous down to the transitional regimes of flow, a Pirani gauge can be used. It measures pressure through the temperature of a heated filament, indicated by the resistance in the filament. The temperature itself conveys the rate of heat loss due to convective mechanisms which is dependent on the pressure of the gas. Once the pressure is too low, then differences in heat loss becomes too small to measure. Below this range is where the inverted magnetron gauge (IMG), is often utilised. The IMG functions through ionising gas through spiralling electrons in a strong electric and magnetic field. Collision of electrons with molecules produces ions, which are then attracted to a cathode, from which a current can be measured to indicate gas pressure. The collision process also produces more electrons, which further facilitates the ionisation process. These gauges can function from $10^{-4} - 10^{-11}$ mbar, above which, the IMG can be damaged due to an excess of ionising gas. Hot cathode gauges (HCGs) use a similar mechanism to measure pressure in these ranges [2].

2.1.2 Pumping

The range of vacuum pumps varies in mechanism depending on regime of flow for which it is designed. Mechanical pumps or roughing pumps are the most prominent, on a UHV chamber; designed to pump in viscous flow regime, with pumping volumes of around $1m^3$ per hour and can typically pump a system down to $\sim 1 - 10^{-3}$ mbar. These function by compressing a volume of gas above atmospheric pressure such that the gas can be exhausted out of a one-way release valve. An example of these is a scroll pump, which is made up of interlaced spirals, one of which is static, whilst the other rotates around the other. This traps gas against the wall of the static spiral then slowly transports it into the centre where the exhaust valve is located, seen in **Figure 2.1**.

Turbomolecular pumps function in the subsequent regimes of flow, transitional and molecular. These are often used inline with roughing pumps, and are only functional at pressures below 10^{-2} mbar. When paired with roughing pumps, they can acquire pressures of $\sim 10^{-6}$ mbar. These are differential pumps, which function by creating a pressure differential

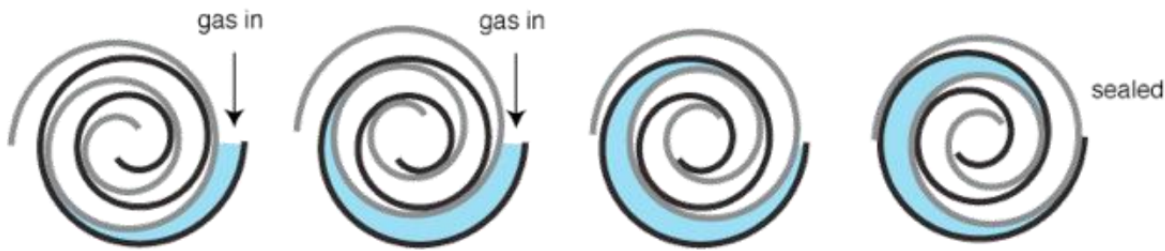


Figure 2.1: Diagram of mechanism of scroll pump. Depicting gas (blue) being compressed against the inner wall of the static spiral (dark grey) by the rotating spiral (light grey), eventually into the central release valve [2].

between the inlet and outlet. Turbo pumps do so using a set of fast moving, angled fan blades which compress gas molecules through the pump, into sets of stationary blades which then deflect molecules down into the next set of rotating blades. These stationary blades also act to prevent backflow. At the rear of the pump is a drag stage that directs pumped molecules out of the outlet. Adjustments can be made to the parameters of the turbo pump such as the fan blade speed and angle, to alter the compression ratio and overall pumping speeds; often specialised for certain molecular weights of gas particles that are common in a specific UHV chamber.

Finally, you have capture pumps which function through capturing gas particles using a reactive metal surface, onto which gas particles adsorb and are impinged until its finite capacity is reached. The most popular of these is the ion pump. Ion pumps can be used between $10^{-4} - 10^{-11}$ mbar (though they shouldn't be used at the upper end of this range as they will rapidly be exhausted) and capture gas through the same mechanism as the IMG, where electrons are fired and put in a spiralling motion by an electric and magnetic fields, ionising gas particles, after which the fields direct them into a reactive titanium cathode which buries or impinges them. The accelerated particles can also sputter titanium ions off, which then coats the surrounding walls and anode, providing more reactive surface to hold gas particles. Meanwhile the additional electrons produced by ionisation, will also be spiralled and undergo further ionisation with other gas particles. This whole process is mirrored in a number of a honeycomb of cells within in the ion pump, multiplying its effect. Titanium sublimation pumps (TSP) are another type of capture pump that is often fired periodically to speed up reduction in vacuum. TSPs utilise the reactivity of titanium, allowing gas to be impinged on the titanium coated walls of the pump. A titanium alloy filament is heated periodically to recoat the internals of the pump with titanium. To fully coat the internals can take a few seconds at 10^{-5} mbar, but will take several hours at low pressures around 10^{-9} mbar. Non-evaporable getter (NEG) pumps are another diffusive pump which functions on the absorption on gas particles into the bulk of a porous metal alloy.

Typical UHV chambers can have a range of different pumps depending on funding for the chamber, pressure requirements, and preferences of the engineers and scientists using them. For example, at the primary end station at I09 of Diamond Light Source, pressures of as low as 10^{-11} mbar are common [2].

2.2 I09

The majority of data shown in this thesis, particularly any PhD, NIXSW, and XPS data, was acquired at the I09 beamline at Diamond Light Source. I09 is rather uniquely a two undulator beamline that provides a selection of two photon energy ranges in soft (100 eV - 1800 eV) and hard (2.1 keV - 20+ keV) X-ray regimes; with both beam spots of size $40 \mu\text{m}$ (hard) and $20 \mu\text{m}$ (soft) aligned to the same spot in the end station. The hard and the soft undulators utilised have magnetic periods of 27 mm and 60 mm, respectively. The ability to quickly alternate between use of hard and soft X-rays is invaluable for surface and interface studies, allowing analysis using various techniques interchangeable during the experimentation period. This is particularly useful when carrying out initial studies of a sample, for example, when calibrating synthesis technique for desired coverages. Soft X-rays are particularly useful for characterisation of surface preparations using XPS, through study of core levels within that energy range. Meanwhile, hard X-rays have wavelengths in the range of scattering plane separations for crystal reflections, this allows higher throughput study of a different facets of surface structure. Hard X-rays, in particular, important for NIXSW measurements, as elaborated in **Section 3.3**.

Selection of photon energies from undulator spectra is done by a Si(111) double-crystal monochromator (DCM) for hard X-rays, followed by numerous beam optics to align and focus the beam, and improve resolution. Meanwhile, for soft X-rays, a plane grating monochromator (PGM) is utilised for energy selection, with optics acting to similar effect are utilised [3, 26].

Both the PGM and DCM are based upon the physics of diffraction, where light reflecting off of a grating forms a diffraction pattern with angular spacing defined by its wavelength. This system is described by the following condition for constructive interference from a diffraction grating:

$$m\lambda = d_G(\sin\alpha + \sin\beta), \quad (2.7)$$

where constructive interference occurs for integer, n , multiples of wavelength, λ , the term $d_G \sin\alpha$ defines the incoming path difference between waves incident on different grooves in the grating, and $d_G \sin\beta$ defines the outgoing path difference, where α and β are the incoming and reflected angles, respectively, with respect to the normal of the plane grating. When the

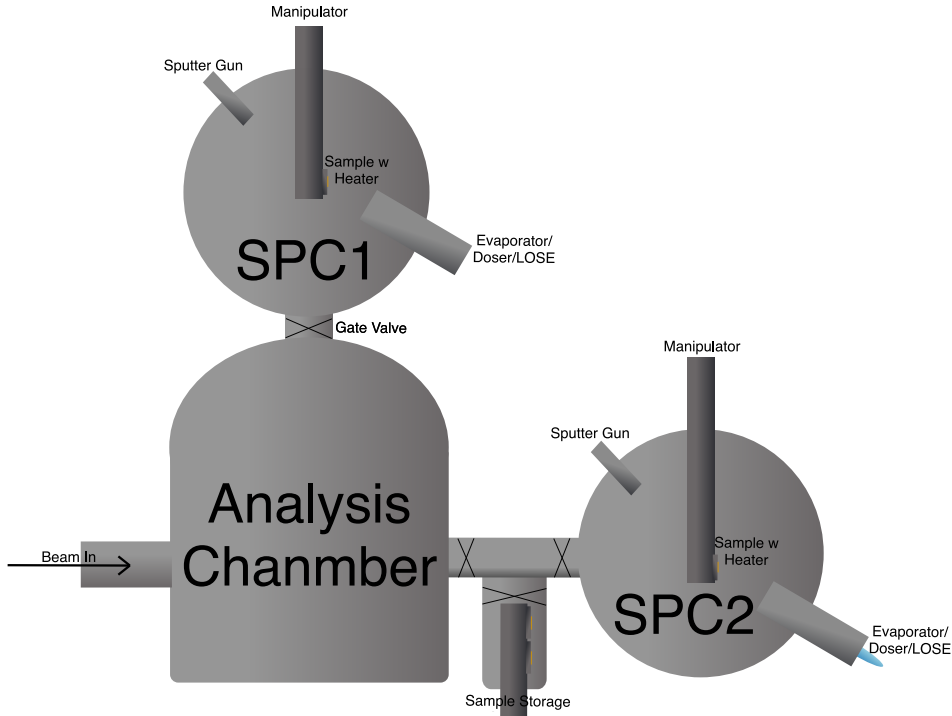


Figure 2.2: Partial schematic diagram depicting the fundamental components making up the I09 EH2 UHV chamber. Note that this only includes primary components of the system [3].

undulator X-rays are incident on the PGM, the spectrum of wavelengths contained within the beam are spread spatially, this spread is directed at an exit slit which selects for photon energy from the spatial spread. To adjust the photon energy, the plane mirror preceding the PGM and the PGM itself will be rotated to adjust the resulting diffraction pattern, and thus the photon energy passing through the exit slit. The basis of the DCM is very similar, however, due to the smaller wavelengths of the hard X-rays, the grating spacing for a PGM would be too large such that the spread of wavelengths would not be too narrow, and the resulting energy resolution would be too broad. Alternatively, the DCM utilises the atomic spacings of two Si(111) single crystal mirrors for diffraction, compared to the spacing of the gratings in the PGM; with the second crystal staggered, but still parallel. This second crystal redirects the beam back in the direction of the beamline; whilst also providing better energy resolution through undergoing diffraction again. These crystals are then rotated to adjust incidence angles to select for photon energies.

2.2.1 I09 End-station

EH2 is the main end-station of the I09 beamline, receiving the beam spot of both the soft and hard X-rays onto its main manipulator. A diagram of the I09 end-station can be seen in **Figure 2.2**. The end station consists of an analysis chamber with 1 preparation chamber atop the analysis chamber (SPC1), and another preparation chamber adjacent to the analysis chamber (SPC2). In the analysis chamber and SPC1, is an electronically controlled 5-axis

manipulator, with an in-built heating filament, that can move between the two stacked chambers; between which there is a gate valve to prevent exposure of the analysis chamber during preparations. Meanwhile, SPC2 has its own manual transfer arm (not shown), that can move samples between the analysis chamber, a sample storage chamber, and SPC2, and a manual manipulator with two sample holders, either with a pBN or an e-beam heater. In both preparation chambers, there are ports for dosers/evaporators to be mounted, in addition to ion guns paired with argon leak valves for sputtering clean the crystals. Not shown in the diagram are 2 load-lock chambers, attached to the analysis chamber and SPC2, for loading samples into the UHV chamber from atmospheric pressure; these are then pumped down sufficiently before they can transfer into their respective chambers with their own transfer arms. The analysis chamber contains a micro channel plate (MCP) LEED, the point at which the X-ray beams converge, with a hemispherical analyser (VG Scienta EW4000 HAXPES angular acceptance of $\pm 30^\circ$) mounted perpendicular to the manipulator and incident beam. This chamber is where XPS, NIXSW, PhD, and LEED are measured; for NIXSW, specifically, a fluorescent plate with a hole is fixed on the entrance through which the X-ray beam arrives. The fluorescent plate, along with a CCD camera to measure intensity, are used to measure the reflectivity of curve of the crystal during NIXSW.

Chapter 3

Experimental and Supporting techniques

3.0.1 Inelastic Mean Free Path and the Universal Curve

The Inelastic Mean Free Path (IMFP) of an electron is one of the key properties to understand in surface science as it directly influences the surface sensitivity of a technique through their penetration depth into the surface. The IMFP is defined as the mean path length of an incident electron through a material before undergoing an energy loss mechanism through interaction with the solid. These include: plasmon scattering, single-particle electron excitations with valence and core electrons; phonon scattering, however, can be ignored as it induces too small energy changes on involved electrons to be notably detectable by most techniques [27]. The fundamental relationship of IMFP describes the exponential decay in intensity of a beam of electrons incident on a solid surface:

$$I(d) = I_0 e^{\frac{-d}{\lambda(E)}} \quad (3.1)$$

where $I(d)$ is the intensity after the primary electron beam has travelled through the solid to a distance d ; I_0 is the initial intensity before attenuation. The parameter $\lambda(E)$, termed the inelastic mean free path (IMFP), is defined as the distance an electron beam can travel before its intensity decays to $\frac{1}{e}$ of its initial value. Whilst IMFP does vary between materials, the relationship between IMFP and electron energy typically follows the same Universal Curve shown in **Figure 3.1**. The shape of the Universal Curve is dominated by plasmon scattering; the cross section of which varies with energy. The energy at which this cross section is greatest is called the *plasmon energy*, and defines the minimum in the curve. At energies lower than this *plasmon energy*, electrons have insufficient energy to cause plasmon excitation thus energy losses are limited only to single-particle excitation; thus IMFP for these lower energy electrons is much longer. Above the *plasmon energy*, the plasmon scattering cross section is high, hence, scattering becomes the dominant energy-loss mechanism. This cross section decreases with greater kinetic energy, giving much longer IMFPs for high energy electrons. At $\sim 2 - 3 \times$ the *plasmon energy*, one finds the minimum

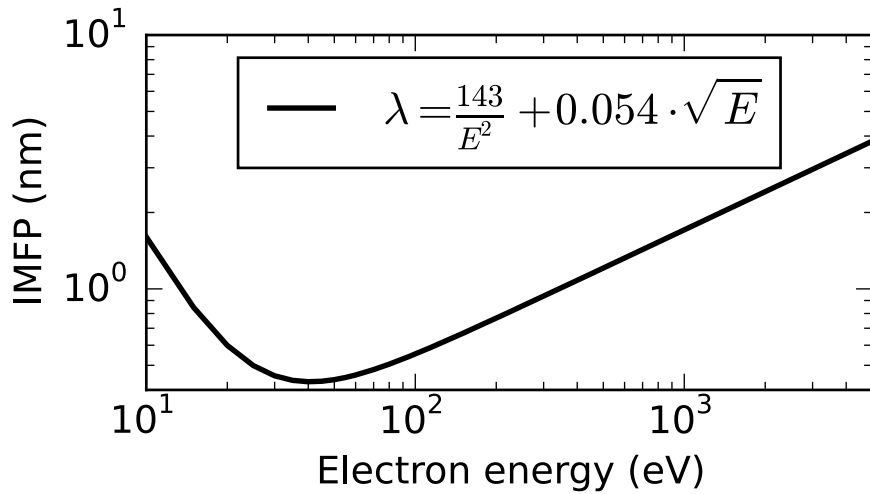


Figure 3.1: Universal curve depicting the IMFP for typical elements utilising equation 3.2, with $A = 143$, and $B = 0.054$ [4].

of the curve with kinetic energy around $50 - 100$ eV. The rapid increase in scattering length above this region of low IMFP can be interpreted through the velocity of the electron, where fast moving electrons have a short period of time to interact with a material before travelling further into the crystal. The effect on the lower end of this curve can be explained by electrons having insufficient energy to excite even valence electrons. These mechanisms are modelled by the following mathematical relationship:

$$\lambda(E) = \frac{A}{E^2} + B \cdot E^{\frac{1}{2}}, \quad (3.2)$$

where $\lambda(E)$ is the IMFP, A and B are parameters unique to a material that characterise the extent of inelastic energy loss of electrons within that material. The A parameter controls the lower energy interactions whilst the B parameter controls the higher energy interactions ($\gtrsim 150$ eV) [4].

This largely defines the surface sensitivity of techniques such as SXPS, PhD and AES, where electron energies are often about this energy range. For example, soft XPS which can utilise electrons in energy ranges of $100 - 1000$ eV where IMFP can range from 5.5 Å, to 17.1 Å. In reality, one must also consider elastic collisions which, though not energy-loss inducing, often extend path length, leading to attenuation from other inelastic effects. As such, the true mean path length of an electron, commonly referred to as electron *attenuation length*, is possibly up to 30% less than that predicted by the IMFP formula [28].

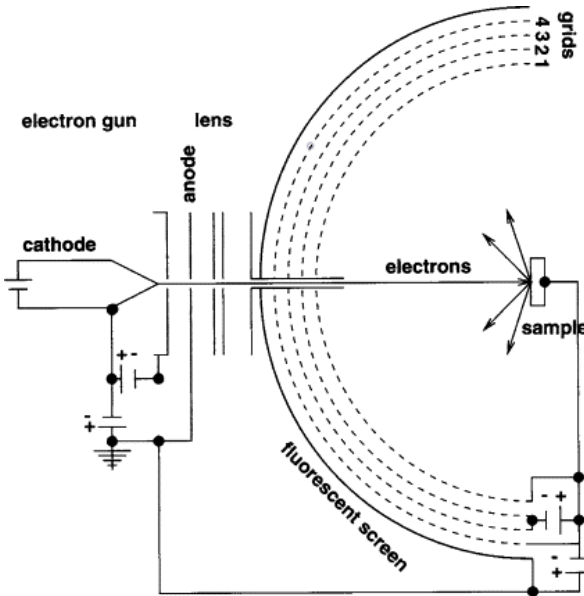


Figure 3.2: Setup of a LEED experiment depicting electron gun on (left) firing low energy electrons at a sample, off which the electrons diffract towards the hemispherical fluorescent screen which is shielded by EM grids, often used for retarding low energy electrons.

3.1 Low Energy Electron Diffraction

One of the oldest and most common surface sensitive techniques is that of Low Energy Electron Diffraction. Diffraction of electrons, and consequently the earliest evidence of wave-particle duality, was discovered by *Davidson and Germer* in 1927 [29]; as described in the previous section, at low kinetic energies of the electrons, the IMFP is short and the diffraction process becomes surface sensitive. At energies between 10 - 100 eV, layers deeper than 3 – 4 atoms are invisible to the technique. The schematic diagram for LEED can be seen in **Figure 3.2**, depicting an electron gun, emitting low energy electrons of precise kinetic energy at a crystal target from which the electrons will scatter and diffract. The resulting diffraction pattern is collected on a fluorescent screen. There are various electric grids used to create fields for adjustment of the resulting diffraction pattern, for example, an initial retarding grid is used to limit the random sources of electrons on the fluorescent screen.

The resulting diffraction pattern is representative of the long range ordered structures across the surface, with an information depth of roughly a few atoms deep. A consequence of the low IMFP in LEED, is an inherent complexity in the LEED pattern. This makes it difficult to model LEED patterns accurately, especially when the surface structure is not known, and is trying to be solved as is done in LEED-IV. To fully interpret a LEED pattern, one requires positions and intensities as a function of energy for which a dynamical diffraction theory that accounts for multiple scattering by each of the atoms in the involved layers is necessary. Instead, LEED is more often used as a qualitative technique, using a simple geometric theory.

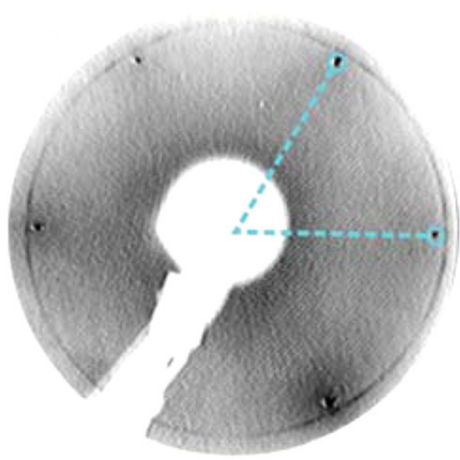


Figure 3.3: Image of LEED pattern of graphene on Cu(111), depicting copper lattice spots with characteristic graphene arc. Image was taken at 150 eV [5].

This geometric theory is based off of the simple fact that the diffraction spot position are determined by the size and shape of the unit cells on the surface, with intensities defined by the atomic co-ordinates in this unit cell. The LEED pattern and its spots comprise a reciprocal lattice, where a large separation between spots indicates a small real space separation on the surface, and *vice versa*. An example of a LEED pattern is shown in **Figure 3.3**. This is conveyed mathematically with real space basis vectors for the unit cell \mathbf{a}_1 and \mathbf{a}_2 , defining a parallelogram with angle between them, γ . Whereas the reciprocal space equivalents are \mathbf{a}_1^* and \mathbf{a}_2^* , with angle γ^* . The vectors relate by the following scalar product expression:

$$\mathbf{a}_i \cdot \mathbf{a}_j^* = \delta_{ij}, \quad (3.3)$$

where $i, j = 1$ or 2 , and δ_{ij} is the Kronecker δ function which is equal to 1 where $i = j$ and 0 elsewhere. This gives subsequent relationships:

$$\mathbf{a}_1^* = \frac{1}{\mathbf{a}_1 \sin \gamma}, \quad (3.4)$$

$$\mathbf{a}_2^* = \frac{1}{\mathbf{a}_2 \sin \gamma}, \quad (3.5)$$

$$\gamma = \gamma^*. \quad (3.6)$$

Whilst this approach can provide distances and bond lengths, with precision depending on that of the bulk crystal and LEED setup, it is often useful for verification of type of structure, order and relative coverage [24, 25].

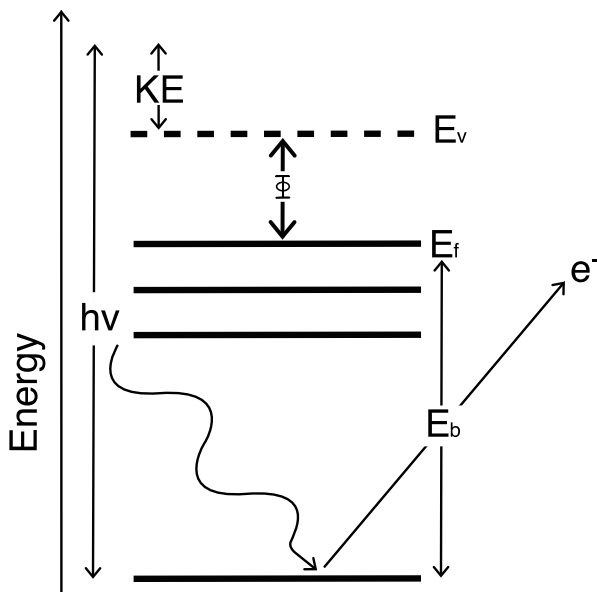


Figure 3.4: Diagram of the process of photoemission during XPS, depicting an incident photon of energy, $h\nu$, exciting a core level electron of binding energy, E_B , surpassing the work function, Ψ , between the vacuum level, E_v , and the fermi level, E_f , emitted with kinetic energy, KE.

3.2 X-ray Photoelectron Spectroscopy

X-ray photoelectron spectroscopy (XPS) is a spectroscopic, surface analysis technique often used for both qualitative and quantitative elemental analysis. XPS probes the binding energies of core level electrons in the X-ray region. It does so through measurement of the kinetic energies of electrons emitted as a result of absorption of an X-ray. The high energy of X-rays allows probing of an atom's core levels which are not involved in bonding, and thus their energies are primarily characteristic of the atom from which they originate, allowing distinguishing of different elemental species in a substance, with a slight energy shift due to the surrounding environment. As electrons are predominantly excited by photons of energy similar to their binding energy, the resulting kinetic energies are mostly insufficient for deep penetration of the surface due to their shorter IMFP, see **Section 3.1**, making the technique particularly surface sensitive. It is one of the primary techniques used for most adsorbate studies. The previously mentioned shifts in binding energy, referred to as chemical shifts, due to the surrounding chemical environment depend on the bonding environment around the atom; highlighting features that are indicative of this such as an atom's oxidation state. The result of an XPS measurement and analysis is a spectrum of photoelectron intensity with respect to binding energy of the electron, seen in **Figure 3.5**, depicting peaks with features unique to the electronic and chemical environments within a sample.

The process of XPS, depicted in **Figure 3.4**, involves the following steps: absorption of a photon with an energy greater than the binding energy of an electron; after which a photo-electron is emitted with kinetic energy from the surplus of energy remaining after excitation.

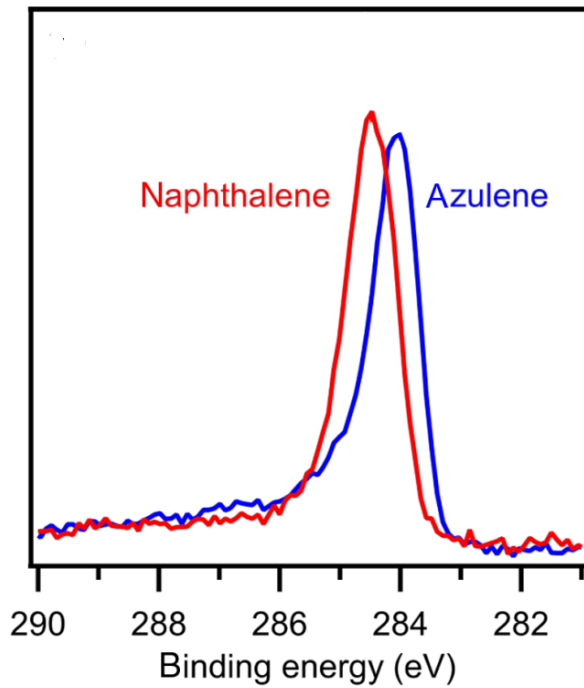


Figure 3.5: Example C 1s XPS spectrum of monolayer napthalene and azulene on copper(111)[6].

The minimum energy required for an electron to be emitted from a material is the work function, ϕ , the energy gap between the fermi and vacuum level, for a material. For metals, this is the minimum energy required to excite an electron to the vacuum level from the Fermi level (the highest occupied energy level). This process is defined by the principal equation of XPS; describing the binding energy (E_B) of the photoelectron in the absence of shifts:

$$E_B = h\nu - E_K - \phi, \quad (3.7)$$

where h is Planck's constant, ν is photon frequency, and E_K is the kinetic energy of the photoelectron. This interaction involves the excitement of an electron from core-level to the vacuum level, the energy at which the electron escapes the potential of the atom. Instead of defining E_B in reference to vacuum level, in a typical XPS experiment, binding energies are commonly referenced to the previously mentioned Fermi level. This energy can be determined quickly and accurately during the experiment through measuring the lowest binding energy emission in an XPS spectra. Whereas the vacuum level requires further information unique to an experimental system, for example, the variable work function of the analyser, making it less easy to use as a reference point [24, 25].

3.2.1 Quantum Mechanical Approach

To fully understand the contributions to an XPS peak, one can interpret the quantum mechanics of the photoemission interaction. The binding energy of an electron in an X-ray photoemission interaction can be taken to equal the energy difference between the initial state of the atom with n electrons and final state of the ion with $n - 1$ electrons:

$$E_B(k) = E_f(n-1) - E_i(n), \quad (3.8)$$

where $E_f(n-1)$ is the final state energy and $E_i(n)$ is that of the initial state. Koopmans' theorem is the one electron approximation case. This is where no spectator electrons rearrange, and the binding energy would be the negative of the orbital energy of the initial electron state:

$$E_B(k) = -\varepsilon_k, \quad (3.9)$$

where ε_k is the negative of the orbital energy of the initial state of the electron, and binding energy is referenced to vacuum level. This approximation can be defined using the single particle wavefunction of the unremoved electron, ϕ_j , the $n - 1$ wavefunction of the electrons in the resulting ion, $\Psi_j(n-1)$:

$$\psi_i(n) = \phi_j|\Psi_j(n-1), \quad (3.10)$$

where ψ_i is the wavefunction for the whole initial state. Whereas the final state wavefunction is:

$$\psi_f(n-1) = \Psi_j(n-1). \quad (3.11)$$

Applying the Hamiltonian operator, we can determine the energies of the initial state:

$$E_i(n) = \langle \psi_i(n) | H | \psi_i(n) \rangle, \quad (3.12)$$

and the final state:

$$E_f(n-1) = \langle \Psi_j(n-1) | H | \Psi_j(n-1) \rangle, \quad (3.13)$$

so long as $E_i(n)$ and $E_f(n-1)$ are single valued, only one peak is expected.

Next, one must consider the final ionic state of the system with an unstable core hole in place of the electron. Within the atom, the energies of the remaining electrons within the system relax to shield the newly created core hole, regardless of phase of the system. Extra-atomic relaxation can also occur involving the electrons of neighbouring atoms. To incorporate this, a more complex description of the final state wavefunction must be made. This can be written

in terms of the possible eigenstates of the ion:

$$\psi_f(n-1) = u_k \Psi_{jl}(n-1), \quad (3.14)$$

where u_k is the excited electron wavefunction with momentum k , Ψ_{jl} are l th ionic state wavefunctions with a hole in the j th orbital. Whereas before, in **Equation 3.11**, the ion hole state was described by $\Psi_j(n-1)$, this is no longer an eigenstate of the ion as relaxation and reconfiguration has occurred. The final state energy must therefore include all the possible final state wavefunctions such that the energy of the state is:

$$E_{fl}(n-1) = \langle \Psi_{jl}(n-1) | H | \Psi_{jl}(n-1) \rangle, \quad (3.15)$$

with up to l number of solutions, indicating the possibility of multiple peaks at different energies from the same transition when solving **Equation 3.8**. This model must also include relativistic and electron correlation effects in addition to the relaxation effects leaving a more comprehensive description of binding energy:

$$E_B(k) = -\epsilon_k - \delta\epsilon_{relax} + \delta\epsilon_{rel} + \delta\epsilon_{corr}. \quad (3.16)$$

It is useful to distinguish between initial and final state effects on binding energy and spectra. To a good approximation, one can take initial state effects to be dependent on the electron configuration in and around the atom as a result of chemical bonding; referred to as chemical shift (ΔE_B). This can also be approximated to shift all core levels to a similar extent. Additionally, the oxidation state of an atom directly impacts the binding energy, increasing it due to reduced shielding by other electrons within the shell, or vice versa.

Final state effects are those which stabilise or destabilise the final state after the photoemission process. Generally, atomic relaxation results from rearrangement of outer shell electrons due to their lower binding energy. As such, a materials conductivity plays a large role in this mechanism, in particular, through extra-atomic relaxation. For conductive metals, shared delocalised valence electrons are able to screen core holes in neighbouring atoms incurred during photoemission. On the other hand, in insulators, electrons are not free to move between atoms and thus neighbouring electrons are only polarised by the core hole; largely limiting the effects of extra-atomic relaxation. Satellite features are an umbrella term for a range of final state effects, including: shake-up events, multiplet splitting and vibrational fine structure. Shake-up events occur when the outgoing photoelectron transfers some energy to a valence electron, exciting it to a previously unoccupied state molecular orbital state, and, in most cases, an electron-hole pair forms. This reduces the kinetic energy of the outgoing

electron and so is seen as a tail, or a separate peak for semiconductors, on the high binding energy side of all XPS peaks, often referred to as peak asymmetry during peak fitting. Alternatively, shake-off events can occur, where sufficient energy is transferred such that the secondary electron is excited to vacuum level and so is also emitted in a double-ionisation event. Whilst shake-up events can produce distinct peaks, this is generally not the case for shake-off events.

Multiplet splittings arise from cases where atoms contain unpaired electrons that interact with the core hole after photoemission through spin orbit coupling. Where parallel and antiparallel spins have different stabilities and thus energies. The complexity of this multiplet is dependent on the number of unpaired electrons present and the possible unique combinations of spins. Vibrational fine structure refers to the possible variations in final vibrational state of the ion after photoemission. Vibrational energy levels are orders of magnitude lower in energy than electronic transitions, thus the variation in measured binding energy of the photoelectron as a result of vibrational transitions are often insignificant and require high resolution to detect.

An XP spectrum is measured by detecting kinetic energies of In XPS, there are a number of parameters of the resulting peak that give indications towards the system of the atomic species involved. For example, the line width of photoemission peaks is determined by the lifetime of the core hole, known as homogenous broadening, and instrument resolution, in addition to satellite features and sample in homogeneity. The instrument resolution is determined through both the resolution of the detector, and also by the energy resolution of the incident X-ray beam. The intrinsic peak width, Γ , is defined through the Heisenberg uncertainty relation, and inversely related to the core hole lifetime, τ , by:

$$\Gamma = \frac{h}{\tau}. \quad (3.17)$$

This lifetime, τ , is dependent on the depth of the core hole, becoming shorter for greater depth, which can broadly be explained as deeper core holes having more de-excitation channels to fill them. Similarly, the lifetime broadening is also dependent on atomic number through total number of electrons, thus number of de-excitation channels. Homogenous broadening is inherently Lorentzian, and thus when interpreting and fitting XPS peaks, a Lorentzian distribution is used.

XPS also has the ability for quantitative analysis, with peak areas nominally proportional to the quantity of an element present. This mainly due to the photoionisation cross sections

of core levels being mostly independent with respect to different surrounding chemical environment, though not entirely, as is exploited by EXAFS. Photoemission intensity attenuation must also be taken into account as the IMFP of photoelectrons are relatively low, in particular, for study of numerous layers of materials. This must be accounted for through models, hence many quantitative studies are done using sub monolayer surface coverages where relevant, whilst maintaining sufficient coverage for a substantial signal to be measurable. When carrying out XPS analysis, background intensity must also be measured on a standard then subtracted before meaningful areas can be extracted. Taking the total intensity of a photo-electron peak, I , to consist of the sum of constituents dI stemming from position r , then one can encompass the various factors affect peak intensity with the following description:

$$dI = \Phi(r) \times N(r) \times \sigma \times p(r) \times \theta_{acc} \times \eta_{det}, \quad (3.18)$$

where $\Phi(r)$ is the X-ray flux at position r , σ is the cross-section of the photoemitting species, $p(r)$ is the probability of no loss escape of electrons at position r , θ_{acc} is the acceptance angle of the electron analyser, and η_{det} is the detection efficiency of the instrument. Whilst it is possible to reduce the cumulative error to accuracies of 5 – 10%, less rigorous analysis can lead to substantial errors, and diffractive effects can lead to variation of up to 40%, making quantitative analysis unreliable.

Note that binding level is reference to vacuum level so as to avoid any shifts relating to possible changes in instrumentation such as the additional work function of the analyser. Despite this, the majority of experimentally acquired binding energies are referenced to the Fermi level of the solid because of the difficulty in determining vacuum level; requiring information regarding the work functions, and potentials in the experimental system. [24].

3.2.2 Data Acquisition and Reduction

XPS requires an X-ray source, commonly a metal anode sources, though laser and synchrotron sources are also growingly common [30], an electron energy analyser, and a UHV chamber of course, though ambient pressure XPS is possible in certain specialised systems. Data is acquired by scanning through kinetic energy on the electron analyser with X-rays incident on the sample. Whilst broad overview scans can be useful to compare intensities of different core levels, for accurate study of a specific XP peak, smaller range scans including only the peak of interest, its satellite features, and some background to help in peak fitting. XP spectra are plotted as photoelectron intensity versus binding energy. In addition to measurement of the XP spectra at a specific photon energy, Fermi edge is also measured to correct for any binding energy variation. This accounts for differences in experimental

conditions and system that produce changes in measured binding energies of the peaks. The peaks in the spectra are then fit.

Peak Fitting

The fitting of an XP spectra is a vital part of analysis which can convey various structural and electronic information about the species of interest whilst removing broadening and shifts resulting from instrumental and experimental factors. Each of these effects are superimposed upon each other, and must be fit with a peak model. Whilst there may exist a best mathematical solution to fitting a peak, this must be tied to physical and chemical properties and their effects to obtain a realistic model from which this information can be extracted. There are checks that can ensure that a peak model is realistic. A good peak model will utilise various lineshapes, to model different final and initial state effects, a sensible number of component peaks, and varying restrictions, which can be tied to the variables of other components, all of this is done from a chemically realistic basis.

The overall peak shape of a photoemission peak is made Lorentzian by the uncertainty principle acting on the electron energy levels:

$$L(E, E_c, \gamma) = \frac{\gamma/\pi}{(E - E_c)^2 + \gamma^2}, \quad (3.19)$$

where γ is the half-width half-maximum (HWHM) of the lineshape, and E is energy, and E_c is the centre of the peak distribution.

Meanwhile other factors including instrumental and phonon broadening contribute a *Gaussian* line shape [31, 32]:

$$G(E, E_c, \sigma) = \frac{1}{\sigma\sqrt{2\pi}} \exp\left(-\frac{(E - E_c)^2}{2\sigma^2}\right), \quad (3.20)$$

with a HWHM of α , and a standard deviation σ , related to each other by $\alpha = \sigma\sqrt{2\ln 2}$. To combine the two effects, a convolution of the two is created, known as a *Voigt* function [33]. The lineshapes of the respective peaks are displayed in **Figure 3.6**. The prominence of either of the peaks can be defined using a *Gauss-Lorentz* ratio $g = \frac{lhm}{lhm+ghm}$, where lhm is HWHM of the *Lorentzian* component and ghm is that of the *Gaussian* component. This parameter takes a value in a continuous range between 0 to 1, where 0 is totally *Gaussian* and 1 is totally *Lorentzian*. Generally, compounds will tend to be more *Gaussian*, whilst metals and isolated elements tend to be more *Lorentzian*, however, as there are many factors that increase the different characters of this peak and its *Gauss-Lorentz* ratio is far from definitive. The shapes of these functions and the combined Voigt function can be seen in **Figure 3.6**. As described in the previous section, the FWHM or width of an XPS peak, depends on various instrumental

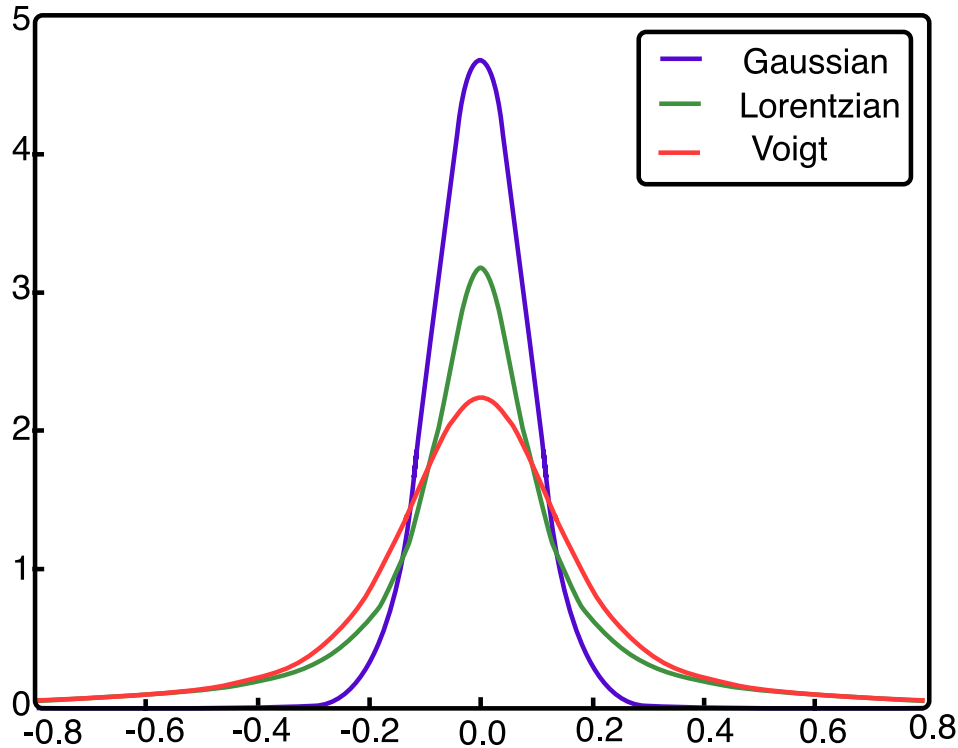


Figure 3.6: Diagram of Gaussian (blue), Lorentzian (green), and Voigt (red) lineshapes [7].

influences (e.g. linewidth of X-ray source), and physical factors (e.g. chemical environment). Asymmetry of a photoemission peak is another important and complex parameter, sometimes contributed to by instrumentation and measurement artifacts, though primarily due to band structure and other physical mechanisms. Asymmetry is typically modelled by an exponential tail guided by characteristics of the *Lorentzian* and *Gaussian* peak parameters. It is also common to model asymmetric peaks in the case of metallic materials through application of a Doniach-Sunjic function [34]:

$$f(E, \alpha, F, E_c) = \frac{\cos \left[\frac{\pi\alpha}{2} + (1-\alpha)\tan^{-1} \left(\frac{E-E_c}{F} \right) \right]}{(F^2 + (E-E_c)^2)^{\frac{(1-\alpha)}{2}}} \quad (3.21)$$

where F is the FWHM, E_c is binding energy centre position (not position of maximum intensity), α is an asymmetry parameter, and E the binding energy position of the peak.

newline

Another important step in peak fitting is determining and subtracting the background. In any peak, the base has the greatest contribution to the area, thus if fitted incorrectly, the measured area of the peak can vary substantially from its true value. A simple fixed linear background is discouraged as the shape of a background can be complex, with non-linear components such as Shirley step functions, Tougaard functions, and parabolas[32]. This is in addition to the other intrinsic and extrinsic effects, described previously that distort peak

shape, introduce splitting, and satellite features and tails. These must be identified visually and accounted for.

Auger decay electrons

Auger decay electrons are a result of secondary relaxation processes that can occur to fill core holes (e.g. those created through photoemission), and are seen in XPS with constant kinetic energy with respect to photon energy spectra. When a core hole is created, it is eventually filled by another electron from a lower binding energy level in conjunction with the emission of energy associated with this transition. This can occur through emission of a photon as is utilised in X-ray anode sources; or it may be donated to another electron as kinetic energy. The Auger decay effect describes when electrons are given sufficient energy as a result of a core hole being filled, such that they reach vacuum level, and are emitted. The difference between this two is highlighted in **Figure 3.7**, where the left diagram shows photon emission as a result of core hole filling, and the right diagram shows emission of electron as a result of core hole filling. The basis for Auger emission can be described using solely binding energies of the levels involved in the mechanism like so:

$$KE = E_h - E_i - E_e, \quad (3.22)$$

where KE is the kinetic energy of the Auger electron, E_h is the binding energy of the initial hole, E_i is the binding energy of the initial filling electron, and E_e is the binding energy of the electron before Auger emission. The key feature of this process is that the kinetic energy of the Auger electron is not dependent on the process that produced the core-hole, and is characteristic of the energy levels involved in the interaction. This has the consequence that the Auger peaks are of constant kinetic energy, however, as XP spectra are plotted against binding energy, the Auger peak will exist at a binding energy of $KE - h\nu$. For tunable X-ray sources, the position of the Auger peak will vary depending on the photon energy utilised and can sometimes obscure or be mistaken for photoelectron peaks which must be accounted for. These values are calculated for a single electron system and, as with XPS, a range of factors have an effect on each of the states of the system. Factors which lead to complex peaks that are analysed in Auger electron spectroscopy (AES), that will not be covered here [24].

3.2.3 Photon source for XPS

Traditional X-ray sources, also known as anode sources, impinge high energy electrons on generally solid metal targets, typically made of silver, copper, aluminium, or magnesium; these electrons collide with those in the metal causing them to be emitted forming core holes within the electronic structure of the atoms. The process of de-excitation of electrons in outer shells to fill these holes leads to photon emission, with photon energy corresponding

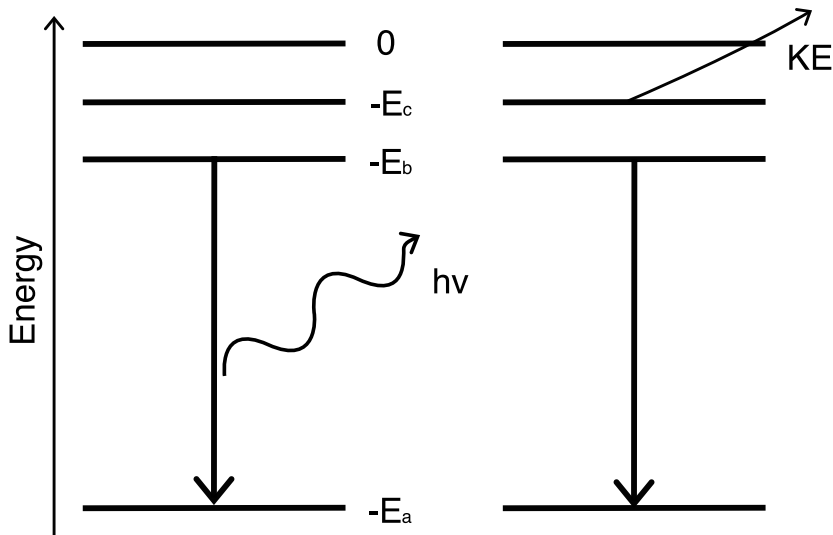


Figure 3.7: Energy level diagram depicting two types of transitions involved in core hole filling. The left diagram depicts emission of a photon as a result of core hole filling, and the right diagram shows Auger emission.

to the difference in energy between these states. As there are a limited number of pathways of de-excitation, this leaves a limited number of energies of transition, thus photon energies. As a result, an anode source produces an X-ray spectrum consisting of intense characteristic emission lines, and lower intensity, continuum background intensity due to bremsstrahlung radiation produced by deflections of the electrons with the fields within the material.

An ideal X-ray source will be as monochromatic as possible, thus a metal that has a low bremsstrahlung intensity and intense line emissions is chosen. Some metal anode sources utilise monochromators to further narrow the photon energies produced whilst also allowing choice of emission line, however, the majority of sources are unmonochromatised. These unmonochromatised sources produce multiple emission lines, which produce multiples of each peak for each emission line of the source. This convolutes the XPS spectra, making the identities of peaks harder to interpret, often covering up vital binding energy regions, overlaying different peaks over one another. The resolution of these sources is often particularly low, with a broadening of several tenths of an eV, far larger than many chemical shifts. Whilst improvements can and have been made on producing better X-ray sources, for example, use of target materials with higher energy characteristic line emissions, which opens the door for higher binding energy levels, this also reduces the technique's vital surface sensitivity[24, 25, 30]. For the most part, these have insufficient intensity in comparison to the main alternative approach is the use of synchrotron radiation. . This produces polarised light with intensity orders of magnitude more intense than the best anode and laser sources, continuously, over a broad spectrum of energies[30]. It effectively utilises the bremsstrahlung

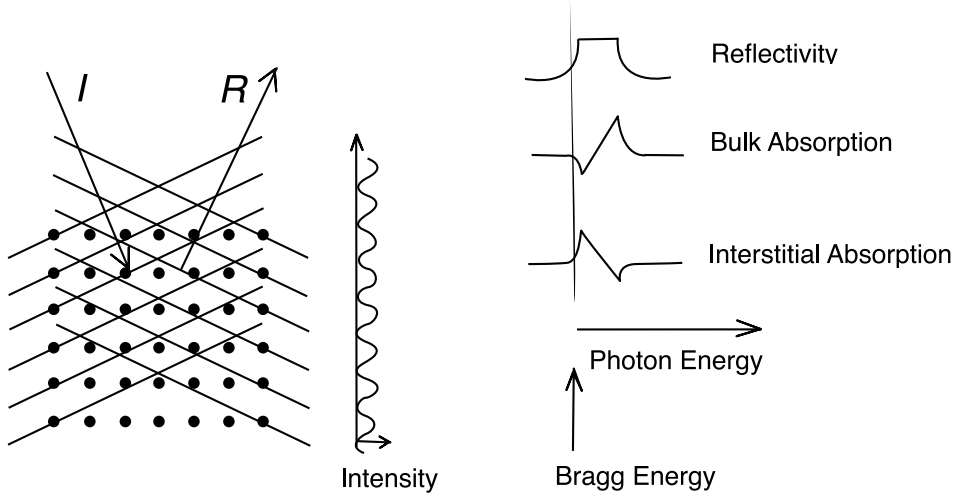


Figure 3.8: Left diagram of X-ray standing wave pattern, showing nodal planes of plane waves for incoming and reflected X-ray waves with respect to the positions of the atoms in the bulk, along with the intensity of the resulting XSW wave pattern formed from the incident and reflected waves. The right hand diagram depicts the reflectivity curve of a bulk crystal, also known as a Darwin curve, and the absorption profiles one would measure for species sitting at bulk and interstitial sites within the lattice as one scans through Bragg condition [8].

mechanism involved in the broader continuum of anode sources, but on a much larger, higher energy scale, producing a lightsource that is far better. Equally, measurements that would take hours on an anode source, may only take minutes at a synchrotron beamline. One drawback of using synchrotron sources is that the photon flux is often so great that it can cause damage to the sample being analysed, referred to as beam damage. X-rays are already highly ionising such that they can induce chemical reactions and rearrangements to structures on a surface, sometimes causing desorption altogether. This can lead to additional XPS peaks and invalidate results thus photon intensities must be tuned to ensure this does not happen.

3.3 Normal Incidence X-ray Standing Waves

X-ray standing waves (XSW) is a surface structure determination method that utilises the standing wavepattern set up between the incident and reflected X-ray wavefield scattered from the various atomic planes within a bulk crystal. The resulting standing wavefield takes up a period that is equal to or a submultiple of the scattering plane spacing, seen in **Figure 3.8**, and spans the surface (roughly $\sim \mu\text{m}$ penetration depth), as a result of attenuation due to backscattering by the atomic layers, and a region extending out of the surface. The X-ray absorption by atoms within the substrate and adsorbate is proportional to the intensity of the wavefield at that point, whilst the intensity of the wavefield at a point is controlled by the position relative to the nodal planes in the standing wavefield pattern. The wavelength of

the standing wavefield, corresponds to the periodicity of the crystal scattering planes with a phase relationship with positions of the atoms in the crystal. The characteristic reflectivity of the crystal is defined by the Bragg condition and occurs over a finite range in the Bragg conditions, over which the reflectivity for a non-absorbing crystal remains constant but the relative phase changes by π , as depicted in **Figure 3.8**. This phase difference physically shifts the position of the nodal planes within the standing wave. By varying the parameters in the Bragg condition through this range through Bragg angle, or incident photon energy when at 90° Bragg angle (NIXSW), then one shifts the relative location of the atoms in the lattice, with respect to the nodal planes. Thus, taking an atomic species that is located at a consistent position within the structure; its position relative to the scattering planes in this structure can be determined by measuring the X-ray absorption across the Bragg condition [35, 36].

Bragg Condition

The diffraction undergone during XSW can be described using the Bragg condition; which describes the required conditions for diffraction to occur as a result of an incident plane wave on the atoms within a crystal lattice:

$$n\lambda = 2dsin(\theta_B), \quad (3.23)$$

where $n\lambda$ equals an integer multiple of the wavelength of the planewave, with integer, n , and wavelength, λ , on a scattering plane with separation, d , at a specific angle from the scattering plane, θ_B . This is the idealised case with a monochromatic light source but is sufficient to understand XSW. In reality, there are various parameters of the crystal and light source with an energy and angular distribution, and so diffraction will broadly occur over a range of Bragg energies/angles as discussed further in this section. The Bragg equation also assumes infinite photon flux and an infinite crystal, which is not realistic and must be accounted for [8, 24].

Whilst, in initial applications of XSW, the scattering angle was utilised as the independent variable, this relies on accuracy of translation and rotation of the crystal to scan precisely through the angular Bragg condition to measure the absorption profile accurately. With the introduction of synchrotron radiation as a highly tunable light source, the use of photon energy as a scattering parameter at normal incidence became feasible. This method, known as normal incidence x-ray standing waves (NIXSW) only relies on control of photon energy which, using synchrotron radiation, can be done more accurately than the angular scanning, producing a much broader theoretical reflection. This technique is utilised on I09 at Diamond Light Source [3, 36].

3.3.1 Mechanism of XSW

Dynamical Scattering in XSW

To understand the function of multiple scattering in XSW, one must first begin with single scattering theory for the mechanism. The X-rays can be interpreted as incoming, and outgoing plane waves produced by the sum of the scattering by equivalent atoms across the pseudo-infinite single crystal lattice. If the Bragg condition is met, according to single scattering theory, the scattering events across the crystal are in phase, producing an “infinite” scattered intensity due to contributions from an “infinite” number of atoms. To solve this lack of flux conservation, one must take into account the attenuation in incident X-ray flux as the wave moves deeper into the crystal, not including the absorption of X-rays by the atoms, referred to as the non-absorbing crystal assumption. With each backscattering event, the transmitted flux decreases; eventually reaching a limit in penetration depth of the crystal. This model has several consequences: that the total reflectivity is finite, and occurs over a finite continuous range as opposed to a single discrete location. The resulting reflectivity curve plotting reflectivity versus Bragg condition, either scattering angle or photon energy, has a characteristic flat top referred to as a Darwin curve, seen in **Figure 3.8**. Moving across the Darwin curve, there is simultaneously relative phase shift in the full standing wave by π . This has the effect that the nodal planes shift by half a wavelength or d spacing across the Darwin curve. At the antinodal planes, the intensity of the wavefield thus X-ray absorption is much greater than that of the raw incident wave intensity. This relationship is conveyed in the absorption profiles in **Figure 3.9 & 3.8**, where the absorption profile is taken to be unity outside of the Darwin curve, then depending on the location, the absorption profile will take up a different shape, with maxima at 4 times unity. Next considering the case of an absorbing crystal, a decrease in reflectivity occurs across the Bragg condition; visible on the trailing edge of the measured reflectivity curve as this is where the bulk crystal lies along the antinodal plane, for most simple single element crystals, thus some proportion of the incident waves are absorbed by the bulk. By measuring the X-ray absorption with respect to the scattering condition, across the Bragg reflection, a characteristic absorption profile is produced, unique to the position of the atom relative to the scattering planes. This is depicted in **Figure 3.9**. However, this only conveys the position relative to one scattering plane within the structure. To determine the exact position of an atom in 3-dimensional space, absorption profile from up to 3, non-parallel scattering planes may be required. This is true for both within and atop the surface of a crystal, thus it can be used to study surface structures.

The intensity of the X-ray standing wave at position r can be determined from the sum

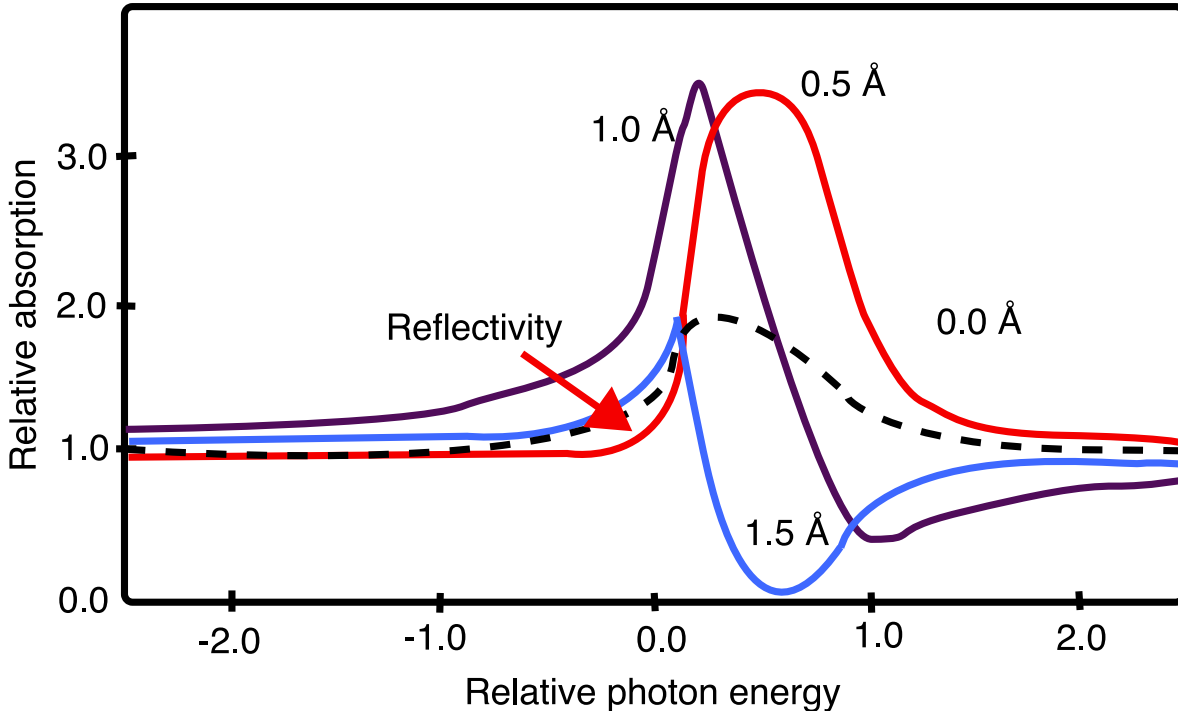


Figure 3.9: Diagram depicting the reflectivity profile for bulk absorption (red) and absorption profiles for atoms located at various points relative to scattering planes of a Cu(111) crystal. Instrumental broadening effects are not included in calculations [8]

of the incident and reflected wave:

$$I = \left| 1 + \left(\frac{A_H}{A_0} \right) \exp(-2\pi i \mathbf{H} \cdot \mathbf{r}) \right|^2, \quad (3.24)$$

where A_H and A_0 are the incident and reflected X-ray amplitude, and \mathbf{H} is the reciprocal lattice vector. This scalar product, $H \cdot r$, is simply the ratio of z , the perpendicular distance from the scattering planes, with d_H , the separation of these planes: $\frac{z}{d_H}$. X-ray reflectivity is defined as the ratio of the reflected and incident amplitudes, and is what is exploited in this technique. It can be determined from the geometrical structure factors like so:

$$\frac{A_H}{A_0} = - \left(\frac{F_H}{F_{\bar{H}}} \right)^{\frac{1}{2}} [\eta \pm (\eta^2 - 1)^{\frac{1}{2}}], \quad (3.25)$$

where F_H and $F_{\bar{H}}$ are the structure factors for the reflections H and $-H$, and η defines the position relative to the midpoint of the Darwin reflectivity curve. Experimentally, η can be determined from measuring a reflectivity curve with respect to one of the scattering conditions, sometimes referred to as a rocking curve referring to the rocking of the sample required when modulating the Bragg angle as the scattering condition. The angular width of this curve, $\Delta\theta$, defined as follows:

$$\Delta\theta = \frac{2(|P|\Gamma(F_H F_{\bar{H}}))^{\frac{1}{2}}}{\sin(2\theta_B)}, \quad (3.26)$$

where Γ is a fundamental constant parameter, P is a polarisation factor, and θ_B is Bragg angle. Considering the common (111) reflection at 45° on a Cu(100) crystal, the angular width is 3×10^{-4} radians. When considering this case it is clear to understand the limitations of using the angular scattering condition in XSW, as slight errors in collimation of the incident X-ray beam or control in rotation of the crystal could introduce significant uncertainty. The I09 beamline at Diamond Light Source exploit this, switching to modulating photon energy as the scattering condition. Whilst all XSW relies on highly collimated X-ray sources, that are easily provided by synchrotron light sources, energy varied XSW also requires synchrotron light sources for their finely tunable photon energies. The next problem is that bulk single crystal being studied must have a near-perfect mosaicity, so as not to broaden the measured rocking curve. Whilst this initially limited XSW studies to highly order covalent semiconductor crystals, a solution was found by taking measurements at normal incidence (NIXSW). It is clear from **Equation 3.26** that a $\theta_B \rightarrow 90$ leads to $\sin(2\theta_B) \rightarrow 0$, which leads to an infinitely increasing angular width, $\Delta\theta$. The value in normal incidence is that the gradient of the Bragg condition with respect to θ_B becomes 0 in these ranges, having the effect that slight inaccuracies in angle as a result of lacking crystal mosaicity have negligible effect on the rocking curve. **Equation 3.26** must be redefined in terms of energy for NIXSW:

$$\Delta E = \frac{E|P|\Gamma(F_H F_{\bar{H}})^{\frac{1}{2}}}{\sin^2 \theta_B}. \quad (3.27)$$

For example, taking the same (111) reflection of Cu(100) using photon energy as Bragg condition, the energy width becomes 0.87 eV, which, compared to the small angular width described before, is much more easily tuned for by the high quality monochromators found at synchrotron light sources [3]. To extract exact quantitative information from the XSW absorption spectra, the wave must be modelled and fit. Using the reflectivity, R , in terms of scattering condition, which is simply $\left| \frac{A_H}{A_0} \right|^2$, written in other terms as:

$$\frac{A_H}{A_0} = \sqrt{R} \exp(i\Phi), \quad (3.28)$$

where $\exp(i\Phi)$ accounts for a possible angular term. When factored into the principal **equation 3.24**, one gets:

$$I = \left| 1 + \sqrt{R} \exp \left(i\Phi - \frac{2\pi iz}{d_H} \right) \right|^2, \quad (3.29)$$

or equivalently:

$$I = 1 + R + 2\sqrt{R} \cos \left(\Phi - \frac{2\pi z}{d_H} \right). \quad (3.30)$$

Whilst this can be solved for z after calculation of the phase angle, Φ , from the Bragg condition in **equation 3.23**. In a real case, d_H is discrete due to thermal vibrations. Furthermore,

there is disorder on the surface and variation in height adsorption sites. Consequently, the values of height, z , will take up a distribution, $f(z)$, surrounding each of the common sites of the species. The sum of these fractional distributions is 1, or in other terms:

$$\int_0^{d_H} f(z) dz = 1. \quad (3.31)$$

This can be incorporated into **Equation 3.30**:

$$I = 1 + R + 2\sqrt{R} \int_0^{d_h} f(z) \cos \left(\Phi - \frac{2\pi z}{d_H} \right) dz, \quad (3.32)$$

Generally, this can be absorbed into a structural fitting parameter, coherent fraction, F_H .

Similarly, the z can be replaced by a coherent position, P_H :

$$I = 1 + R + 2F_H \sqrt{R} \cos \left(\Phi - \frac{2\pi P_H}{d_H} \right). \quad (3.33)$$

The coherent fraction acts to describe the extent of the spread of the distribution of z values about the coherent position. These parameters become misconstrued in the case of multiple species at different adsorption heights. For example, in a case where there is a 50:50 mixture of $P_H = 0.25$ and 0.50 , a simple NIXSW analysis will state a combined P_H of 0.375 , where no atoms sit, with a F_H of 0.50 . To interpret this type of data with multiple species, it can be helpful to convert this equation into Fourier form:

$$F_H \exp \left(\frac{2\pi i P_H}{d_H} \right) = \int_0^{d_H} f(z) \exp \left(\frac{2\pi i z}{d_H} \right) dz, \quad (3.34)$$

Where F_H is the conventional amplitude, and P_H is the phase of the Fourier component. It can be useful to interpret this in an Argand diagram to visualise the different species distinctly. Here, the left side of the relationship forms the component vectors for each species, i , with individual phases $\frac{2\pi z_i}{d_H}$ and length f_i ; whilst the right side represents the sum of component vectors with combined length F_H and phase $\frac{2\pi P_H}{d_H}$. Considering a case of two distinct sites of equal proportion, the Fourier series becomes:

$$F_H \exp \left(\frac{2\pi i P_H}{d_H} \right) = f_a \exp \left(\frac{2\pi i z_a}{d_H} \right) + f_b \exp \left(\frac{2\pi i z_b}{d_H} \right), \quad (3.35)$$

which neatly solves for $f_a = f_b = 0.5$ and $P_H = \frac{(z_a+z_b)}{2}$, implying that:

$$F_H = \left| \cos \left(\pi \left(\frac{z_a - z_b}{d_H} \right) \right) \right|. \quad (3.36)$$

It is clear in these situations, that the coherent position of the species must be predicted, often through supporting techniques such as DFT modelling.

3.3.2 Data Acquisition and Reduction of NIXSW

Detection of absorption of X-rays by adsorbed species on a surface, even of multilayer samples, on top of a bulk crystal of semi-infinite atomic planes is not possible through measuring attenuation of transmitted X-rays. Thus, to measure the absorption profile in XSW, secondary probes must be used. These can include photoelectrons from X-ray absorption, Auger electrons, or fluoresced photons resulting from the core-hole filling process.

In UHV, photoelectrons and Auger electrons are primarily utilised as probes, particularly for emitted energies of below 5 keV and especially 3 keV, where they are compatible with most typical electron analysers. Deciding between the two can be influenced by numerous factors. For example, a primary difference between the two when comparing for a specific core level is the resulting kinetic energy of the photoelectron or Auger electron, with lower kinetic energy electrons being easier to detect due to their higher cross section. Subsequently, choice of probe may be decided by the resulting kinetic energy of the probe electron. One benefit of Auger electrons as probes is that one does not have to consider non-dipolar effects. A substantial drawback for using Auger emission for XSW, is that this process can be induced by numerous processes that create a specific core hole; many of which result from X-ray absorption from substrate atoms, so the XSW profile for these components will be a result of the substrate atoms, not the adsorbate. This is an issue for surface samples where the proportion of surface to bulk is minute. However for bulk samples, it is more beneficial to use Auger emission. A further benefit of using photoemission, is the chemical specificity of the process, described in **Section 3.2** as this technique exploits XP spectra for photoemission detection. This gives rise to the possibility of differentiating coherent position between different chemical species of the same element, so long as the species are sufficiently chemically distinct [8, 24, 36, 37].

One would expect that the likelihood of multiple site adsorption is unlikely as this should lead to a different binding energy due to different stronger/weaker interaction with the surface, as described in **Section 3.2**. However, it is not uncommon for species to take up multiple different sites on the surface, whilst having similar energies such that their binding energy peaks cannot be distinguished. Other issues can arise from situations where there is sufficient coverage and adsorbate-adsorbate interaction that species are forced into specific unfavourable sites. This lattice mismatch is inevitable when adsorbates have different bond

lengths to that of the substrate, and is particularly exaggerated at higher coverages, manifesting as buckling in networks grown on a surface [8].

3.4 Energy-scanned Photoelectron Diffraction (PhD)

Photoelectron diffraction (PhD) is a spectroscopic technique used to determine structural information in the local environment surrounding specific atomic species, commonly used for adsorbates on metal crystals. Energy-scanned photoelectron diffraction does not provide direct structural information but produces a spectrum that can be modelled and optimised through a trial-and-error style approach similar to LEED-IV [9].

3.4.1 Principles of PhD

Photoelectron diffraction originates from coherent interference between the directly-emitted photoelectron wavefield from a core level of an atomic species of interest (the emitter atoms) with those scattered off nearby atoms (scatterers); depicted in **Figure 3.10**. As a result of varied scattering pathways, and phase shifts induced during scattering, the photoemitted electrons have an introduced phase shift relative to the directly-emitted component of the wavefield. Through variation in energy and/or emission angle, the different wavefield components will go into and out of phase with each other. This relationship can be used to probe structural information surrounding the species of interest, more specifically, the angle and path lengths undertaken by the photoelectrons and scatterer atoms. This information can be collected through measuring the photoelectron intensity whilst varying emission angle or photon energy. These two dependent variables give rise to two variations in this technique: energy-scanned (PhD) or angle-scanned (XPD) photoelectron diffraction which are each useful for probing different aspects of the structure. XPD at grazing emission angles can also be used to give information on the adsorbate-substrate registry. On the other hand, PhD uses low electron kinetic energy ranges ($\sim 50 - 400$ eV), though the photon energy used depends on the energy of the core level from which the photoelectrons are excited, this variable photon energy source can only be supplied through synchrotron radiation; PhD also probes from higher angles to utilise the dominant backscattering component. PhD as a technique has been compared to the popular technique: extended X-ray absorption fine structure (EXAFS) in particular surface-EXAFS. In SEXAFS, the interatomic distances between the emitter atom can be extrapolated from modulation of the photoabsorption cross section instead of the photoemission intensity. The photoabsorption cross section is a result of a matrix element composed of the initial core state of the electron, and the final photoelectron wavefield amplitude at the atom. Thus the emitter can be thought of as the detector, at which the wavefields of the photoemitted electron and the backscattered electrons interfere, with phase shift dependent on the photoelectron wavelength/energy. It may be clear to see that this is simply a spherically

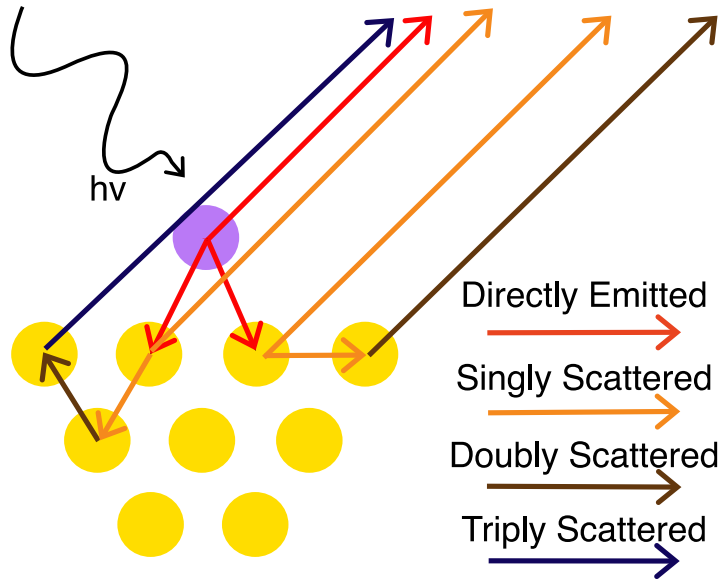


Figure 3.10: Diagram of various scattering pathways involved in PhD scattering calculations, depicting an incident photon the emitter atom (purple), and the various scattering pathways of the photoemitted electron by neighbouring atoms(yellow) [9].

averaged version of PhD; losing real-space angular information between scatterers and between the emitter(s). In contrast to techniques such as LEED, both SEXAFS and PhD do not require long range order on their surface making them valuable for studying adsorbate sites. This is because of the source of the incident probe (e.g. photon, or electron) which is found close to the site of interaction, meanwhile in XSW and LEED, the source of the probe is the incident photons/electrons effectively arriving from infinity as plane waves.

Whilst it is unfeasible to attempt to solve PhD directly, it can be helpful for understanding to attempt to do so, particularly with comparison to EXAFS. To describe the PhD and EXAFS mathematically, the problem can be simplified through considering the case of single scattering only, emission from an initial s-state, and to treat photoelectron wavefields as plane waves. The intensity of the field $I(\mathbf{k})$ in a given direction and energy specified by the electron wavevector \mathbf{k} is [9, 38]:

$$I(\mathbf{k}) \propto \left| \cos\theta_k + \sum_j \frac{\cos\theta_r}{r_j} f(\theta_j, k) W(\theta_j, k) \exp\left[\frac{-L_j}{\lambda(k)}\right] \exp[i(kr_j(1 - \cos\theta_j) + \delta_j(\theta_j, k))] \right|^2 \quad (3.37)$$

where the $\cos\theta_k$ represents the directly emitted component varying with θ_k , the angle between the polarisation vector of the light and the outgoing wavevector. The second term involves a summation over all individual scattering atoms denoted by j , each with a prefactor of $\cos\theta_r$, where θ_r relates the scattering angle with the emitter. Similarly, $\cos\theta_j$ accounts for the amplitude of the emitted wave at position \mathbf{r}_j relative to the emitter, with scattering factor $f(\theta_j, k)$

where θ_j is the scattering angle and \mathbf{k} is the wavevector. $W(\theta_j, k)$ is a Debye-Waller factor which accommodates for the reduced scattered coherent wavefield amplitude as a result of atomic vibrations. The term $\exp\left(-\frac{L_j}{\lambda(k)}\right)$ accounts for the attenuation of the scattered wavefield due to inelastic scattering, with pathlength L_j through the crystal relative to the directly emitter component. The phase of the scattered wavefield is controlled by the final exponential term with contribution from the scattering phase shift $\delta_j(\theta_j, k)$ and the phase difference induced by difference in pathlength $kr_j(1 - \cos\theta_j)$. A simplified expansion of this equation gives a function of the wavevector modulus:

$$\chi(\mathbf{k}) \propto \sum_j \frac{\cos\theta_r}{r_j} f(\theta_j, k) W(\theta_j, k) \times \exp\left[\frac{-L_j}{\lambda(k)}\right] \cos[kr_j(1 - \cos\theta_j) + \delta_j(\theta_j, k)] \quad (3.38)$$

The SEXAFS analog of this equation provides a good comparison that highlights the features and challenges in PhD analysis:

$$\chi(\mathbf{k}) = - \sum_j \frac{3\cos^2\theta_r}{kr_j^2} f(\pi, k) W(\pi, k) \times \exp\left(\frac{-2r_j}{\lambda(k)}\right) \sin(2kr_j + 2\phi_e(k) + \delta_j(\pi, k)) \quad (3.39)$$

The key expression to compare between **equation 3.38 & 3.39** is the final phase term contained within the cosine and sine terms. A Fourier transform can roughly be used to solve for this part of the equation yielding a radial distribution function r_j term, for EXAFS, compared to the scattering path length difference term $r_j(1 - \cos\theta_j)$, in PhD, which comprises a more complex relationship with both the radial distribution function and the scattering angle θ_j corresponding to the information it conveys; pathlengths and scattering angles [9]. Alternatively, attempts have been made to utilise the fact that the scattered electrons effectively act as a hologram[39, 40]. Due to the increased complexity, as a result of multiple scattering, as opposed to single scattering which is typical of the holographic process, this methodology is unreliable and not the most accurate in the structural information it conveys[9].

A more accurate approach than both of these direct methods is the trial-and-error process which, though not as quick to analyse, can provide meaningful accurate information on the structural information of surface. This involves carrying out multiple-scattering calculations from hypothesised model structures to simulate the theoretical PhD modulations, then comparing with experimental modulations. This often utilises several modulations taken from various azimuthal and polar angles to take advantage of the emission angle dependency, and acquire a larger data set for better identification of the correct structural model.

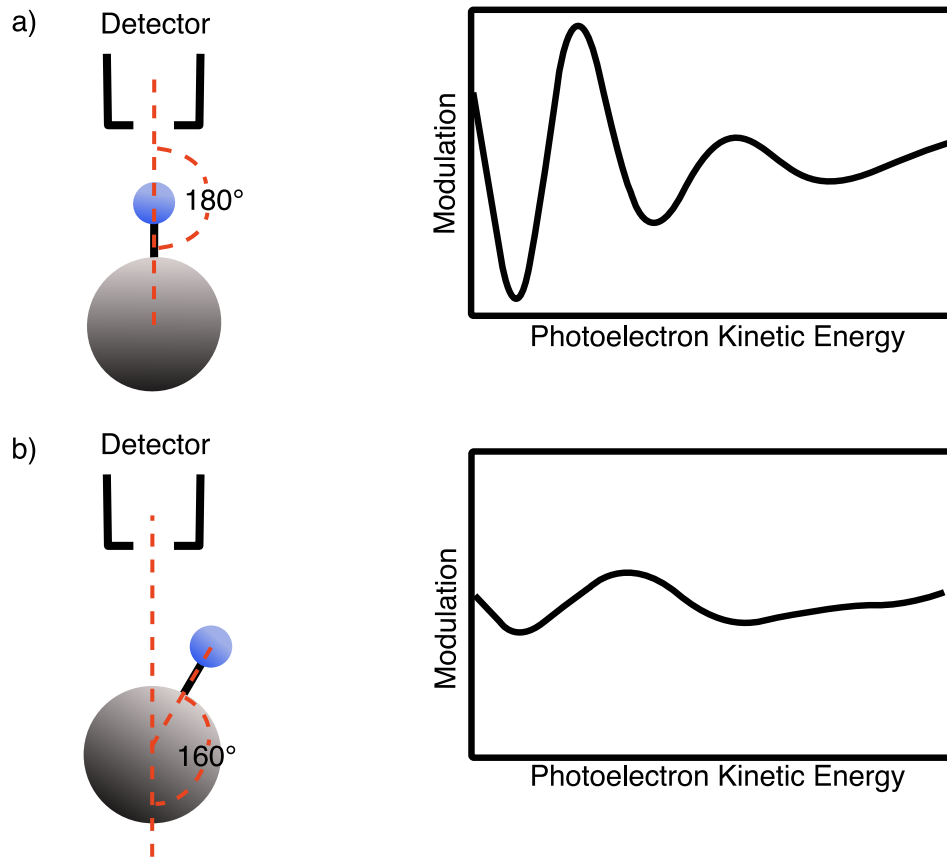


Figure 3.11: Diagram showing the a) 180° backscattering geometry between the Detector, emitter atom (blue), and the scatterer atom (grey), along with a PhD modulation for that geometry and b) highlighting the effect of a slight 20° skew on this geometry on the shape of the resulting PhD modulation.

3.4.2 Qualitative Information

The PhD modulation is made up of the sum of numerous complex scattering pathways. As a result, determining the structure that produces these modulations can be long and painstaking. Without undergoing this process, some parameters of the structure and geometry surrounding the emitter atoms can be determined qualitatively from the overarching features of the modulation. This is primarily because the general shape of any PhD modulation is dominated by the first scattering events involving the nearest neighbour atoms to the emitter atoms. These are the components of the electron wave that are scattered once after emission before arriving at the detector and are the primary sources of modulation in any modulation. Furthermore, the dominant component of these first scattering events are those backscattered by an atom that lies directly behind the emitter atom with respect to the detector at 180° , depicted in **Figure 3.11**, with greater effect, the closer the backscattering atom is to this 180° geometry. This dependence becomes clear when looking at the scattering **equation 3.37**, where each scattering contribution has a prefactor of $\cos\theta_r$ which is greatest when θ_r , the angle relating the scatterer to the emitter, is closest to 180° [9].

When considering a PhD spectrum, one can often predict the geometry of a system, through amplitude of modulations at varying angles of detection. For example, a high amplitude modulation at a particular geometry indicates the presence of a neighbouring atom at or close to 180° with the detector and the emitter. Additionally, when emitters sit on high symmetry sites such as atop or hollow sites, $\sim 30\%$ greater than average amplitude can be expected. Meanwhile on low symmetry sites, a $\sim 20\%$ lower than average amplitude can be expected. Thus, one can sometimes infer the symmetry of a molecule's adsorption site if modulations have particularly high or low amplitudes. Distances and thus bond lengths can sometimes also be inferred from visual analysis of raw PhD modulations as shorter distances between nearest neighbour scatterers will induce longer period modulations, and vice versa, with longer distances with nearest neighbours produces shorter period modulations. Finally, when a PhD spectrum appears to have non-periodic modulations, this is often a result of disorder in the system or is indicative of multiple adsorption geometries on the surface[9].

3.4.3 Multiple-Scattering Calculations

For realistic experimental modulations to be simulated, multiple-scattering must be included in calculation of the theoretical modulation [41, 42, 43, 44]. The photoemitted electron intensity at the detector is defined as:

$$I(E, r) = |\Psi(E, r)|^2 \quad (3.40)$$

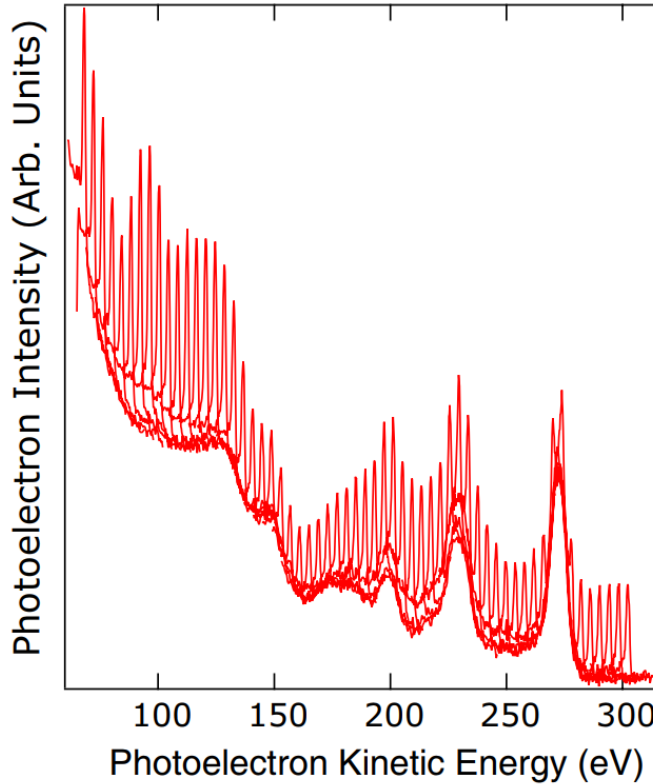


Figure 3.12: Plot of EDC intensity with respect to photoelectron kinetic energy. This being the first step in processing of raw PhD data[10].

where $\psi(E, r)$ is the electron wavefunction with respect to the position of the detector r , and the photoelectron energy E . The electron wavefunction can then be defined as:

$$\Psi(E, r) = \psi(E, r)_0 \int (d^3 r' G(r, r', E) \mathbf{E} p \Psi_0(r')), \quad (3.41)$$

where p is the momentum operator, \mathbf{E} is the vector potential of the photon field, $\Psi_0(r')$ is the wavefunction of the excited core level and $G(r, r', E)$ is the Green's function of the total system. Green's function can then be expanded over all scattering pathways, resulting in a sum of all partial wavefunctions:

$$\Psi(E, r) = \sum_j \psi_j(E, r), \quad (3.42)$$

Where j denotes each individual pathway, $\psi_j(E, r)$ is the partial wavefunctions [43]. Computation of electron scattering is typically done with the plane wave approximation; however, this breaks down when the distance between scattering events is comparable to the wavelength of the electron; to accommodate for this, a more easily computable spherical wave approximation was developed [41] that allows more accurate expansion of scattering events. For an exact solution to this expansion, all possible scattering pathways must be calculated.

Considering that a cluster of 100 atoms would have 10,000 double scattering paths, and 1,000,000 triple scattering paths, it is clear that full calculation would be extremely computationally expensive and time consuming. Through Fritzsch's approximations [41, 42, 43, 44], and parallelisation by Duncan [10, 45] reasonable calculation times are now achieved. One of these being the reduced angular momentum expansion (RAME) which only calculates a limited number of low angular momentum wavefields at high accuracy to energies as low as 40 eV. It is based on the magnitude of scattering phase shifts for higher angular momenta tending towards 0. This allows for a maximum angular momentum (l_{max}), and equivalently, a maximum magnetic quantum number (m_{max}), above which the resulting phase shift for the scattering event is ignored to no substantial effect on the resulting modulation [42]. Another simplification arises from the finite energy resolution of electron analysers and the electrons being damped by inelastic scattering processes, mentioned in section 3.0.1. Consequently, the scattering contribution predominantly originates from elastic scattering in the small region surrounding the emitter atom giving reason to ignore long pathways. Additionally, the contribution for a scattering pathway can be constructed from scattering theory, producing a resulting oscillating wavefunction that has frequency inversely proportional to path length. These high frequency modulations cannot be seen in experimental data as they are averaged out by the small phase differences induced by finite energy resolution of the instrumentation and the life time broadening of the core level accounted for in the following:

$$I(E) \propto \sum_{i,j} \psi_j^*(E) \phi_i(E) f_{Gauss} f_{Lorentz}, \quad (3.43)$$

$$f_{Gauss} = \exp \left[-\sqrt{\frac{m}{8\hbar^2 E \ln 2}} (E_b(R_i - R_j))^2 \right], \quad (3.44)$$

$$f_{Lorentz} = \exp \left[-\sqrt{\frac{m}{2\hbar^2 E}} E_b |R_i - R_j| \right], \quad (3.45)$$

where the summation is over all possible combinations of pathways i and j , E_b is the energy broadening, f_{Gauss} is the Gaussian broadening accounting for the instrumentation, whilst $f_{Lorentz}$ is the Lorentzian broadening to account for the core level life time broadening [10, 43]. It is for the previous reasons, that a maximum of 3 scattering event pathways are considered in the theoretical model; more specifically, the shortest 2000 single, 1000 double, and 1000 triple scattering events are calculated. To further shorten process times, parallelisation of various independent components of the computation such as modulation spectra from each emitter, domain, and direction [10, 45]. Whilst these approximations are convenient in allowing us to calculate a smaller number of scattering pathways, they indicate the limited range around the emitter atom which can be accurately probed, highlighting the surface sensitivity of the PhD technique. For a greater range, more scattering pathways must be calculated, thus the substantially increased computational cost to model the modulations would make

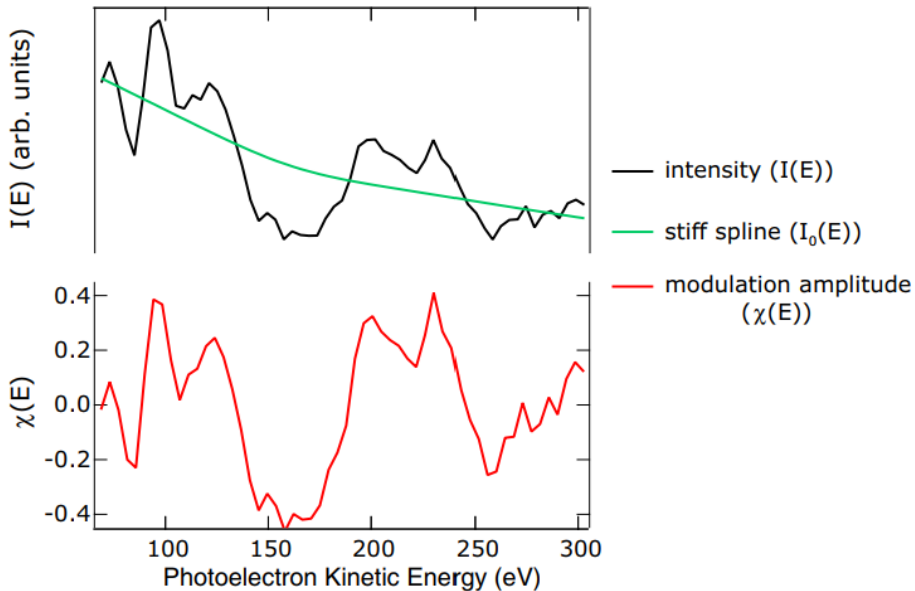


Figure 3.13: Plot of background-adjusted PhD modulation with fitted stiff spline (upper diagram), and final PhD modulation with spline subtracted depicting only diffractive effects [10].

the trial-and-error optimisation unfeasible. Moreover, longer scattering pathways have more negligible contributions to the overall PhD modulation, and so inclusion of them would likely not improve accuracy of calculated modulations substantially.

3.4.4 Data Acquisition & Processing

energy-scanned Photoelectron Diffraction requires a tunable X-ray source, thus it is limited to synchrotron radiation sources. Data is acquired by measuring several soft XPS spectra, also known as energy distribution curves (EDCs), at incremented photon energies ($\sim 50 - 400$ eV with 4 eV step). The EDCs are superimposed onto a PhD intensity versus photoelectron kinetic energy plot, seen in **Figure 3.12**. A template background is modelled from the background tail of the EDCs, and any present Auger peaks in the data are modelled also. These are then subtracted from the intensity modulation to remove background contributions. Then each individual EDC is fitted with a form of a Gaussian distribution with a template background, from which the intensity of the peak is taken as the photoemission intensity for the final modulation. This leaves a plot of photoemission intensity against photoelectron kinetic energy, producing our first visualisation of the oscillation in intensity of the PhD scattering, seen in **Figure 3.13**. To isolate the diffractive signal, a spline is defined to account for effects, such as variation in photoionisation cross-section with photon energy, and also normalise the intensities between the data points. This spline is subtracted from the overall amplitude, seen as the green line in **Figure 3.13**. The final PhD modulation is calculated like so:

$$\chi_{exp}(E) = \frac{I(E) - I_0(E)}{I_0(E)}, \quad (3.46)$$

where $\chi_{exp}(E)$ represents the fractional contribution of diffractive effects to the photoemission spectrum(i.e. the final PhD modulation), $I(E)$ is the photoemission intensity, and $I_0(E)$ is the stiff spline. This process is repeated for each of the measurements at different angles, which is later used to find a theoretical model with as similar a modulation as possible [10, 38].

3.4.5 Assessing & Finding the best fit

Once a theoretical modulation has been computed, it is compared to experimental results. R-factor is utilised as a quantitative quality of fit parameter, developed similarly to that developed for LEED-IV by Pendry [46, 47]:

$$R_f = \frac{\sum(\chi_{exp}(E) - \chi_{theory}(E))^2}{\sum(\chi_{exp}(E)^2 + \chi_{theory}(E)^2)}, \quad (3.47)$$

where both summations are over all measured and computed beams, and χ represents the modulation for theory or experimental. R_f or R factor is the goodness of fit parameter which takes a continuous value between perfect agreement, 0, and anti-correlated results, 2, with values nearing 1 indicating no correlation whatsoever. The R factor was designed to be particularly sensitive to peak positions, not to absolute intensities, and partially to relative peak intensities of neighbouring peaks. It was developed such that it wouldn't involve higher derivatives with respect to energy so as not to require calculations to be made for closely spaced energies to provide sufficient numerical accuracy [46, 47].

One can utilise various automated methods to search the structure space for the best fit according to the R-factor. Unfortunately, the complexity of structures often gives a number of parameters, such as emitter and scatterer position(s), vibrational amplitudes, inner potential etc, creating a many-dimensional hyper space within which a minimum would be computationally expensive to scan through. An alternative approach is to utilise optimisation algorithms to search the hyperspace more efficiently. The simplest of these being a gradient descent, though due to the presence of extensive local minima, this isn't an ideal choice. Alternatively, global search algorithms were identified; methods that have been attempted for PhD include: genetic algorithms (GA) [48] and particle swarm optimisation (PSO) [45, 49], similarly but more extensively LEED-IV has utilised genetic, fast simulated annealing(FSA) [50], and other techniques have been utilised [51]. A comparison of the three revealed that

PSO outperformed the other techniques in PhD optimisation and has thus been utilised in this thesis [10, 45].

newline

For a goodness of fit parameter to be defined properly, a variance in this parameter must be defined to measure the significance of its results. For R factor, its variance is defined like so [45, 46]:

$$\text{var}(R_{\min}) = R_{\min} \sqrt{\frac{2}{N}}, \quad (3.48)$$

where R_{\min} is the minimum calculated R factor, and N is the number of possible independent pieces of structural information contained in the experimental spectra. In the case of Pendry's R-factor, N refers to the number of distinct peaks within the data [46]. Whilst in the PhD adaptation, N is defined as:

$$N = \frac{\delta E}{4\sqrt{V_i^2 + E_b^2}}, \quad (3.49)$$

where δE is the energy range of the spectrum, V_i is the imaginary part of the inner potential of the material, and E_b is the energy broadening factor. This estimates the maximum amount of features, with individual width defined by the accuracy limitations of the experiment through uncertainty introduced by inelastic loss processes (V_i), and inherent energy broadening (E_b). The values for these two parameters are often approximated to 5 eV, making the variance, seen in **Equation 3.48** entirely dependent on reduction of R_{\min} to be minimised.

Any R-factor found within the range of $\text{var}(R_{\min})$ of R_{\min} , can be considered to be within 1 standard deviation of R_{\min} , and thus seen as an acceptable solution. This variance can be used to define uncertainty on a structural parameter by varying the parameter until the R-factor exceeds the range of 1 standard deviation of the minimum. Meanwhile, any secondary minima found outwith this range can be excluded. This variance defines the bounds of the uncertainty on the R-factor. This does not account for systematic error, introduced by inaccurate detector geometry, for example. The effect of a slight difference in angle from expected would be negligible due to the dominance of backscattering on the modulation for a relatively broad angular range surrounding the 180° geometry [47]. Generally, an R factor of between 0.2 and 0.3, over a reasonable number of modulations, shows sufficient agreement such that a model can be said to be comparable to the experimental structure. The quality of data and the amplitude of observed modulations plays a role in this. With lower quality data or smaller amplitude modulations (i.e. ±10%), an R factor closer to 0.3 would be acceptable, whereas with good quality data with minimal noise, and high amplitude modulations, a lower R factor would be required for the model to be valid. Furthermore, once a global minimum has been

found, the structure must be compared to other experimental and supporting information to deduce the validity of the model structure. It is not uncommon for a global minimum of a variable hyperspace to have an impossible atomic structure.

3.4.6 Particle Swarm Optimisation (PSO)

The particle swarm optimisation takes influence from the search patterns of swarming organisms, who will individually search whilst relaying information to other members of the swarm. Each individual will remember relayed information and relay some of their own to improve the speed and quality of search. In the PSO algorithm, a host of variables (e.g. relaxation heights, lattice parameters) will be entered along with bounds for those variables, limiting their range, to then produce a range of starting calculations, unique for each of the 20 – 40 individuals. Individual calculations will begin from a variation on the supplied starting parameters so as to randomise starting points. Functionally, each searching individual will remember the best fit that it is calculated ($X(i)_{local}$) and the best fit it has been informed of from other individuals ($X(i)_{global}$). Together, these are used to determine the parameters/location in variable hyperspace of the subsequent iteration, for each individual, through the following equations:

$$V_{X(i)} = c_p P_p V_{X(i)} + c_{local} P_{local} dX(i)_{local} + c_{global} P_{global} dX(i)_{global} \quad (3.50)$$

$$dX(i)_{local} = X(i)_{local} - X(i), \quad (3.51)$$

$$dX(i)_{global} = X(i)_{global} - X(i), \quad (3.52)$$

The primary equation, **Equation 3.50**, defines the variation of the parameter set in the next iteration, $V_{X(i)}$, and can be split into three terms: The individual's momentum, $c_p P_p V_{X(i)}$, this term controls the dependence on the most recent calculation parameters, $V_{X(i)}$, and can be thought of as its velocity through the variable hyperspace; its Nostalgia, $c_{local} P_{local} dX(i)_{local}$, the term leading the fit towards the individual's best found fit; and its Optimism, the term tending the fit towards global best fit that it has been informed of. $X(i)$ is the current parameter set, defining the location of the individual in variable hyperspace; $X(i)_{local}$ is the location of the best found fit of the individual, and $X(i)_{global}$ is the location of the informed best fit. The "distance" between the individual and its best found, $dX(i)_{local}$, or best informed $dX(i)_{global}$ is proportional to how quickly an individual moves towards those points. The P prefactors take random values between 0 and 1 to introduce randomness in the optimisation and prevent premature convergence and convergence between individuals. Meanwhile the C prefactors are weighting factors that control the dominance of each of the terms in **Equation 3.50**. The importance of these prefactors is vital, for example, C_p , if too large, will give the individual too much momentum that it will never stabilise into a minima; whereas C_{local} and

C_{global} are kept at similar values and not too small to allow the individual to escape local minima and explore surrounding regions.

A key parameter not included in any of these equations is K, the number of randomly selected individuals that will inform the individual of their local best found fit. This one-way passage of information directly controls how quickly convergence will occur. Too small, and information will not be passed on effectively and convergence will be too slow. Too large, and convergence will occur too early, before the true global minima is found [10, 45].

3.5 Scanning Tunnelling Microscopy

Since the discovery of STM by Binnig and Rohrer in 1982 [52], the whole research area of scanning probe microscopy has revolutionised the field of surface science, providing a tool for precise study of surface structure but also a technique for atomic manipulation of surfaces [19, 53]. All scanning probe techniques involve an atomically sharp tip being taken close to a surface, then a measurement is made through some property that indicates the distance between the tip and the surface. Scanning tunnelling microscopy (STM) measures this distance through an electron tunnelling current with constant voltage, or vice versa, between a conductive tip and surface, this tip is then rastered across the surface producing a 3D image of the surface through the electronic states of the surface. The differences between these two methods of STM are depicted in in **Figure 3.14**

The tunnelling of electrons between the tip and the surface can be modelled as tunneling of an electron through a potential barrier, potential wells on either side of different energies, defined by their Fermi energies. Considering a 1-Dimensional, 1 electron model, the electron has a wavefunction in either of the wells, which decays exponentially as it enters the potential barrier. If, however, the barrier is sufficiently small and the energy of the electron wavefunction is sufficiently large, then it is possible for the two wavefunctions in either well to overlap within the barrier, consequently tunneling can occur between the two sides of the well and current can flow. The decay of the wavefunction is governed by their decay length, κ :

$$\kappa^2 = \frac{2m}{\hbar^2}(E_{barrier} - E), \quad (3.53)$$

where m is mass of the electron, \hbar is reduced Planck's constant, $E_{barrier}$ is barrier height(vacuum level), and E is energy of the electron. At low temperatures and voltages, the tunnelling current depends on the decay length and separation of the tip and the surface, d , like so:

$$I \propto e^{-2\kappa d}, \quad (3.54)$$

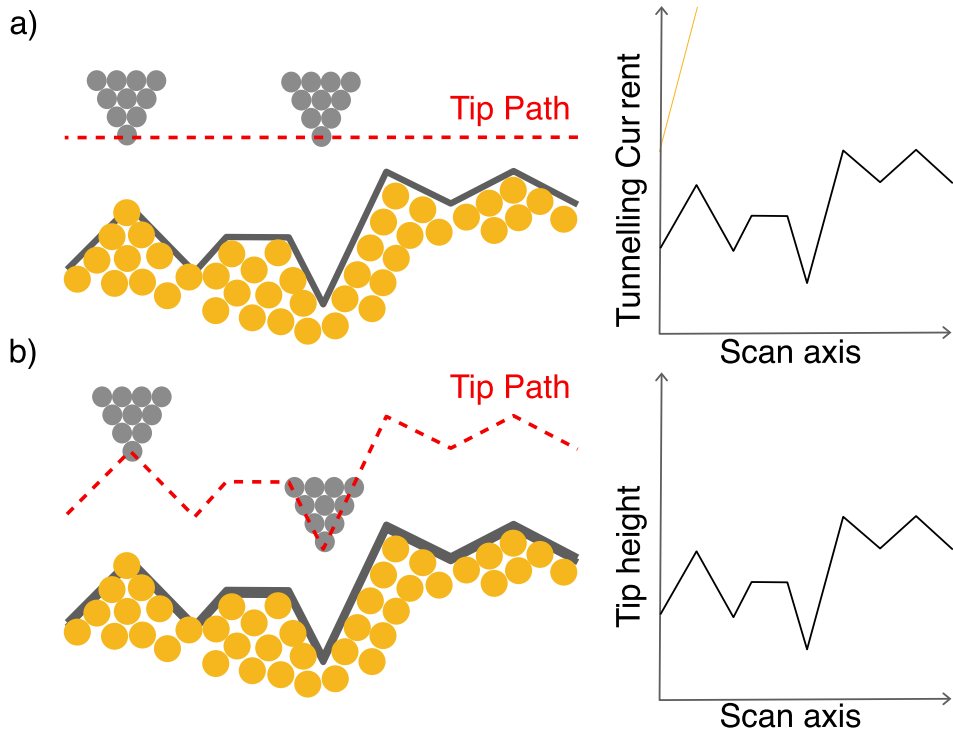


Figure 3.14: Diagram of the measurement of an STM linescan in a) constant height mode, and in b) constant current mode, along with the resulting plot of the 2D linescan from the respective method to their right.

where κ is in the range of 1 \AA , a difference in separation of 1 \AA leads to an order of magnitude reduction in tunnelling current. This is the basis for STM; where the tip is scanned across the surface whilst the height of the tip is adjusted through a feedback loop to maintain constant tunnelling current. Alternatively, one can maintain constant height and constant voltage, while the current is measured. Each line scan is then compiled to produce a 3-D image of the surface, specifically a convolution between the physical and electronic structure, though only the constant current method was utilised in my work. Elaborating on the constant current mode, the tip is lowered until a tunnelling current is measured at a reasonable voltage between 1 mV and 2 V , where a tunnelling current on the scale of nA is measurable. A diagram comparing the two methods can be seen in **Figure 3.14**. The resulting raw STM image of height versus position will have various distortions that must be corrected for in the data processing phase. For example, when manoeuvring the STM tip, the tip often rotates a small angle in the direction it is moving; resulting in an image that looks bowed, and taller at the sides. Additionally, it is common for the motors controlling the tip to be imperfectly calibrated, in which case, there is often a drift in the image after each scan [25]. Leveling of data, alignment of rows, as well as selection and adjustment of a colour scheme is typically carried out using software. For example, Gwyddion 2.61 was used in the following studies.

3.5.1 Moire Patterns in STM

Generally, Moire patterns are interference patterns that appear as a result of two periodic structures being overlaid on one another. These two patterns must either, not be identical, and/or have a slight displacement, rotation, or pitch. The implication of this for STM is in the overlaying of an overlayer lattice upon a substrate lattice.

A popular example of this is graphene on metal surface. For example, graphene on copper (111). Here, both graphene and the Cu(111) surface have a hexagonal structure, however, the bond lengths of the hexagonal patterns are not identical. Consequently, the lattices between the two, even if they are aligned in rotation and pitch, have a slight mismatch; where carbon atoms of the graphene are sitting on varying sites(i.e. hcp, top, fcc, or otherwise) on the copper surface within a large combined unit cell. At each of these sites, different parts of the lattice interact more or less strongly, occurring in a periodic fashion within this larger unit cell. In STM, hexagonal corrugation of the 2D carbon surface is seen, with different periodicity and angle depending on the angular difference between the graphene and the Cu(111) surface [54, 55].

Chapter 4

Azupyrene and Pyrene on Cu (111) for the synthesis of graphene

4.1 Introduction

This chapter describes the surface study of graphene produced using topological design, utilising selected alternant and non-alternant aromatic molecules: pyrene and azupyrene, and probing their growth processes during epitaxial growth on copper(111) in UHV with techniques such XPS, XSW, STM, and LEED. Understanding the growth mechanism for the differing molecules will shine light on the differences between alternant and non-alternant reagent produced graphene, with potential for revealing a mechanism of synthesising defect-containing graphene with the goal of controlling defect concentrations, and later utilising them as sites for single atom catalysts.

Single Atom Catalysis (SAC)

Development of chemical processes in the modern day are done with the aims of greener, more sustainable, and economical methods. These are paired with the general aims of greater efficiency and selectivity that can allow for more precise reaction pathways that could, for example, help to reduce undesirable and often environmentally harmful side products. A fundamental component of these processes are the heterogenous catalysts which accelerate these reactions; some of the most efficient of which are built upon nanostructured substrates, which have structural elements between 100 and 1 nm in size. These are already of great interest and application; often utilising the unique electric, magnetic, and optical properties of the substrate which can have valuable effects, for example, specific control over selectivity of active sites [19]. When catalyst atoms are distributed on a substrate, they have a tendency to group together and form nanoclusters. Efficient spread of these catalyst atoms into smaller nanoclusters is controlled by the substrate; improved catalyst reactivity and reaction selectiv-

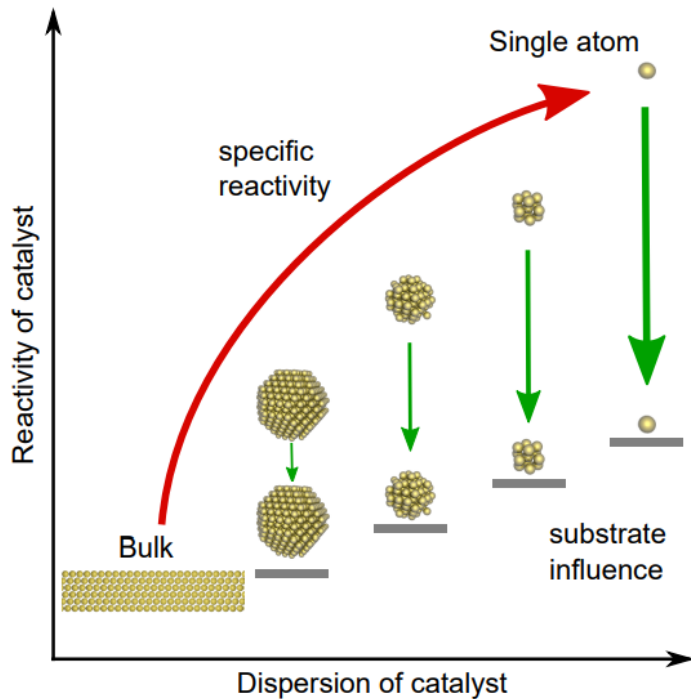


Figure 4.1: Plot depicting specific reactivity of catalyst versus catalyst dispersion, alongside the relationship between dispersion of catalyst with influence of substrate [11].

ity can thus be achieved by discovery and development of novel substrates. This relationship is conveyed in **Figure 4.1**, displaying the improvement in specific reactivity (reactivity per unit catalyst) and substrate influence, as the dispersion of catalyst atom on the substrate increases. It is clear from this figure, that single atom dispersion could provide the greatest reactivity and thus efficiency per catalyst atom. SAC, or single atom catalysis, refers to the dispersion of single atoms across a substrate to achieve this improved functionality. Unfortunately, it becomes increasingly difficult to stabilise greater dispersion of catalyst atoms, becoming predominantly dependent on substrate. It is thus clear that supporting single catalyst atoms on a surface is extremely difficult, requiring unique, exceptional substrates, to prevent conglomeration, forming larger, less efficient nanoclusters, particularly in typical reaction conditions at elevated temperatures of several hundreds of degrees Celsius. It is an aim of SAC research to find a suitable substrate that can host lone catalyst atoms distributed in as high quantities as possible across its surface. Some investigated mediums include: metal oxides like iron oxides, on which single platinum atoms have been stabilised, or rhenium atoms on zinc oxide; metal carbides such as platinum on tungsten carbide; and even on graphene and graphene-like systems [56, 57, 58, 59, 60]. Previous studies have shown that metal atoms have a tendency to become trapped or pinned to defect sites in graphene due to a greater electron density [60]. This study aims to investigate the synthesis process of graphene prepared using a non-alternant molecule, azupyrene, in comparison to an alternant one, pyrene, seen in **Figure 4.3a** and **4.3b**, respectively. With an aim of understanding the effect of this on the

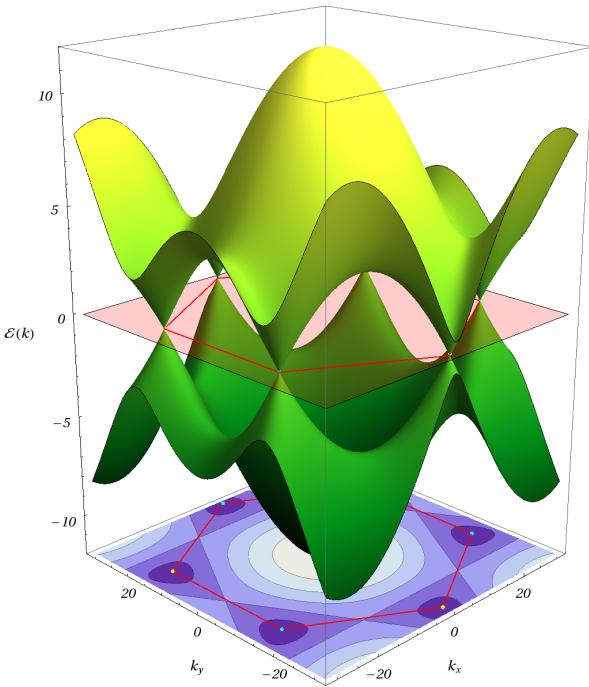
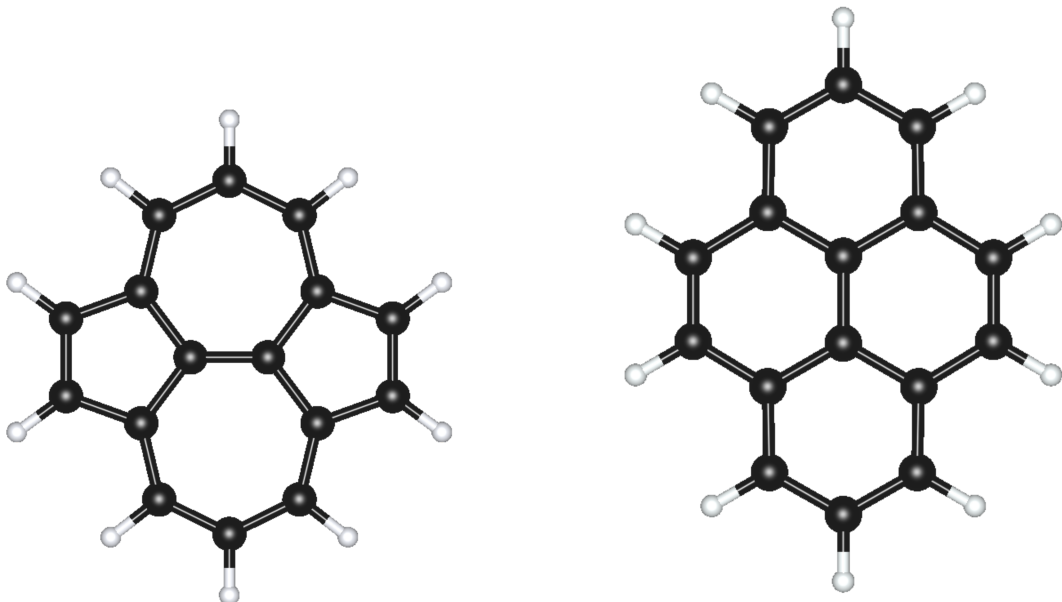


Figure 4.2: The Fermi surface of graphene in a nearest neighbour tight-binding model [12, 13]

resulting graphene. If changes the concentration of defects, specifically Stone-Wales defects in azupyrene syntheses can be controlled and optimised there could be potential for development of a new synthesis method for graphene as a substrate for single atom catalysis [60]. This is discussed in more detail later in this chapter.

Graphene

Graphene is a 2-dimensional lattice of sp^2 hybridised carbon atoms arranged in a hexagonal network. It has been one of the most researched modern materials, particularly since its first synthesis using the mechanical exfoliation method by K. Novoselov and A. Geim [17]. Prior to its discovery, graphene's unique, and potentially revolutionary properties had been theorised, but its existence was believed to be impossible due to thermal fluctuations [61]. Some of the most notable properties of graphene are its intrinsic strength, high charge carrier mobility and thermal conductivity, higher than all other tested materials, in addition to its great chemical stability [62, 63, 64, 65]. These give rise to a wide range of potential applications from energy storage, to heterogenous catalysis [66]. Many of these excellent physical and chemical properties stem from the carbon sp^2 hybridisation that, in aromatics, forms a pseudo-delocalised cloud of electrons above and below the planar structure, stabilised by the coupling between neighbouring π orbitals within the cyclic aromatic ring. Meanwhile in graphene, bands form corresponding to the bonding and antibonding π and π^* molecular orbitals. The result of which produces a Fermi surface seen in the 2-dimensional k-space plot depicted in **Figure 4.2**. Here we see the meeting on the upper (electrons/ π^*)



(a) Structure of azupyrene. Azupyrene is composed of two 5-membered and two 7-membered rings, giving it a non-alternant topology.

(b) Structure of pyrene. Pyrene is composed of 4 benzoid rings, with an alternant topology.

Figure 4.3: Diagrams of the structures of azupyrene and pyrene molecules.

and lower (holes/ π) bands at Dirac cones situated at the corners of the k-space hexagonal lattice. Through computation of the Schrodinger equation, using a single particle model, it can be found that the energy at these meeting points is 0. Therefore, the two bands are split at the Fermi level, through which electrons require no excitation energy to move. This gives rise to the delocalisation of electrons across the graphene surface, massless relativistic charge carriers, the quantum hall effect, and more. These effects are only reinforced by graphene's high stability, thus low defect probability; which lowers the rate of electron wave disruption within the material [14, 67].

Defects in graphene

The majority of the outstanding properties that led to the prominence of graphene research are due to its naturally low defect concentrations, many potential applications for graphene involve utilisation of introduced structural defects and impurities. It is hence important to understand the types and properties of the defects present within graphene. It can be difficult to determine accurate measures of the nature of defects experimentally. Thus, theoretical calculations, using DFT methods, can be done to estimate their stability through their formation energies (E_{form}) and migration barrier (E_m). These energies were obtained from the total energy of a supercell containing the defect of interest:

$$E_{form} = E_d - E_{bulk} - n\mu \quad (4.1)$$

Where E_d is the total energy of the defective supercell, E_{bulk} is the total energy of the graphite substrate, and n is the number of carbon atoms that were added or removed from the structure multiplied by μ , the chemical potential of carbon [68, 69]. Determination of migration barrier involved either calculation of energies of known migration paths, prediction of the reaction coordinate through hypothesized transition states (drag method), or methods where the reaction coordinate is determined mathematically (nudged elastic band method) [14, 70, 71, 72].

The 2D nature of graphene's structure gives graphene its unique properties whilst limiting the possible type of defects that can exist within it. Ideal graphene's high carrier mobility that results in its hallmark quantum Hall effect and ballistic electron propagation at room temperature, is dependent on its low concentration of defects that would disrupt electron waves through the material. Similarly, adatoms and even clusters have been found to be very mobile on graphene's surface but stabilised at defects [73]. Single Vacancies (SV), are the simplest of the defects resulting from removal of a carbon atom, as seen in **Figure 4.4 a)**. The resulting 5-9 membered ring structure is particularly unstable due to the under-coordinated carbon atom, giving a comparatively high E_{form} 7.5 eV and a low E_m of 1.3 eV allowing migration at temperatures above 100°C. Stone-Wales (SW) defects, **Figure 4.4 b)**, have a lower formation energy ($E_{form} = 5$ eV) thanks to their lack of dangling bond. These defects involve effectively rotating the central C-C bond 90°, maintaining stoichiometry and resulting in a pair of two alternated 5 and 7 membered rings [74]. Its high formation energy leads to low concentrations of SW defects in typical experimental temperatures of below 1000°C. However, their reverse transformation has an energy barrier of 5 eV, meaning that once the defect is formed, stability is expected below 1000°C [75]. In general, introductions of pentagons into the graphene lattice leads to positive curvature/protrusion out of the surface, whilst, the heptagons lead to negative curvature/depression into the surface [76, 77]. In SW defects and other symmetrical arrangements, these effects compensate for each other maintaining stability of the defect within the planar, ideal graphene lattice despite having a non-planar local environment. [14]

Multiple vacancies (MV) are of particular interest due to their reduced E_{form} :Number of vacancies ratio. Double vacancies (DV), where two carbon atoms have been removed from the lattice, have a similar total E_{form} to SV ($E_{form} \approx 8$ eV) thanks to their 5-8-5 structure and lack of dangling bonds seen in 4.4 c). Thus the existence of 1 DV is nearly thermodynamically more favourable than 1 SV, and significantly more favourable than 2 individual SVs. Whilst spontaneous formation of double vacancies in the lattice will be unlikely, the large gain in energy from coalescence of two sufficiently mobile single vacancies would make this mechanism a much more common means of DV formation (only in single walled nanotubes). The

following notation: 5-8-5 refers to the defect being made up of a 5, an 8, and a 5 membered carbon ring; this does not necessarily indicate the arrangement of these rings. Upon rotation of a bond in the 5-8-5 structure, just as in SW defect formation, a more stable 555-777 defect is produced, and furthermore, a 5555-6-7777 defect. The 555-777 is of interest as it has a 1 eV lower formation energy than the 5-8-5 defect. These multi-vacancies have much higher migration energies and thus are practically immobile in comparison to single vacancies (7 eV >>> 1.3 eV) [14, 78].

These various vacancies break the uniformity of the ideal graphene lattice, leading to protrusions and depressions within the layer, but also increased electron density due to this separation allowing sole π orbitals to extend out of the surface. This can give rise to increased reactivity, for example, adsorption and substitution of foreign atoms onto/into these defect sites. Adatoms will either physisorb via van der Waals bonding or for stronger covalent bonding interactions, chemisorption will occur with the graphene surface. In the latter case, the adatom will typically sit in a high symmetry position such as atop a carbon atom or in the centre of a hexagonal unit [79]. Even these bonds are relatively weak; with migration barriers of between 0.2 – 0.8 eV for various transition metals, according to various theoretical studies [79]. Transition metal (TM) adatoms, which have much larger atomic radius and a greater number of valence electrons than most elements, have been found to be able to be pinned by structural defect sites (Binding energy \approx 2 eV) [80] thanks to their increased electron density and thus reactivity. This is sufficient for stable trapping at up to 200°C [79]. Furthermore, foreign atoms can and will be substituted into the lattice; most easily at under coordinated C atoms and electron dense regions. For atomically similar elements such as boron and nitrogen, substitution is particularly viable due to the similar atomic radius, and only slight difference in number of electrons [14, 81]. TM atoms tend to form covalent bonds at single and double vacancies due to their greater reactivity. The resulting complexes, seen in **Figure 4.4**, have binding energies ranging between 2 and 8 eV. This could be sufficient for the purposes of hosting catalyst TM atoms for SAC.

Synthesis Methods of Graphene

Since the mechanical exfoliation method was first discovered, a range of techniques have been developed to synthesise graphene of varying levels of thickness (multilayer, bilayer, monolayer, sub-monolayer), purity, and quantity. For the purposes of surface and fundamental structure analysis, reproducible and compliant methods are required, particularly for monolayer and sub-monolayer study. In this use-case, epitaxial methods and mechanical methods are common [82]. For the purposes of this study, however, Epitaxial Growth was chosen. This is because of its reproducibility as a technique that allows accurate control over experimental conditions to vary sample properties, also allowing easy production of sub-

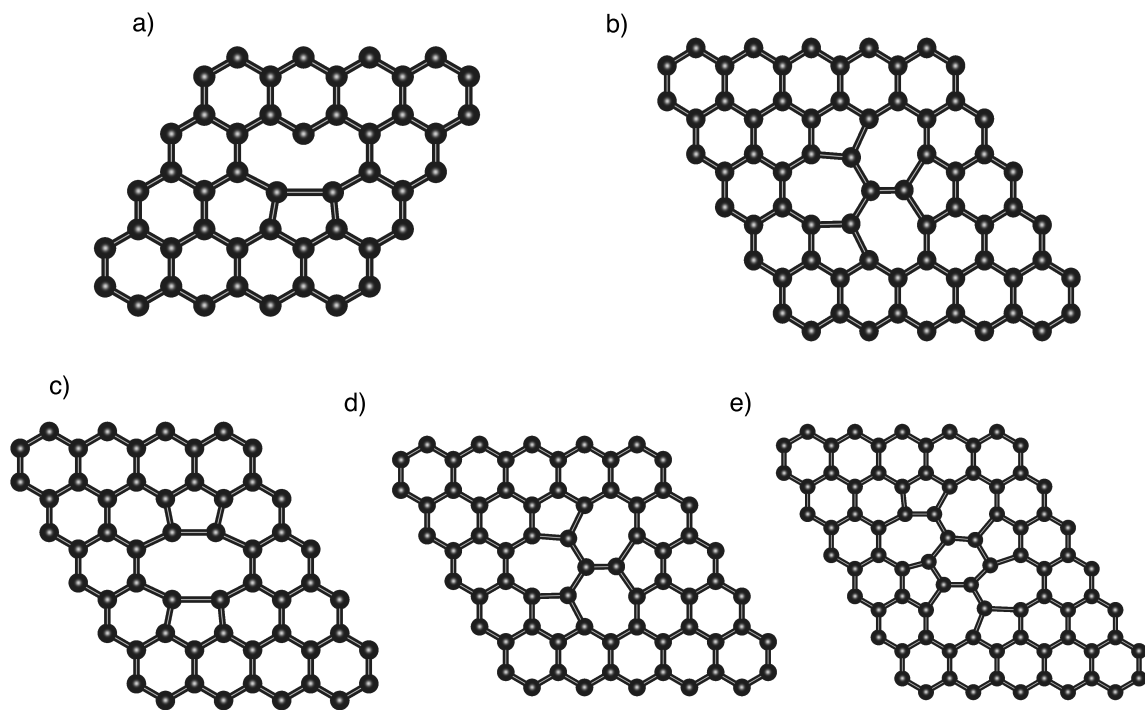


Figure 4.4: Depiction of different types of some of the types of possible defects in graphene.
a) Single Vacancy. b) Stone-Wales Defect. c) 5-8-5 MV. d) 555-777 MV. e) 5555-6-7777 MV [14]

monolayer molecular coverage. Sub-monolayer coverage being incomplete coverage of the copper surface with regions of graphene.

Epitaxial growth of graphene with hydrocarbons on Cu(111)

Epitaxial growth is formation of a crystalline film with a defined orientation(s) onto a substrate. In the case of this study, this process is done through a molecular beam, in ultra high vacuum, depositing molecules onto a heated substrate. The process by which this occurs is of high regularity allowing for fine control over layer thickness and other preparation parameters. It is this one of the most prominent techniques used for UHV surface science [83, 84].

The current accepted mechanism for graphene formation on most transition metals describes the dissociation of carbon from supplied hydrocarbons; chemisorption into the crystal, dehydrogenation of the molecules and dissociation into carbon atoms; then diffusion into the bulk metal before eventual diffusion to the surface once the temperature-dependent threshold for nucleation has been reached through sufficient concentration of carbon within the bulk. Finally, the precipitation process for graphene formation occurs on the surface [85]. Copper is unique in this regard in that it has a low solubility [86] and high diffusion barrier [87] for carbon. Thus, the mechanism by which graphene forms on copper is believed to be dominated by carbon reactant kinetics at the copper surface described by the Gompertzian sigmoidal growth kinetics. A modified Gompertz function can be used to describe graphene flake growth [88]:

$$A(t) = A_{max} \exp \left\{ -\exp \left[-\frac{\mu_m e}{A_{max}} (t - \lambda) + 1 \right] \right\} \quad (4.2)$$

A being the flake area (μm^2), A_{max} the maximum flake area at growth saturation (μm^2), A_{max} , μ_m the maximum growth rate(dA/dt), λ the time lag (minutes), and t the growth time (minutes). Key features of this model are that it does not take into account crystal orientation as this is believed to be independent of the growth rate. It differs from other models [85, 89] in that growth duration is determined by hydrocarbon exposure and not total duration at growth temperature (which would be the case for carbon diffusion out of the crystal). The process can be described like so; supply and adsorption of hydrocarbons onto the surface till supersaturation; meanwhile dissociation and dehydrogenation of hydrocarbons is occurring; nucleation phase begins after which graphene growth is continual from these nucleation site, dominated by continual adsorption of hydrocarbon; some secondary nucleation occurs but graphene growth is dominated by first nucleation; gradually full coverage of surface is reached with majority monolayer (98 + %) [88]. Nucleation is limited by copper sublimation leading to an inverse relation between growth temperature and nucleation site density. Mean-

while, the rate limiting step would appear to be dehydrogenation of adsorbed hydrocarbons, as opposed to diffusion out of bulk.

The differing growth mechanism of graphene on copper(111) made it an interesting candidate for study. Whilst the 2D nature of graphene makes it suited for study using surface analysis techniques, its selection as a substrate was also due to its relevance to chemical industry as a low cost, relatively easily scaled, and intermediate reactivity as a transition metal that would maintain adsorption of azupyrene at graphene growth temperatures greater than 1000°C but weakly bound enough to allow adsorbate movement required for the graphene growth mechanism [85].

4.2 Methods

4.2.1 Equipment

When carrying out epitaxial growth, a doser is chosen to supply the desired flux of a molecule/evaporant. Depending on the vapor pressure of the evaporant, an evaporant can require a different valve or control of temperature to achieve a desired molecular flux.

Line-of-sight doser (LOSE)

Azupyrene has an intermediate vapour pressure that is too low to be leaked in using a leak valve but too high to be evaporated using an organic evaporator. Steady evaporation of azupyrene was achieved using a LOSE. The LOSE utilised at I09 is made up of a glass crucible with a modular temperature control device that can heat or cool molecules using a peltier element controlled by an external power supply, along with water cooling if cooling is required. The molecular flux can then be directed on a precise area with the UHV chamber through a specially manufactured, unreactive glass capillary that can be wound into or out of the chamber to control the spread of the flux onto the crystal substrate. The glass capillary provides a less reactive direction mechanism than a LOSE which utilises a metal capillary tube.

4.2.2 Synthesis Procedure

All of the XPS, XSW, and LEED data in this section was collected in experimental hutch 2 (EH2) of the I09 Beamline at the Diamond Light Source Synchrotron; whilst the STM was measured at the Surface and Interface Laboratory, also at Diamond Light Source. The following procedures are a result of 2.5 years of research in an ongoing project involving numerous

staff at I09, and collaborators. Furthermore, some of the results displayed in this section were collected before my involvement in the research. Specifically, the data of XPS spectrum a) of **Figure 4.8 & 4.9**, and NIXSW spectra a), b), and c) of **Figure 4.10**.

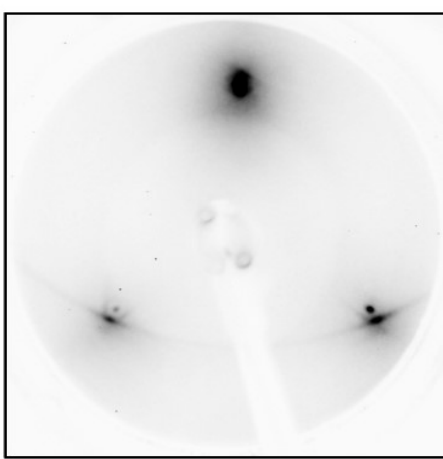
Crystals were cleaned using an Ar gas line attached to a leak valve, paired with an ion gun to sputter the crystals. Sputtered crystals were then annealed to $\sim 700^\circ\text{C}$ using the heaters built into the respective manipulators, though the majority of preparations were completely in SPC2 which utilises a resistive heater. Preparations were carried out with the LOSE onto Cu(111) single crystals at varying temperatures. See **Section 2.2** for more details on the I09 end-station.

Initially, synthesis methods were varied to identify a preferred procedure. For example, depositing onto a cold crystal then post-annealing was found to reduce molecular coverage substantially and uncontrollably thus continuous deposition at temperature was selected. Deposition of molecule was done using the LOSE, with slightly elevated evaporant temperatures ($30 - 40^\circ\text{C}$). Before the first deposition for any experimental period, the molecule was opened to the chamber for at least 30 minutes to allow molecules to coat the quartz tube within the LOSE so that a more consistent flux was achieved during depositions. Evaporant temperatures for the LOSE were aimed to be kept constant, as were coverages, however, preparations were carried out in the different UHV systems of the Surfaces and Interfaces lab and I09, and so acquiring consistent and equivalent coverages were less similar between systems. Between beamtimes in which measurements were made, initial rough calibration preparations were made and measured with XPS to ensure consistent coverages. Crystal temperature was the key experimental parameter that was changed between preparations, to study the different stages of growth mechanism with different thermal energy.

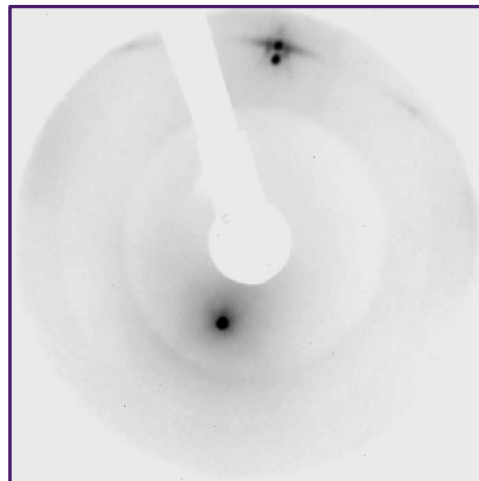
4.2.3 Analysis Techniques

Soft XPS measurements were taken for greater surface sensitivity. C 1s spectra were measured at 430 eV. After each change in photon energy, the Fermi edge was measured to allow correction to binding energies for any slight variations in photon energy during energy moves. NIXSW on the Cu(111) surface was used to determine coherent position and fraction of the Carbon atoms in relation to the surface plane, and the specific adsorption height was determined using the d separation of the Cu(111) plane ($d_{111} = 2.0871\text{\AA}$). Due to the mechanism of the technique, this only indicates whether the carbon is at $(n + P_h) \times d_{111}$, where n is an integer. Included in the NIXSW cycles were reflectivity measurements to check crystal quality at that spot, and HAXPES was used for an C 1s XPS before and after an XSW to check for potential beam damage indicated by a difference in intensity [90]. NIXSW data was fitted using a script written by David A. Duncan, and adapted for this work.

XPS peaks were fitted using the Wavemetrics XPST module designed for IGOR Pro 9.0 [91].



(a) LEED image taken at 49 eV of azupyrene produced graphene.



(b) LEED image taken at 56 eV of pyrene produced graphene.

Figure 4.5: LEED images of azupyrene and pyrene produced graphene displaying the characteristic graphene arc surrounding the Cu (111) reciprocal lattice points [5].

STM data were acquired using an Omicron VT XA STM at room temperature in the UHV chamber of the Surfaces and Interfaces lab at Diamond Light Source. Chemically etched tungsten STM tips were used for the displayed images. They were first conditioned using a clean Au(111) sample using voltage pulses of varying strength.

4.3 Results & Discussion

Initial growths at higher temperatures were carried out to confirm that epitaxial growth was possible on a copper(111) surface for both of the molecules. LEED provided a quick means for doing so; by searching for the existence of the characteristic circular arc surrounding the Cu(111) diffraction spots that is present with graphene [5]. In both pyrene and azupyrene, this pattern was found. These images are displayed in **Figure 4.5b** and **Figure 4.5a**, respectively. This indicated the possibility of existence of graphene upon the surface. Furthermore, STM images were taken of samples prepared at similar temperatures from the two molecules, with 870 K preparation of azupyrene, seen in **Figure 4.6**, and a \sim 970 K preparation of pyrene, seen in **Figure 4.7**.

Figure 4.6 depicts growth of the azupyrene network from islands, two of which are seen in the centre of the image with flat centres and textured edges indicating consistent and varied physical and electronic structure within these islands. This flatness in the STM image could be interpreted as the centres of the islands having a more uniform, graphene-like property, whilst growth of the islands occurs outward from the edges of the island. The evidence of

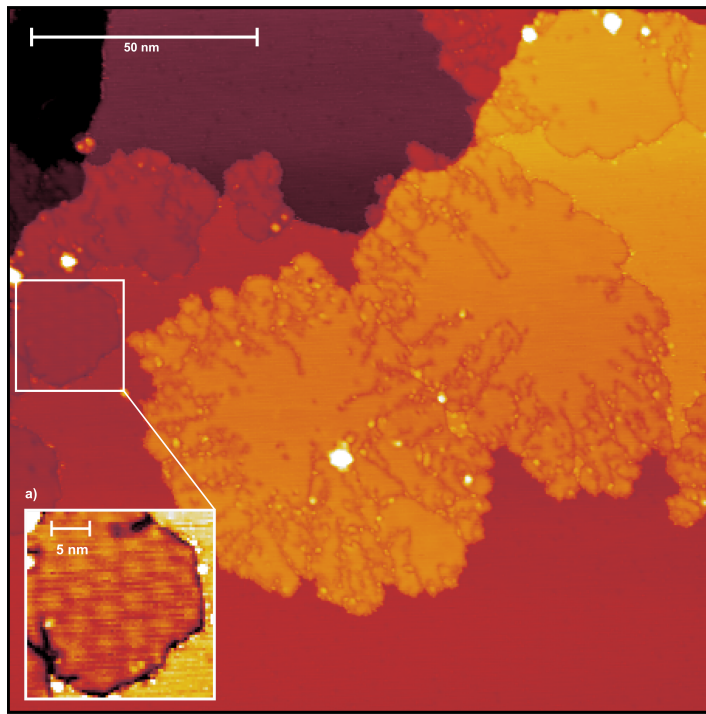


Figure 4.6: STM of a 2D Island preparation of graphene from Azupyrene at 870 K. Image was taken at 1 V, with a current of 1 nA. a) Improved contrast image of moire pattern from graphene.

graphene is confirmed by the region highlighted in white, and scaled up in the inset; within which a hexagonal Moire pattern is visible. This pattern, described in **Section 3.5.1**, is characteristic of ideal graphene on the Cu(111) surface, further confirming the synthesis of graphene by azupyrene on Cu(111) at this temperature range [92]. The nature of the textured edges surrounding the islands is also of interest with large changes in electron density, appearing to spread outward in a dendritic fashion from the islands. This growth also appears to stem from the terrace edges of the copper crystal and was present in both of these environments in numerous preparations of azupyrene.

Figure 4.7 is a larger scale STM image of a higher temperature preparation of pyrene, depicting larger islands, with a clear Moire pattern. The extensive presence of this Moire pattern is the result of the misaligned hexagonal lattices, likely of synthesised graphene and copper. This type of Moire pattern has also been seen in other studies of graphene on copper[92]. Less prominent in the pyrene growth is growth stemming from the copper terrace. Notably, the copper surface is covered in numerous triangular oligomers in the pyrene preparation, highlighted in inset a) of **Figure 4.7**. Whilst exact size of these molecules cannot be determined accurately at this scale of STM image, a rough estimate would put them at ~ 4 nm, on the scale of multiple pyrene molecules. Its triangular general shape is indicative of it be-

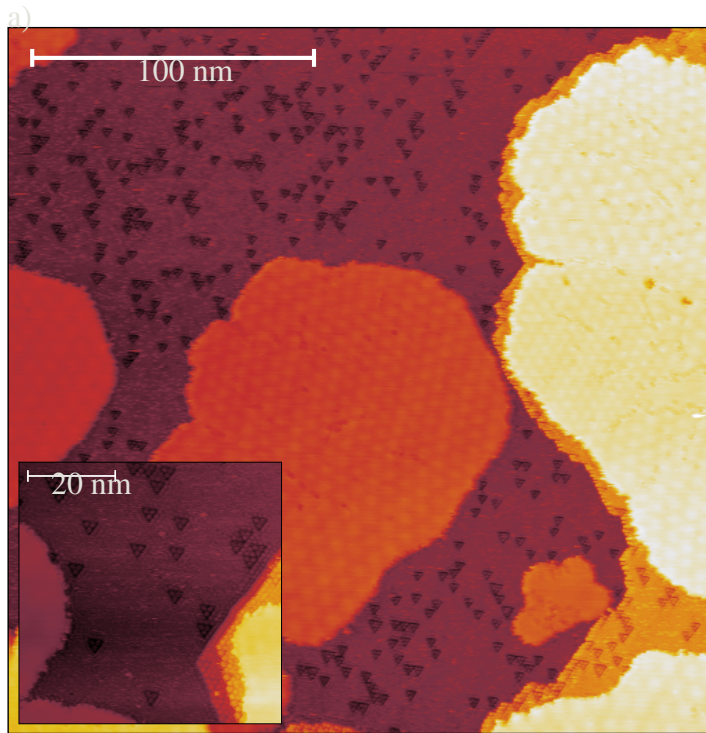


Figure 4.7: STM of a molecular preparation of graphene from pyrene between 870 K and 1070 K. Image was taken at 1.5 V, with a current of 0.3 nA.

ing a trimer of pyrene molecules. The existence of these trimers at such a high preparation temperature may be evidence of their stability and their interaction with the surface being sufficiently strong so as not to desorb upon heating. Alternatively, it may be the result of molecules remaining in the UHV chamber whilst the crystal was cooling, then adsorbing at a lower temperature and oligomerising into the trimer form.

Whilst pyrene preparations were carried out in smaller quantities, numerous preparations of azupyrene have been studied with STM allowing different temperature ranges to be classified into 4 growth stages by which they will be further referenced: Molecular, Dendritic, 2D Islands, and Ideal. The same was not done with pyrene due to insufficient STM analysis, and as a result of failure of equipment during the research. Some XPS and NEXAFS analysis was done on varying temperature preparations at the MAX IV synchrotron, however, no substantial changes were seen, suggesting fewer growth phases for pyrene.

Further analysis of these preparations was carried out using XPS, specifically the C 1s peak using soft X-rays, the results of which are displayed in **Figure 4.9** for pyrene and **Figure 4.8** for azupyrene, with peak fitting parameters tabulated in **table 4.2** and **table 4.1**, respectively. NIXSW was also completed for the C 1s peak, the spectra of these are displayed in **Figure 4.11 & 4.10** for pyrene and azupyrene, respectively, the results of which were tabulated in **table 4.4 & 4.3**.

4.3.1 Molecular

The XP spectra of molecular azupyrene on Cu(111), is shown in spectra a) of **Figure 4.8**; whilst the specific fitting parameters of these are found **table 4.1**. Meanwhile, the XP spectra for molecular pyrene can be seen in spectra a) of **Figure 4.9**, with the fitting parameters denoted in **table 4.2**. Comparing the binding energies of the two component peaks of molecular azupyrene and pyrene; azupyrene is lower at 284.35 eV and 283.96, relative to that of pyrene at 284.81 eV and 284.40 eV. The reduced binding energy of the azupyrene chemical environments indicates greater interaction with the metal crystal. Thus the lower binding energy of azupyrene would indicate that it is closer bound to the crystal, interacting more strongly. Previously studies have shown that non-alternant molecules interact more strongly with metal surfaces due to hybridisation of their molecular π orbitals with electronic states of the metal surface [6, 93, 94, 95]. These results would support these studies. Furthermore, there is a greater asymmetry of both azupyrene peaks relative to that of pyrene; 0.22 and 0.22 compared to 0.14 and 0.20, for primary and secondary peaks. As discussed in **Section 3.2**, asymmetry of an XPS peak is a result of final state effects, some of which are proportional to the interaction of an adsorbate with a source of electrons(i.e. the metal surface [34]). This theory would imply that the greater asymmetry of azupyrene peaks would be a result of greater interaction with the surface, supporting the aforementioned theory of non-alternant molecules interacting more strongly with metal surfaces. Individual peak widths for both molecules are similar, around ~ 0.6 ev for both peaks of both molecules which is to be expected for simple molecules containing few different chemical environments, that are sitting unreacted upon a surface.

The presence of 2 peaks within the azupyrene XP spectra can be explained by these previous studies also. Using DFT simulation of a similar non-alternant molecule to azupyrene, azulene, which is made up of a single pair of 5-7 membered rings, this study predicted electron donation from the metal surface to the non-alternant azulene, leading to negative charging and deformation of the azulene to form more distinct chemical environments interacting differently with the surface and sitting at different adsorption heights [95]. This may be a result of the multiple chemical environments in azupyrene. It is also possible that the differing environments relates to the tertiary or secondary carbons with 3 or 2 carbons bonded to other carbons, respectively. Alternatively, this could also represent the environments of carbons within the azupyrene/pyrene molecule and those on the edge, bonded to hydrogens.

newline

Molecular azupyrene was the only 2 peak NIXSW analysis included in this report was because of its 2 distinct carbon environments present in its C 1s spectrum, seen in spectrum

a) and b) of **Figure 4.10**, the results of which are denoted in **table 4.3**. This analysis showed low adsorption heights of 2.08 Å and 2.33 Å, as predicted by the low binding energies of the peaks and the high asymmetries in XPS, and a concentrated spread of heights with a coherent fraction of 0.79 and 0.74 respectively. This high coherent fraction is expected for a room temperature deposition of a molecule, as only the lone molecule exists on the surface. This would have the implication that the two peaks represent two different chemical environments within azupyrene structure, reinforcing the aforementioned distortion in planarity of the non-alternant azupyrene as a result of the stronger binding of the 5-7 structure.

In the 1 peak pyrene NIXSW analysis, seen in spectrum a) of **Figure 4.11** and tabulated in **table 4.4**, only 1 peak could be accurately distinguished in the XSW analysis due to the small height of the secondary peak. Despite this, it is likely that a 2 peak analysis wouldn't reveal a significant difference in coherent fraction or position indicated by the already fairly high coherent fraction. The determined adsorption height was much higher than that of azupyrene at 3.11 Å. This would reinforce the weaker binding predicted from the alternant molecular pyrene XPS, indicated by its higher binding energy and lower asymmetry than azupyrene.

4.3.2 Dendritic

The dendritic preparation of azupyrene can be seen in spectra b) of **Figure 4.8**, with its fitting parameters denoted in **table 4.1**. This preparation was carried out at 50 K lower in temperature than that measured in **Figure 4.6**, thus one would expect less ideal graphene regions, and a greater amount of dendritic phase in this preparation. The XP spectra was fitted with a broad primary peak centred at a low binding energy of 284.15 eV of width 0.85 eV with no asymmetry, and substantially smaller secondary peak at a lower binding energy of 283.32 eV. The broadness of the peaks at 0.85 eV, suggest their composition to be of numerous carbon environments ranging from possible unreacted molecular azupyrene, partially reacted dendritic azupyrene and oligomers, to likely small quantities of ideal graphene. This assuming our growth model is correct and that it encompasses the entire process which is wholly unlikely. Other examples of possible reaction intermediates include; sigma bonded molecules with the surface, or adatoms. The prominence of these may lead to different trends in binding energy and asymmetry to what our hypothesised mechanism would expect. Fitting this peak with more subpeaks to determine the chemical environment of each of the components of individual species proved to be difficult and unsuccessful, but it is safe to assume a large spread of environments in the dendritic form. Fitting with only 2 peaks may have had the effect that the individual asymmetries of the component environments were absorbed into the broad peak width. Alternatively, lack of asymmetry of either peaks could indicate that the molecular azupyrene, that binds strongly with the surface to produce asymmetry, is not stable at these crystal temperatures. Assuming that the remaining structures on the surface

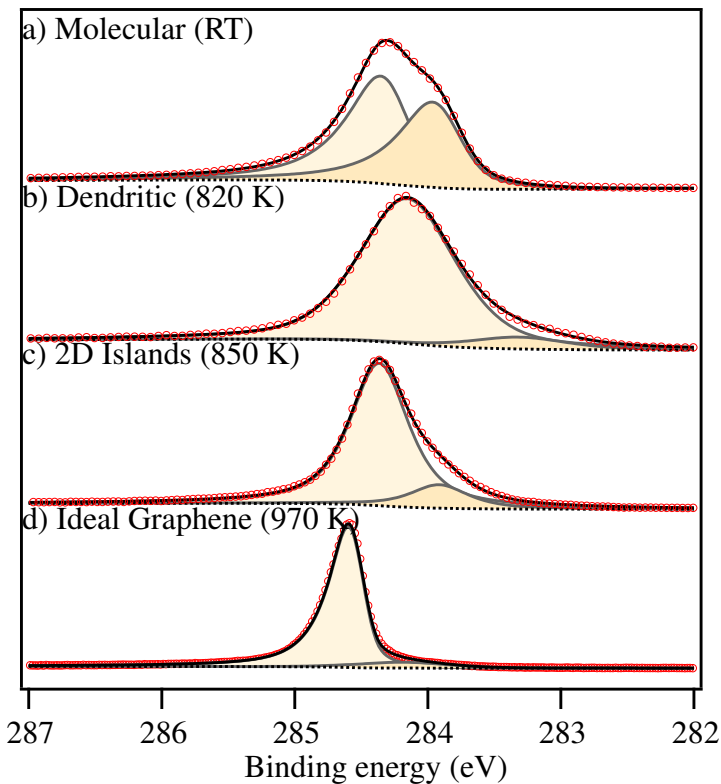


Figure 4.8: Comparison of soft XPS C 1s peaks and their sub-peaks for different temperature preparations at different stages of growth of graphene from azupyrene.

are primarily the dendritic form of azupyrene, the dendritic network may disrupt the aromatic π system that interacts with the metal surface in molecular azupyrene, resulting in a loss of peak asymmetry. This may be the source of the secondary peak in the 2D islands XP spectrum in **Figure 4.8**, spectra c).

A 1 peak NIXSW analysis of a dendritic preparation of azupyrene can be seen in spectrum c) of **Figure 4.10**, the results of which are denoted in **table 4.3**. The slightly higher adsorption height is indicative of reaction of azupyrene to form reaction intermediates as the average height has moved away from the molecular form and closer to that of graphene and 2D islands. The low coherent fraction of 0.30 describes a larger spread in adsorption heights, which would be expected for a surface that contains oligomers and dendritic structure, all with varying structures that have varying interaction with the metal surface. This would conform with the dendritic regions with variable height and electronic structure seen in **Figure 4.6**, the STM image of a 2D island preparation of azupyrene. As the adsorption height is still fairly low compared to that of the higher temperature preparations, it is quite likely that molecular azupyrene exists on this surface; contributing to the low mean adsorption height.

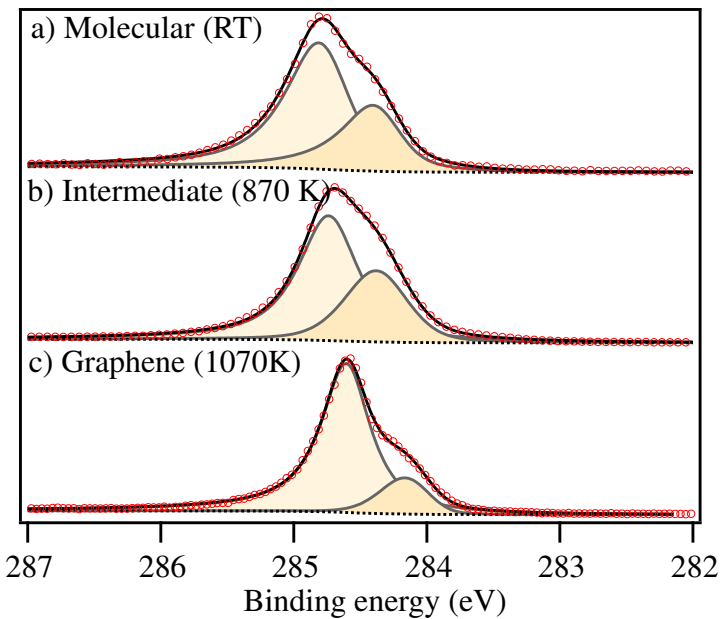


Figure 4.9: Comparison of soft XPS C 1s peaks and their sub-peaks for different temperature preparations at different stages of growth of graphene from pyrene.

4.3.3 2D Islands/Intermediate

The spectra for the 2D islands preparation for azupyrene is shown in spectra c) of **Figure 4.8** with specific fitting parameters denoted in **table 4.1**. The peaks in the azupyrene spectra have increased in binding energy from their dendritic preparation, spectra b) of **Figure 4.1**, now located at 284.36 eV, and 283.91 eV, suggesting a trend toward the higher binding energy of graphene with the azupyrene. The temperature of this preparation would be comparable to that seen in the STM image in **Figure 4.6**, and so one could associate this binding energy change to the increase in graphene-like property of the centres of the islands and closest to the terraces, seen in inset a). The azupyrene peaks themselves have both narrowed with widths of 0.53 eV, suggesting a reduction in concentration of reaction intermediates and increase in consistent graphene-like form.

Meanwhile, the XP spectra of the intermediate temperature preparation for pyrene is shown in spectra b) of **Figure 4.9** with specific fitting parameters denoted in **table 4.2**. Relative to the molecular pyrene preparation, minimal change in binding energy has occurred with a slight decrease (<0.1 eV) in binding energy, as well as a slight narrowing of the primary peak from the molecular form from 0.61 and 0.55 eV, meanwhile the secondary peak remained the same width. This lack of chemical environment change may simply be a consequence of the similarity in structure to graphene, and so the graphene growth process of pyrene may not induce as visible changes in chemical environment, as seen through XPS, relative to that of azupyrene.

Whilst it is unlikely, this may simply mean that the required temperature for graphene syn-

Growth Stage	Crystal Temperature (K)	Peak	Binding Energy (eV)	Relative Intensity	FWHM (eV)	Asymmetry
Molecular	300	1	284.35	0.56	0.63	0.22
		2	283.96	0.44	0.63	0.22
Dendritic	820	1	284.15	0.92	0.85	0.00
		2	283.32	0.08	0.85	0.00
2D Islands	850	1	284.36	0.86	0.53	0.00
		2	283.91	0.14	0.53	0.00
Ideal	970	1	284.60	0.91	0.36	0.20
		2	284.20	0.09	0.80	0.00

Table 4.1: Table of fitted azupyrene XPS peak parameters. The respective spectra and peaks can be found in **Figure 4.8**

Growth Stage	Crystal Temperature (K)	Peak	Binding Energy (eV)	Relative Intensity	FWHM (eV)	Asymmetry
Molecular	300	1	284.81	0.67	0.61	0.14
		2	284.40	0.33	0.55	0.20
Intermediate	870	1	284.74	0.67	0.55	0.05
		2	284.38	0.33	0.56	0.03
Ideal	870	1	284.60	0.85	0.46	0.06
		2	284.16	0.15	0.45	0.10

Table 4.2: Table of fitted pyrene XPS peak parameters. The respective spectra and peaks can be found in **Figure 4.9**

thesis using pyrene is higher than that of azupyrene, and the activation energy for the intermediate phase to start forming graphene has not been reached.

The largest change in peak parameters between the intermediate and molecular pyrene prep is the loss in asymmetry of the two peaks, suggesting some change in structure leading to a weaker interaction with the the surface; perhaps oligomerisation or formation of the aforementioned trimers that could interact weakly with the surface. These structure would have to have a weaker interaction with the surface to produce this result. Alternatively, this may be a result of not fitting all the individual chemical environments in the fairly broad peaks, possibly resulting in the larger peaks absorbing the asymmetry into their intensity. This lack of asymmetry is also true for azupyrene at this temperature range despite clearly reacting, the previous explanations could also hold true for the azupyrene XP spectra. As both molecules have the same lacking asymmetry, it may relate to both molecules intermediate phases having a disrupted π system that does not interact as strongly with the metal surface.

A key difference between the different the intermediate preparation of the different molecules, is the trend in secondary peak height from low to high temperature preparations such as that of the intermediate and 2D islands preparations. The decrease in secondary azupyrene

peak is indicative of a development in the growth process, with less dendritic phase existing. Meanwhile the continued prominence of the secondary peak for pyrene may indicate that the growth process occurs at higher temperatures for pyrene, and/or that part of the secondary peak in the pyrene is not part of a dendritic phase, but the trimers, seen in STM image in **Figure 4.7**, that appear to survive up to high temperatures.

A 1 peak NIXSW analysis of a 2D islands preparation of azupyrene can be seen in spectrum d) of **Figure 4.10**, the results of which are denoted in **table 4.3**. An increase in mean adsorption height of 0.55 \AA , to 3.04 \AA is measured for this preparation; nearing that of ideal graphene, seen in spectrum e). This suggests a development in the growth process, potentially formation of some quantities of ideal graphene, as seen in the centre of the islands of the STM image in **Figure 4.6**, which would contribute to a higher mean height. The remaining presence of dendritic azupyrene and other reaction intermediates would also be expected to contribute to the slightly reduced adsorption height from ideal. A low coherent fraction of 0.30 would agree with this prediction, indicating the broadening of the range of phases of azupyrene, now including graphene, dendritic, and possibly even molecular, though this phase was not visible in the STM.

In the 1 peak pyrene NIXSW analysis, seen in spectrum b) of **Figure 4.11** and tabulated in **table 4.4**. The results of this NIXSW did not reveal any substantial changes in the coherent fraction, increasing by 0.03 from the molecular preparation, and remaining at 0.51; neither has it had much effect on mean adsorption height, increasing by 0.03 \AA , to 3.14 \AA . This lack of substantial change would suggest that either minimal reaction has occurred with the pyrene on the surface, or that the reaction intermediates of the growth process of pyrene on copper(111) maintain a similar adsorption height. Reaction intermediates could be expected to simply be larger oligomers of pyrene, or potentially islands of graphene. This would not be easily differentiable the graphene form. These results agree with those of the XPS which indicated similar peak properties between molecular intermediate phase. In general, it is not clear at what stage the pyrene is changing, and whether it is changing rapidly at all due to the nature of XPS and NIXSW techniques.

4.3.4 Ideal Graphene/Graphene

The XP spectrum for the ideal graphene from azupyrene is shown in spectra d) of **Figure 4.8**, with specific fitting parameters denoted in **table 4.1**. This preparation of azupyrene has a significantly narrow primary peak of 0.36 eV , indicating a high purity of graphene resulting

Growth Stage	Coherent Fraction (F_h)	Coherent Position (P_h)	Adsorption Height (Å)
Molecular Peak 1	0.79 ± 0.06	0.12 ± 0.03	2.34 ± 0.06
Molecular Peak 2	0.75 ± 0.07	0.00 ± 0.03	2.09 ± 0.06
Dendritic	0.40 ± 0.05	0.19 ± 0.04	2.48 ± 0.08
2D Islands	0.30 ± 0.04	0.46 ± 0.03	3.05 ± 0.06
Ideal graphene	0.75 ± 0.03	0.56 ± 0.01	3.26 ± 0.02

Table 4.3: Table of azupyrene XSW Results for different growth stages.

Growth Stage	Coherent Fraction (F_h)	Coherent Position (P_h)	Adsorption Height (Å)
Molecular	0.48 ± 0.05	0.49 ± 0.04	3.11 ± 0.08
Intermediate	0.51 ± 0.02	0.51 ± 0.01	3.15 ± 0.02
Dendritic	0.58 ± 0.03	0.50 ± 0.01	3.13 ± 0.02

Table 4.4: Table of Pyrene XSW Results for different growth stages.

from its high concentration of identical chemical environments, hence the labelling of this preparation as ideal graphene. Furthermore, the relative intensity of the primary peak compared to the secondary, 0.91:0.09 respectively, indicates the low concentrations of alternative environments and growth phases such as dendritic, and other oligomer structures. The secondary peak is substantially more broad at 0.8 eV width, is likely accounting for the small concentrations of various phases remaining on the surface, or alternatively, the edge carbons and those at the terraces of the copper. Furthermore, the primary peak has a high asymmetry, indicating that there is a strong interaction between the ideal graphene and the copper surface. The lack of asymmetry in the 2D islands phase would suggest there is a difference between this interaction depending on the quality of graphene. Conversely, the higher binding energy of this primary peak at 284.60 eV would suggest that the interaction between the surface has gotten weaker.

Meanwhile the spectra for the graphene preparation for pyrene is shown in spectra c) of **Figure 4.9**, with specific fitting parameters denoted in **table 4.2**. The primary peak of pyrene has the same binding energy of 284.60 eV, suggesting that this represents the graphene in both samples. Despite this similarity, the properties of the spectra of these samples have some clear differences. For example, the secondary peak of pyrene is much more dominant with a ratio of 0.85:0.15 between the primary and secondary peak, suggesting a more prominent alternative phase(s). Moreover, the primary peak is more broad, at 0.46 eV, than that of ideal graphene from azupyrene, indicating a lower purity. The secondary peak is similarly wide to the primary, indicating that it is representing a single, or at least a small range of pyrene environments, perhaps the trimer seen in the STM image in **Figure 4.7** contributes significantly to this. The asymmetry of the primary graphene peak is still fairly low in comparison to that of

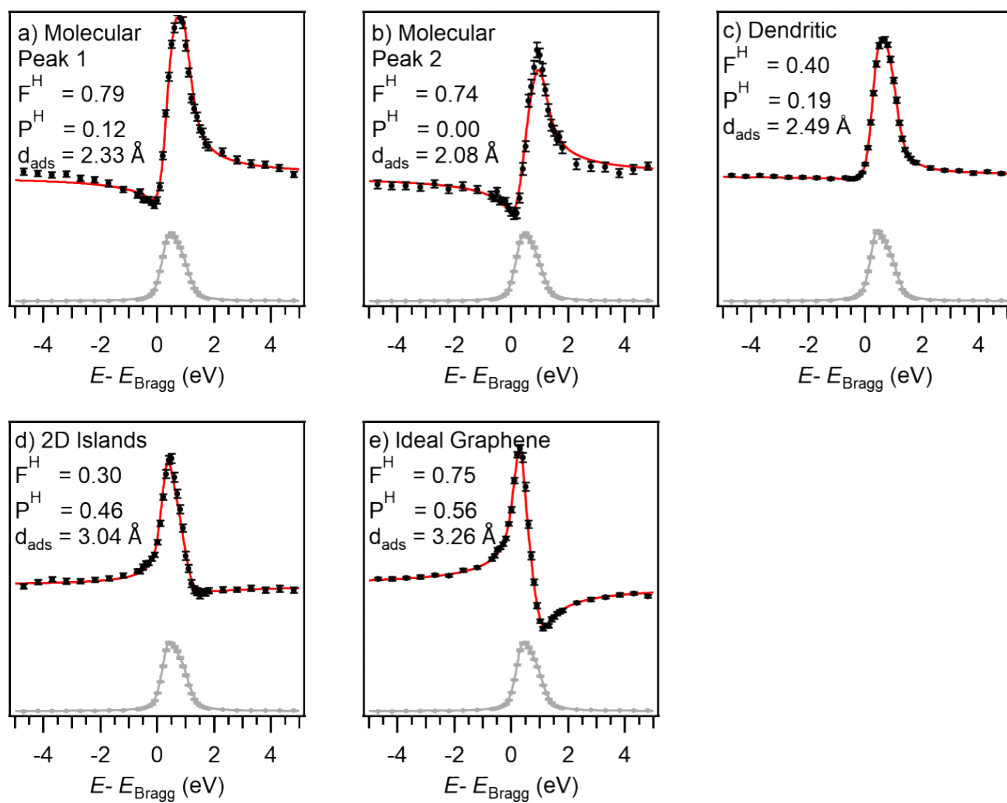


Figure 4.10: NIXSW of different stages of growth of graphene from Azupyrene. a) Molecular sample peak 1(Room Temperature). b) Molecular sample peak 2(Room Temperature). c) Dendritic sample (820 K). d) 2D Island (870 K). e) Ideal graphene (973 K).

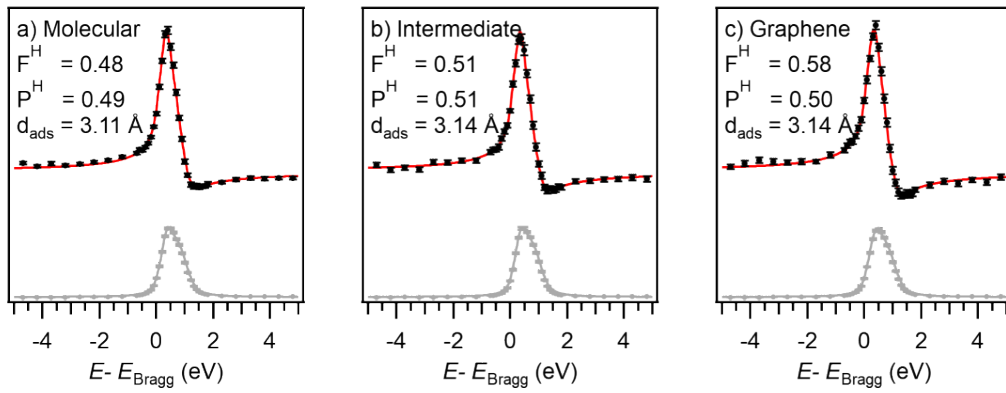


Figure 4.11: NIXSW of different stages of growth of graphene from Azupyrene. a) Molecular sample (Room Temperature). b) Dendritic sample (820 K). c) 2D Island (870 K).

azupyrene; whilst the secondary peak has a higher asymmetry, possibly suggesting a weaker interaction with the surface for pyrene graphene than azupyrene graphene. Simultaneously, the alternative pyrene environments in pyrene, may interact more strongly with the surface, producing this asymmetry.

From this data, a question arises as to whether higher or lower quality graphene is bound more strongly to the surface. According to the previously mentioned studies, non-alternant defects/impurities would lead to stronger interaction with the surface [6, 94, 95]. This would imply that the higher asymmetry for azupyrene graphene compared to that of pyrene would mean azupyrene graphene is not more pure, but in fact contains more defects, in particular, 5-7 defects from the azupyrene reagent. This would disagree with the implication narrowness of the peak; that the environment is more concentrated and defined, thus is more pure.

Regardless of comparison with the azupyrene, both peaks of this pyrene preparation are narrower than before and have higher binding energy than the intermediate preparation. The secondary peak has decreased in intensity substantially from the lower temperature.

A greater perspective for this argument is provided by the NIXSW of the two graphene preparations of the molecules. A 1 peak NIXSW analysis of the ideal graphene from azupyrene can be seen in spectrum e) of **Figure 4.10**, the results of which are denoted in **table 4.3**. A significant improvement takes place as a result of this temperature step. Firstly, the adsorption height increased further to 3.26 Å, which clearly indicates further production of graphene, as alternative product with such an adsorption height that could contribute to the higher height is not known. More significant is the substantial increase in coherent fraction to 0.75, indi-

cating a much higher concentration of ideal graphene, and lower concentration of dendritic and intermediate phase graphene.

Conversely, in the 1 peak pyrene NIXSW analysis, seen in spectrum c) of **Figure 4.11** and tabulated in **table 4.4**. The mean adsorption height of the high temperature preparation of pyrene is practically identical to that of the intermediate phase. The only change comes in the improvement in coherent fraction by 0.07 to 0.58, indicating a slight decrease in spread of heights, despite them being centred around 3.14 Å. Through more extensive study of azupyrene graphene, the expected adsorption height of graphene on copper(111) is believed to be 3.24 Å; implying either a lack of purity in the resulting pyrene graphene, or an alternative product with a lower adsorption height, that is preventing a higher coherent fraction from being achieved. A combination of the both may be the most likely option considering that the XPS study of pyrene graphene, seen in spectra c) of **Figure 4.9**, has shown a slightly more broad primary carbon environment at the same binding energy of azupyrene graphene, seen in spectra d) of **Figure 4.8**, but also containing a notable but narrow secondary peak at a lower binding energy which could possibly account for the trimers seen in the pyrene STM image in **Figure 4.7**.

Due to limitations in the experimental systems used for synthesis, the temperature of the copper crystal could not be controlled reliably and consistently above those shown in this paper, and so producing preparations with pyrene at higher temperatures was not done. It may well be possible that at higher temperatures, pyrene produces graphene with a coherent fraction similar to that of azupyrene, with a coherent position similar to that as well. The mechanism by which this occurs is not entirely clear, potentially involving incorporation of the stable oligomers into the body of the graphene network, or desorption from the crystal, for example, of the aforementioned pyrene trimers. Alternatively, there may be some other feature that needs to optimised for better quality growth of graphene by pyrene. What can be concluded from this research is the growth of graphene at comparable temperatures between pyrene and azupyrene, produces a less defined graphene environment, with a secondary feature that is indicative of another which may be trimers remaining on the surface.

4.3.5 Conclusions

Studying the growth of azupyrene using XPS, NIXSW, and STM indicated the existence of 4 growth stages, at increasing crystal temperatures: Molecular(~ 300 K), Dendritic (~ 820 K), 2D Islands (~ 870 K), and ideal graphene (~ 970 K). The existence of graphene confirmed through measurement of characteristic graphene arc in LEED[5], and characteristic moire pattern seen in STM[92]; with the quality of graphene indicated by the narrow width of its

XPS environment in the C 1s spectrum, and a high coherent fraction seen in NIXSW. Study of pyrene growth showed evidence of graphene through LEED and STM at similar crystal temperatures (870 – 1070 K), although XPS and NIXSW revealed a broader range of carbon environments at similar temperature preparations. Study of pyrene and pyrene produced graphene was more difficult due to the similarity of the natural pyrene environment with that of graphene. Where in azupyrene, there are clear changes in adsorption height during the growth process, determined by NIXSW, varying from a predicted mean adsorption height as low as 2.08 Å, to 3.26 Å, the predicted adsorption height remained consistent, varying between 3.11 Å and 3.14 Å. This would suggest some change in the electronic structure of the azupyrene during growth, a larger number of reaction intermediates. Furthermore, the coherent fraction of azupyrene fluctuated substantially between 0.30 and 0.79 for different growth stages, whereas pyrene only varied between 0.48 and 0.58 from molecular to graphene product; further supporting the substantial change in azupyrene physical and electronic structure compared to that of pyrene. In terms of possible reaction intermediates for pyrene, one would expect larger chain oligomers of hexagonal pyrene. The growth process likely does not involve breaking of pyrenes hexagonal subunit, or its aromaticity, as this would have been indicated by a more substantial change in XP peak binding energies, and variance in mean adsorption height measured through NIXSW, for different crystal temperature preparations.

Whilst there were some indications of purity of environments from XPS and NIXSW analysis of azupyrene and pyrene preparations, the defect concentrations of azupyrene and pyrene graphene could not be definitively stated from this research. Further study, potentially incorporating AFM or low temperature STM, of defect types and concentration for various quality preparations could indicate whether the 5-7 defects exist within these samples, and optimise for desired concentrations of these defects through control of preparation temperature, with target of potential sites for single atom catalysts. This study would also be useful to understand the growth mechanism of pyrene and azupyrene in more detail. Looking forward, research attempting depositing metal and other heteroatoms upon these sites would be a clear next step for development as a SAC substrate. In conclusion, this study served to provide a fundamental understanding of the results of graphene synthesis using alternant and non-alternant molecules through epitaxial growth of copper(111), revealing some quality differences, and clear differing pathways of growth for azupyrene and pyrene.

Chapter 5

Energy-scanned Photoelectron Diffraction analysis of Molybdenum Disulfide on Au(111)

5.1 Introduction

One type of 2D material that has come into the fore in recent years, particularly since discovery of graphene, are transition metal dichalcogenides (TMDCs). TMDCs have chemical formula MX_2 , where M is a transition metal, and X are chalcogens; and are structurally arranged as a layer of transition metal, sandwiched between two layers of chalcogen atoms. Choice of chalcogen is frequently sulfur, selenium or tellurium; whilst choice of transition metal is commonly molybdenum, tungsten, tantalum etc. In contrast to the most prominent 2-D material, graphene, TMDCs uniquely have strong spin-orbit coupling, favourable electronic and mechanical properties, including a direct bandgap in monolayer form. These electronic properties are similar to that of the most common Si/GaAs materials used in current semiconductor technology, but on the nanoscale; with modern Si semiconductors being as small as 7 nm, there still lies potential for further reduction of this size, for greater space efficiency of chips. Application of atomic thickness components, produced using 2-D material based semiconductors could be the next stage for the transistor and general electronics industry[96]. Furthermore, these properties give rise to numerous applications including flexible electronics, optical electronics, energy storage and harvesting. A key stage in development of these products is improving understanding of the physical structures that underpin a materials properties. This study involves the use of energy-scanned photoelectron diffraction (PhD) to attempt to identify the structure of MoS_2 on Au(111) [97, 98].

5.1.1 Molybdenum Disulfide

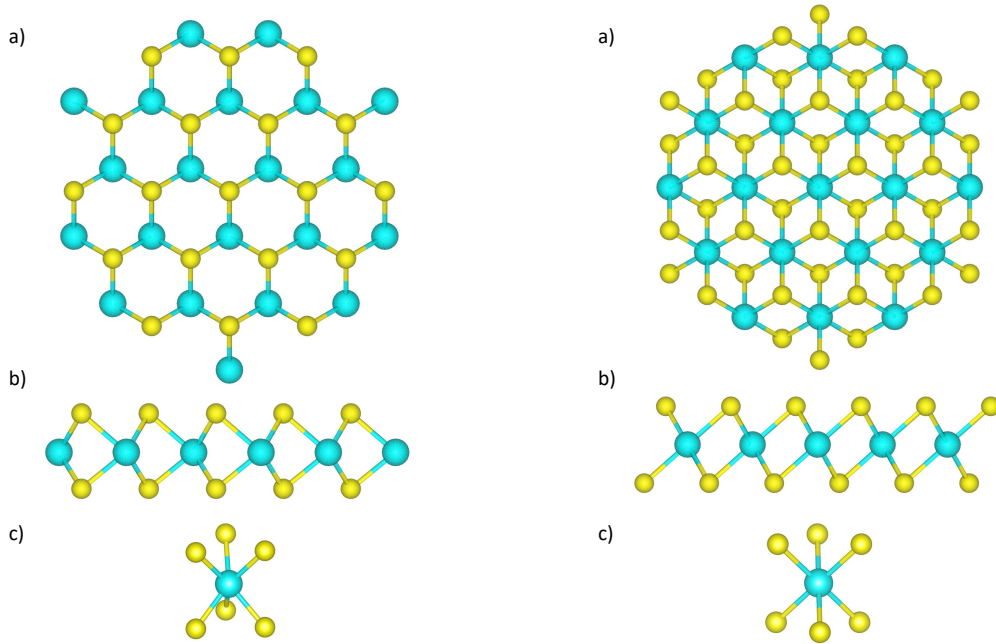
The most popular combination of TMDC in recent times has been molybdenum disulphide(MoS_2) due to its high on/off current ratio (10^8) useful for field effect transistors, a sizeable charge carrier mobility of $200\text{cm}^2(\text{Vs})^{-1}$, and variable band gap for the 1H configuration; shifting from a direct band gap of 1.88 eV to an indirect band gap of 1.29 eV when increasing the number of layers from monolayer to bulk, respectively [18]. This tunability of the band gap holds true for variation in other properties of its nanostructure, giving potential for flexibility through a range of uses from biosensors [99] to nanoscale electronics [20, 100, 101, 102]. The components of MoS_2 are also particularly common and safe to work with compared to other options of chalcogen(e.g. selenium, tellurium) [97]. MoS_2 has found varying use photovoltaic devices, and rechargeable batteries, and in solid-state lubricants thanks to its weak interlayer interactions [103, 104, 105]. Additionally, MoS_2 has been investigated for possible applications in energy storage and conversion, use in the hydrogen conversion reaction (HER), as an electrode material for lithium and sodium batteries to name a few [18].

5.1.2 Polyptism of Molybdenum Disulphide

MoS_2 can be synthesised through varying methods; leading to creation of different allotropes and morphologies (e.g. 2D nanosheets, 1D nanowires, and 0D nanoplatelets)[19]. Despite these varied overall macrostructures, the majority of studies have shown that (cite the studies) bulk MoS_2 has 3 primary structural configurations: 1T, 2H, and 3R; where the number refers to the number of layers in the bulk unit cell, and the letter refers to the type of structure where T - Trigonal, H - Hexagonal, and R - Rhombohedral [106]. Each of these structures have been found to exhibit different electronic properties as a result of their structural differences, meanwhile heterostructures have also been found to form [107]. This study involves analysis of monolayer and sub-monolayer preparations of MoS_2 thus the configurations differ only by monolayer unit cell, for which the 3R and 2H are identical. Thus, this study primarily considers the possibilities of the 1T and 1H conformers of MoS_2 .

1H MoS_2

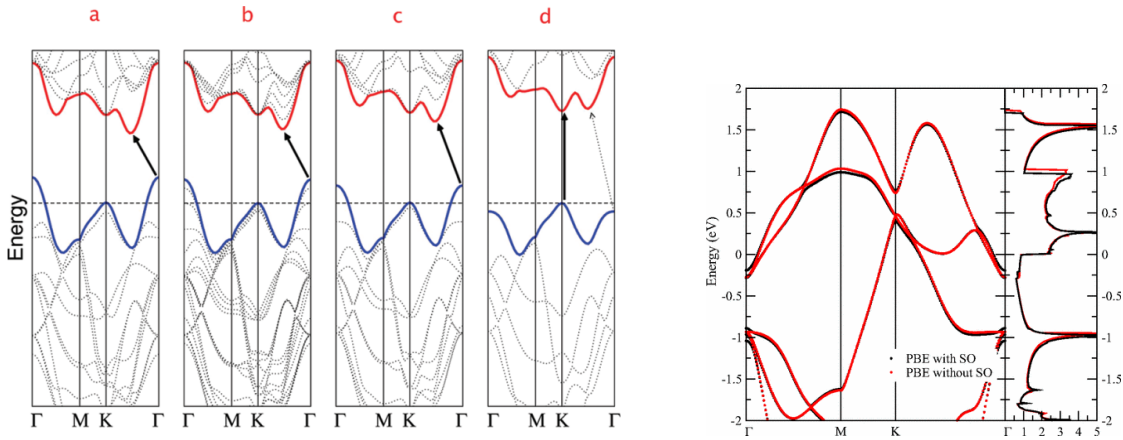
This structure is by far the most common form of MoS_2 , exhibiting a hexagonal structure with literature lattice parameters (citation) $a = 3.15 \text{ \AA}$, $c = 12.30 \text{ \AA}$, seen in **Figure 5.1a**. The 1H structure is composed of a triangular prismatic configuration of Mo and its 6 co-ordinated S atoms, with D_{6h} symmetry, and $P6_3/mmc$ space group and behaves as an n-type semiconductor. It is the most thermodynamically stable of the conformers, being stable until 1203°C before forming Mo_2S_3 . Common synthesis techniques include CVD, PVD, and ball milling. Interestingly, its band gap can be altered when heated at high pressures such that its electronic properties go from being semiconductor-like to metallic. Electronically, it has



(a) a) Vertical, b) side view of $1H - MoS_2$ structure, c) trigonal prismatic coordination of $1H$ configuration. In this structure, the Mo atom has trigonal prismatic coordination with the S atoms, with the upper S atoms situated directly above the lower S atoms.

(b) a) Vertical, b) side view of $1T - MoS_2$ structure, c) trigonal prismatic coordination of $1H$ configuration. In this structure, the Mo atoms has octahedral coordartion with the S atoms, with the upper S atoms offset to the lower S atoms, almost as if rotated in plane by 60 degrees relative to the opposite layer.

Figure 5.1: Diagrams of 1H and 1T configurations of MoS_2 .



(a) $1\text{H} - \text{MoS}_2$ bandgap diagram showing trend in changes of band gap depending on numbers of monolayers. a) is bulk $1\text{H} - \text{MoS}_2$, b) is quadrilayer, c) is bilayer, and d) is monolayer [108]. (b) $\text{S}1\text{T} - \text{MoS}_2$ band gap diagram depicting overlap between upper and lower bands at Fermi level [109].

Figure 5.2: Bandgap diagrams for 1H and 1T configurations of MoS_2

a finite band gap that varies from indirect to direct as the number of monolayers within the structure decreases to a single monolayer, between the filled d_{z^2} and the empty $d_{x^2} - d_{y^2}$ and d_{xy} bands; this is depicted in **Figure 5.2a** [18, 108].

1T MoS_2

This is the tetragonal structure of MoS_2 with octahedral coordination, seen in **Figure 5.1b** and is the second most common configuration found. Typical monolayer growth methods such as mechanical exfoliation produce a low proportion of this conformer relative to the 1H form[107]. One method involves oxidation of regular $1\text{H} - \text{MoS}_2$, progressing through 3 polymorphs as it does so: $a \times 2a$, $2a \times 2a$, then finally, $\sqrt{3}a \times \sqrt{3}a$. This suggests a distinct variability in the physical, thus electronic properties, with potential for tuning with adjusted growth parameter. $1\text{T} - \text{MoS}_2$ has tetragonal structure with lattice parameters $a = 5.60 \text{ \AA}$, and $c = 5.99 \text{ \AA}$ [18, 110], and vastly differing electronic properties from the 2H configuration owing to its Fermi level lying within its d_{xy} , d_{yz} , d_{xz} giving it its metallic nature, with overlapping conduction and valence bands at Fermi level, as seen in **Figure 5.2b**. This conformer has its own range of potential uses including: electrochemical reactions, photoelectrocatalysis, photodetectors, and energy storage devices [111].

5.1.3 Synthesis of MoS_2

MoS_2 layers only undergo van der Waals bonding between one another, thus mechanical exfoliation, similar to that used in Graphene, is commonly used to synthesise flake samples of monolayer MoS_2 [82]. Alternatively, liquid phase exfoliation, hydrothermal/solvothermal methods, and commonly CVD are often also utilised for synthesis [106]. In this study growth

was carried out using molecular beam epitaxy (MBE). As for the previously mentioned study of azupyrene graphene, this is because of its reproducibility as a technique, that allows accurate control over experimental conditions facilitating consistent production of sub-monolayer samples. Where sub-monolayer refers to incomplete surface coverage by the molecule, typically between 20 - 80%.

5.1.4 Epitaxial Growth of MoS_2 on Au(111)

This study of MoS_2 growth on an Au(111) surface was carried out with the purpose of characterising the Moire superstructure resulting from the substrate-overlayer relationship between the two as described by C. Silva [1]. Whilst both Au(111) and MoS_2 share a hexagonal structure, the difference in lattice constants of 2.884 Å for Au(111) and 3.18 Å for MoS_2 1H [112, 113] leads to a lattice mismatch between the two structures that produces a variation in registry between the bottom S atoms of the MoS_2 , and Au(111) surface seen as a corrugation in the surface [114], similar to that seen in graphene on Cu(111) [92]. Previous studies of this type of growth have investigated the electronic structure of the material using ARPES, strongly suggesting, through the inferred band structure, that it produces the 1H conformer of MoS_2 [115, 116]. Choice of gold as substrate metal was done with the aim of understanding the properties of MoS_2 on gold, a commonly used contact material for electronics.

5.2 Methods

5.2.1 Experimental Details

Preparation and analysis was carried out at the I09 Beamline at Diamond Light Source, UK ($P = 2 \times 10^{-10}$ mbar), at which XPS, XSW, LEED and PhD were used to study the samples. The experimental data used in this chapter was acquired before my involvement in the research at Diamond Light Source, in parallel to a previous study at I09[1]. Similarly, the initial data processing to acquire the experimental modulations was completed by *David A. Duncan*.

Preparations were carried out on Au(111) single crystals cleaned using 1.5 keV sputtering, annealed to 873 K, and verified using LEED. MoS_2 was prepared using following method: in a preparation chamber, Mo was evaporated with a rate of $\approx 0.05 \text{ \AA min}^{-1}$ for 5 min using an e-beam evaporator (SPECS EBE4 (OAR EGN4)) with the sample at room temperature. Simultaneously, the sample was exposed to H_2S via a LOSE doser with a stainless steel capillary tube of 12 mm diameter ending 20 mm in front of the sample, resulting in a background pressure of 5×10^{-6} mbar. After the evaporation is stopped, the sample was annealed for

30 min at 853 K (843 K) while the exposure to H_2S is continued. The exposure then was stopped directly (5 min) after the heating [1].

The PhD spectra were acquired for the S 1s spectra using a photon energy range of 2522 - 2822 eV whilst the Mo 2p spectra were taken with a photon energy range of 2570-2870 eV. Fitting of the individual EDCs was carried out using a numerical convolution of a Gaussian and Lorentzian peak.

The software used to carry out the scattering calculations were those written and developed by numerous collaborators, including *D. P. Woodruff*, *V. Fritzsche*, and the PSO scripts were written by *Dr. David A. Duncan*. During attempts to identify structural models for PhD modulations, 2 primary methods were used: Particle swarm optimisation, as described in **Section 3.4.6**, and grid searches. Use of the particle swarm optimisation was identified as the most efficient model optimisation technique for PhD compared to other optimisation techniques[45], as described in **section 3.4.6**, and so was used for optimisation of model structures in this analysis. Grid searches were used understand the the relationship between various structural parameters with R-factor, although the results of these are only depicted for the 1H hexamer structure as the results of those for the trimer and 1T hexamer were lost before the writing of this report. Because of the large computational cost of grid searches, they were only used for simpler models with low numbers of scattering events. The results of these grid searches were displayed using various line and colourmap plots for 1D and 2D datasets using MatLab scripts developed by *D. A. Duncan*, which were adjusted and debugged for use in this study. Identified minima were visualised as molecules using VESTA, and their PhD modulation along with the experimental modulation was plotted using a Python script. The aforementioned scripts can be provided upon request. All of the PhD scattering calculations, optimisations, grid searches were ran on the SCARF computer cluster hosted by the Science Technology and Facilities Council (STFC).

The experimental modulations taken during this study were chosen to have as high amplitude and signal-to-noise ratio as possible. Consequently, particularly for sulfur modulations, off-normal crystallographic directions and higher polar angle modulations were measured as its nearest neighbour scatterer would be expected to be the molybdenum atom, which is 30° off-normal emission according to literature values for MoS_2 structure [102]. Similarly for molybdenum modulations, the dominant 180° backscatterer atoms behind Mo would be expected to be the lower S atoms within literature models of the structure [102, 117], thus measurements were also taken at the same off-normal crystallographic directions, though with slightly smaller polar angles.

5.3 Results & Discussion

5.3.1 Previous Study

As mentioned in the previous section, these measurements were taken in parallel to those described in another study by *Silva et al*, investigating the Moire superstructure of MoS_2 on Au(111)[1]. The results of which can be summarised as determination of the samples as a 1H configuration of monolayer MoS_2 with a Moire superstructure seen as corrugation in the material. This study provided the basis for the models used in the PhD analysis.

5.3.2 Computational Aspects

During the process of attempting structural determination of these MoS_2 samples using PhD, various bugs were identified in the underlying PhD scattering calculation code, that of the PSO, and the scripts involved in reading the data. Briefly, these include:

- Discovery of a memory error that produced a large unrealistic intensity for the first photoelectron energy data point in the scattering calculation specifically for simulating 2D materials. This led to unrealistic R-factors and was corrected by *David A. Duncan*.
- Bug identified limiting the shape of the potential file arrays. This required editing of the gold potential file used in the relevant calculations.
- CPU affinity error during parallel processing using multiple nodes on the SCARF cluster. This prevented two calculations from sharing the same nodes on the cluster, thus limiting the maximum number of simultaneous calculations being run.
- General adjustments had to be made to the scripts involved in reading the results of grid searches.
- A script was written in python to interpret the results of the PhD single calculations. This is available upon request.

5.3.3 Qualitative Analysis

Experimental modulations for the samples of sulfur (S 1s) and molybdenum (Mo 2p) are displayed in **Figure 5.3 & 5.4**, respectively, with columns of modulations labelled by their crystallographic direction $\langle \#\#\# \rangle$, and the polar emission angle with respect to normal emission

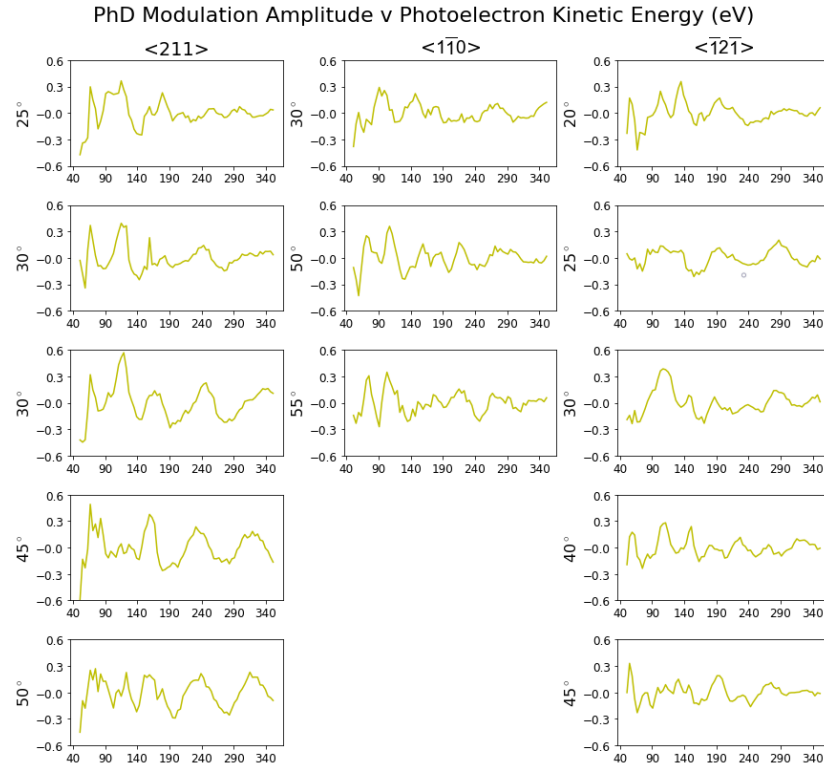


Figure 5.3: Pure PhD modulations for S 1s emission. Polar angle is denoted along the y axis of each modulation, whilst the azimuthal angle/crystallographic direction is denoted atop the columns of the plots.

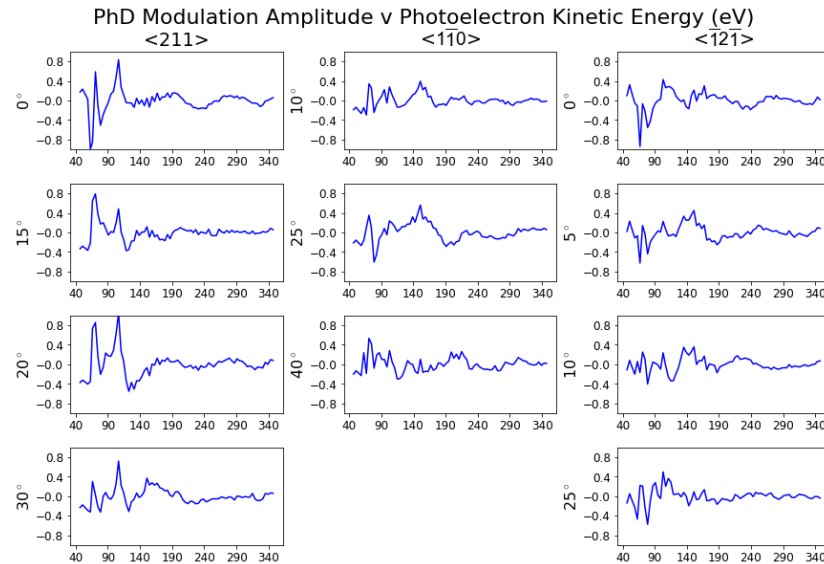


Figure 5.4: Pure PhD modulations for Mo 2p emission. Polar angle is denoted along the y axis of each modulation, whilst the azimuthal angle/crystallographic direction is denoted atop the columns of the plots.

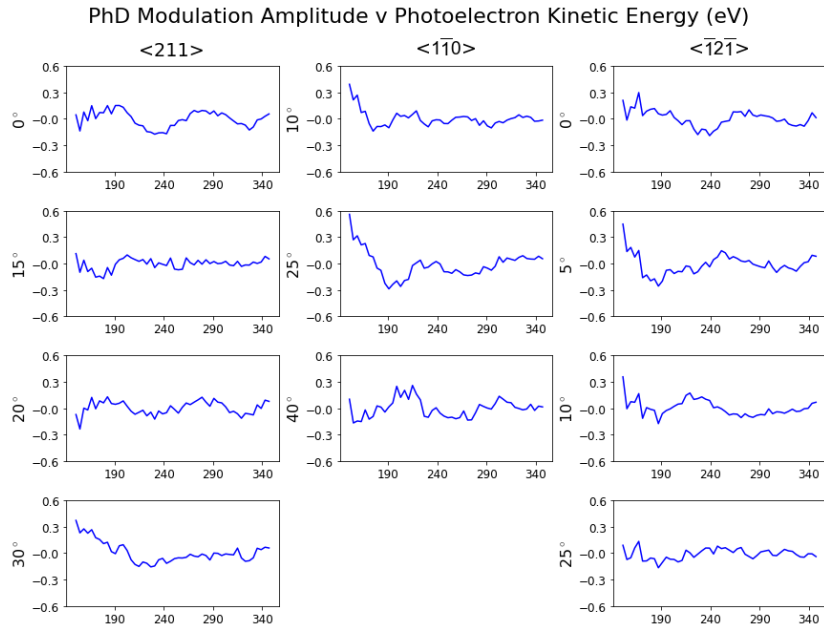


Figure 5.5: Pure PhD modulations for Mo 2p emission with 40 - 150 eV removed. Polar angle is denoted along the y axis of each modulation, whilst the azimuthal angle/crystallographic direction is denoted atop the columns of the plots.

labelled on the left hand side of each modulation. Qualitative analysis of the modulations themselves can convey some qualitative information of structure. As described in **Section 3.4.2**, the amplitude and period of a PhD modulation can be indicative of the geometry and sometimes symmetry of the site at which an emitter exists.

Looking first at the molybdenum modulations, it is clear that there is an additional contribution to the first ~ 150 eV of the modulations, with large changes in amplitude of over 1 over small changes in photoelectron kinetic energy. These large fluctuations are non-periodic as would be expected for a diffractive contribution, both factors indicating a possibility of contribution of an XPS feature, such as a transient Auger peak. The presence of these Auger peaks was noted in the labbook whilst measurements were being taken. Consequently, the initial region of 40 - 150 eV was removed from experimental molybdenum modulations. This updated modulation can be seen in **Figure 5.5**.

Looking next at sulfur modulations, they do not appear to be completely periodic throughout as well. The amplitude of these modulations are more reasonable than was seen with sulfur, consequently, one would expect this to be a result of greater dynamical disorder, and possible existence of multiple emission sites. Removing this region of data for sulfur modulations was therefore not done. These effects could account for the perceived shorter period modulations for sulfur compared to molybdenum. Generally, there is a larger amplitude for sulfur modulations compared to molybdenum modulations, this may be the result of the

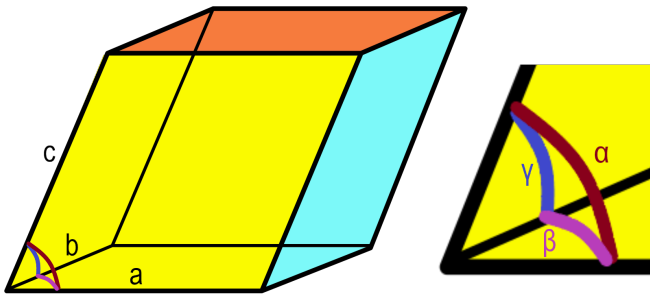


Figure 5.6: Example rhombohedral unit cell with side lengths a , b , and c , with angles α , β , and γ between them. This type of unit cell was used to define the full structure models for MoS_2 1H and 1T, as well as the gold substrate.

scattering cross section of Mo being much higher than that of sulfur, resulting in a larger modulation for the sulfur modulations involving the Mo backscatterer[118].

5.3.4 Particle swarm optimisation parameters

When carrying out structure optimisations, numerous structural parameters were optimised alongside some fundamental parameters that are universal for all calculations. One of these is the inner potential. This refers to the energy barrier that electrons at the Fermi edge have to overcome to be emitted, this is variable in an experimental system and so it must be optimised for to acquire the correct modulation shape. Furthermore, a Debye-Waller factor is used to model the atomic vibrations of the atoms within the structure, this takes the input of the mean squared vibrational amplitude for each atomic species, which is also included in the optimisation.

5.3.5 Full Structure with Au(111) Substrate

Building upon the results of the previous study [1], a pure, 1H configuration MoS_2 sample could be expected. Furthermore, in literature, 1H and 1T are described as the most common configurations of MoS_2 , and so models of these two structures seemed most reasonable[102, 117, 119, 120, 121].

The models for 1T and 1H were based upon literature descriptions of the structure, using a rhombohedral unit cell, of lattice parameters a , b , and c for side lengths, and α , β , and γ for the angles between them. An example rhombohedral unit cell can be seen in **Figure 5.6**. To allow for variance of the structure, there was freedom around the literature values for these parameters; for 1H, $a = b = 3.24 \text{ \AA}$ [119], and $c = 3.18 \text{ \AA}$ [120] for 1T, $a = b = 3.18 \text{ \AA}$ [121], alongside the height of each layer, cartesian position of Mo atom, with the general parameters stated in the previous sections. Note, angles α , and γ were restricted at 90 degrees.

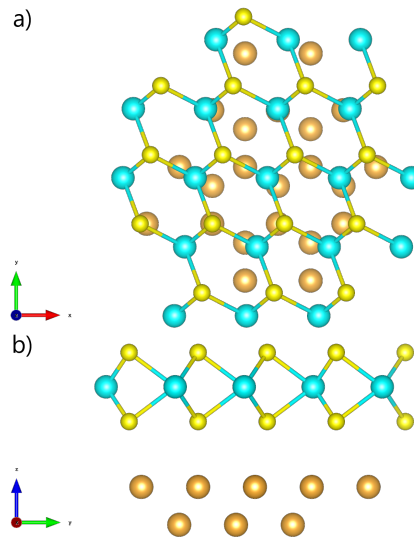


Figure 5.7: PSO optimised structure of 1H full structure on Au(111) substrate from different perspectives: a) Vertical, b) Side

$R =$	0.82	Literature Values[119, 120, 121]	
	Model	1H	1T
a (\AA)	3.45	3.24[119]	3.18[121]
b (\AA)	3.33	3.24[119]	3.18[121]
c (\AA)	3.22	3.18[119]	N/A
β ($^\circ$)	81	60 [117]	60 [117]

Table 5.1: Table of model parameters from optimisation of PhD modulations of full structure 1H on Au(111) compared to literature values from various sources. No literature parameters are of MoS_2 on gold(111) substrate.

The result of PSO of these structures was a low correlation. To provide an example, the results for the 1H model are displayed. The optimised modulations for the 1H structure can be seen in **Figure 5.8**, whilst the optimised structure can be seen in **Figure 5.7**, with tabulated results of lattice parameters listed in **table 5.1**. It is clear from visual analysis of the modulations that there is limited correlation between theoretical and experimental data. This is confirmed by the high R-factor of 0.82, indicating minimal correlation of the model with the data. For the remaining models, the modulations will only be listed in the appendices.

The source of this lack of correlation despite the structure could have been a number of issues with the model. One of these may relate to not modelling the corrugation of the MoS_2 with the Au(111) surface. For this to be computed, a method of modelling the corrugation would need to be developed, as well as a much larger supercell to include all possible sites

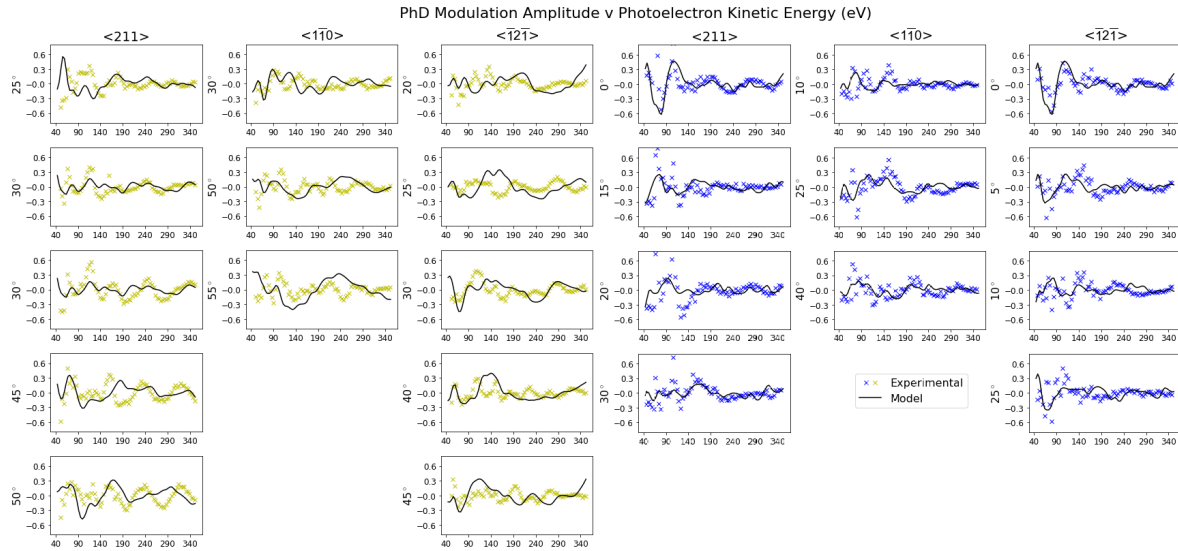


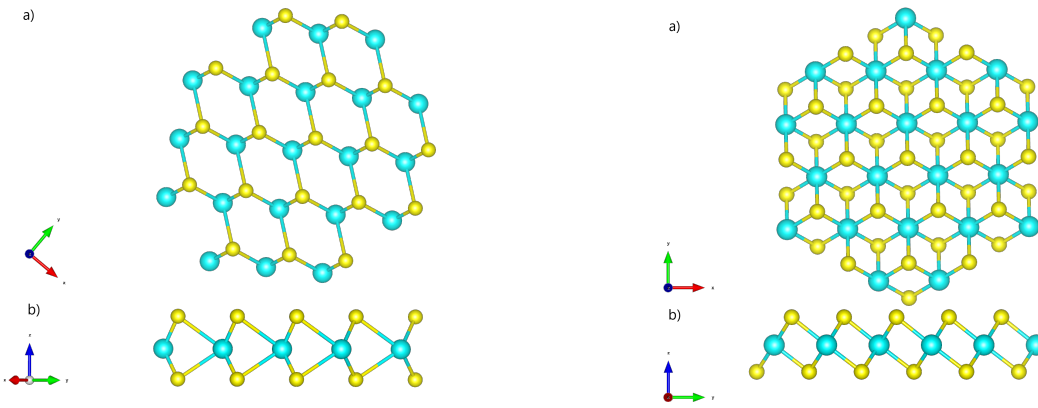
Figure 5.8: PhD modulations of PSO optimised structure of 1H full structure on Au(111) substrate overlayed onto experimental modulations of S (yellow) and Mo (blue) at varying polar angle (y label) and crystallographic direction (x label).

of MoS_2 on the Au(111) surface. The scattering calculations to do so would be substantially more computationally expensive to simulate and optimise. Consequently, modelling this varied registry was not attempted.

An alternative approach to avoid the inclusion of this registry was to bypass the gold entirely. To do so, one would have to consider the dependence of the PhD simulation on the gold surface. In the case of sulfur modulations, S 1s modulation would primarily be dominated by the 180° backscattering from nearest neighbours. Whilst this would primarily be dependent on alignment of upper S atoms with Mo atoms, one would expect a notable contribution from scattering of lower S emission by the gold substrate. For the molybdenum, however, this 180 degree backscatterer is the lower S atoms, with the gold substrate being several Angstrom below. These assumptions would suggest that the PhD modulations of from S 1s emission would require inclusion of gold within the model. Mo modulations would be less likely to be impacted by removing gold from the model. Consequently, the following models excluded the gold substrate from the model and consequently use the molybdenum modulations in their calculations.

5.3.6 1T and 1H Full structure without Au(111) substrates

Subsequent models optimised using Mo modulations only, with the gold substrate removed were attempted. The resulting optimised modulations are listed in **Appendix A.1 & A.2** for 1H and 1T, respectively. The optimised structures are shown in **Figure 5.9a & 5.9b**, with the resulting structural parameters tabulated in **table 5.2 & 5.3**.



(a) PSO optimised structure of 1H full structure from different perspectives: a) Vertical, b) Side.

(b) PSO optimised structure of 1T full structure from different perspectives: a) Vertical, b) Side.

Figure 5.9: Optimised full structures of 1T and 1H configurations of MoS_2

R =	0.75	Literature Values[119, 120, 121]	
	Model	1H	1T
a (\AA)	3.19	3.24[119]	3.18[121]
b (\AA)	3.19	3.24[119]	3.18[121]
c (\AA)	3.44	3.18[119]	N/A
β ($^\circ$)	83	60 [117]	60 [117]

Table 5.2: Table of model parameters from optimisation of PhD modulations of full structure 1H compared to literature values from various sources. No literature parameters are of MoS_2 on gold(111) substrate.

Compared to the Gold model, there was an improvement in correlation for the 1H and 1T models, conveyed by the lower R-factors of 0.75 for 1H and 0.77 for 1T. For both models, the resulting R-factor was still particularly large, indicative of an incomplete model, disagreeing with the results of the previous study [1]. Furthermore, the optimised structures produced are different from the literature structures, particularly for 1H[102, 117]. The 1T structure is closer to what is expected by literature[121] though the weak correlation invalidates this.

As this large structure model did not produce clear correlation, and a more complex method of varying registry was not available, the decision was made to build the model from the base up. This involved designing a simple model to imitate the full structures, but isolating the fundamental scattering events that underpin the PhD modulation. The resulting modulations from these calculations can still fit data very well as, the skeleton of a PhD modulation is dominated by the nearest neighbour scattering events, as described in Section

R =	0.77	Literature Values[119, 120, 121]	
	Model	1H	1T
a (\AA)	3.43	3.24[119]	3.18[121]
b (\AA)	3.43	3.24[119]	3.18[121]
c (\AA)	3.19	3.18[119]	N/A
$\alpha(^{\circ})$	90	90 [117]	90 [117]
$\beta(^{\circ})$	72	60 [117]	60 [117]
$\gamma(^{\circ})$	90	90 [117]	90 [117]

Table 5.3: Table of model parameters from optimisation of PhD modulations of full structure 1T compared to literature values from various sources. No literature parameters are of MoS_2 on gold(111) substrate.

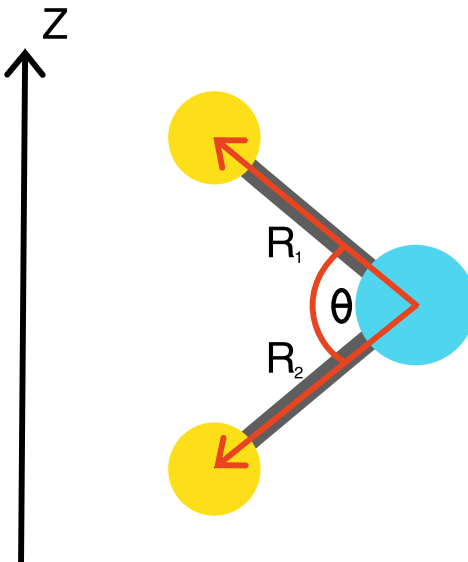


Figure 5.10: Diagram of trimer model, along with key parameters of the model: Upper sulfur bond length, R_1 , lower sulfur bond length, R_2 , and bond angle, θ .

3.4.2.

5.3.7 Simple Model - Trimer

The trimer model was developed as the simplest model to imitate any MoS_2 structure, involving less than 10 scattering events of Mo-S and Mo-S-S interactions. The trimer structure was based around the central Mo atom, and 1 of the upper and lower S atoms coordinated to it, as the other 4 S atoms are equivalent through symmetry. The model itself was built upon a spherical coordinate system centred around the origin of the Mo atom, and 2 S atoms restricted to upper and lower hemispheres, with complete freedom in angle and bond length within reasonable limits. This model is depicted in **Figure 5.10**.

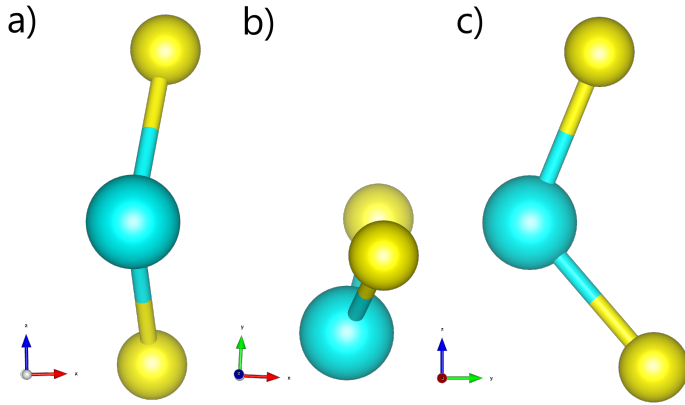


Figure 5.11: PSO optimised structure of trimer model from different perspectives a) Rear, b) Vertical, c) Side

$R =$	0.62	Literature Values[102]
	Model	1H
Upper Bond Length (\AA)	2.27	2.42[102]
Lower Bond Length (\AA)	2.23	2.42[102]
Bond Angle ($^\circ$)	115	120[102]

Table 5.4: Table of model parameters from optimisation of PhD modulations of trimers compared to literature values from various sources. No literature parameters are of MoS_2 on gold(111) substrate.

The trimer model produced a substantial reduction in R-factor from the full structures, modelling the backbone of the experimental modulations more accurately, as seen in **Appendix A.3**, with resulting structure parameters tabulated in **table 5.4**, and depicted in **Figure 5.11**. Accompanying the improved correlation were bond lengths nearer that of literature for both 1T and 1H structures[102].

Some inferences could be made from the resulting structure, particularly the staggered nature of the two S atoms. In the 1H configuration, one would expect vertical stacking of the two S atoms, aligned with the z axis, however, this is clearly not the case, indicating that either the structure is not 1H as predicted in the previous study [1], or that the structure is not flat. This would support the idea of the corrugated Moire superstructure with a variable registry[1]. Despite this notable improvement in correlation, the simplicity of the trimer structure cannot reveal the full identity of the MoS_2 structure configuration, only confirming the rough shape and bond lengths of the base unit of the MoS_2 structure. To do so a more complex model would be required, involving more atoms, and modelling the Mo-Mo scattering events.

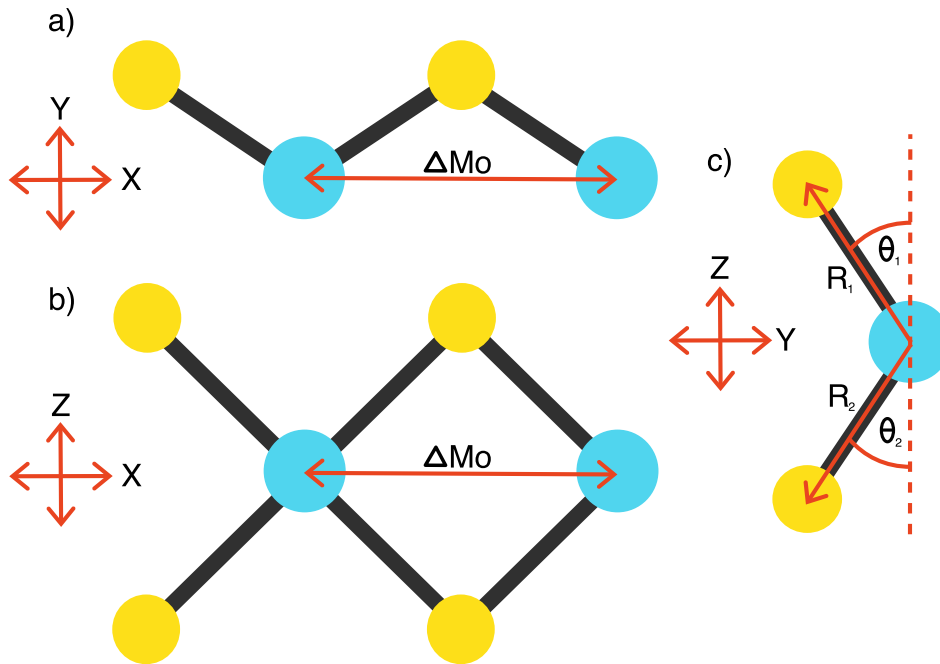


Figure 5.12: Diagram of hexamer 1H model, with perspectives from the a) Z axis (Vertical), b) Y axis (Side), and c) X axis (End), denoting key parameters of the model.

5.3.8 Hexamers

The solution to a slightly more complex model was a 6 atom hexamer structure composed of 2 Mo atoms and 4 S atoms in, a mirrored trimer configuration, the model originates from a small section of the 1T and 1H full structures containing two adjacent trimers, outlined in **Appendix A.6 & A.7**. The purpose of this model was to introduce more complex scattering events with between neighbouring trimers, in particular, it reintroduces the Mo-Mo scattering event, which would be expected to have a substantial impact due to the strong scattering cross section of Mo[118]. Models of the structures can be seen in **Figure 5.12** for 1H, and **Figure 5.17** for 1T.

1H configuration

The structure of the 1H hexamer model is shown in **Figure 5.12**. The PSO optimised structure is shown in **Figure 5.13**, with resulting parameters tabulated in **table 5.5**. The raw modulations can be found in **Appendix A.4**. There is a clear further improvement in R-Factor with a new lowest value of 0.51, showing best correlation so far with the experimental modulations. Comparing model parameters to literature, bond lengths are much closer to literature than that of the trimer model, however, the bond angle acquired is significantly larger than expected at 176° compared to the expected 120° , furthermore, the Mo - Mo separation, which one would

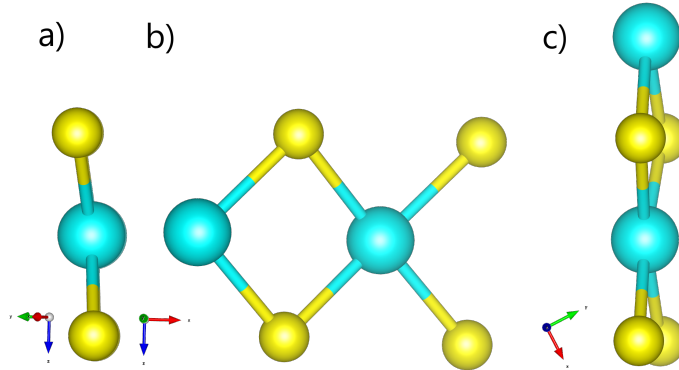


Figure 5.13: PSO optimised structure of 1H hexamer structure from different perspectives:
a) End, b) Side, c) Vertical.

$R =$	0.51	Literature Values[102]
	Model	1H
Upper Bond Length (\AA)	2.38	2.42[102]
Lower Bond Length (\AA)	2.35	2.42[102]
Bond Angle ($^\circ$)	176	120[102]
Mo - Mo Separation (\AA)	3.34	3.18[102]

Table 5.5: Table of model parameters from optimisation of PhD modulations of 1H hexamer compared to literature values from various sources. No literature parameters are of MoS_2 on gold(111) substrate.

expect to be analog with the unit cell length, is larger than expected at 3.34\AA compared to 3.18\AA . This pairing of lower R-Factor with unrealistic structural parameters is indicative of the model not representing the motifs present in the true system; essentially that the model is too simplistic. Subsequently, an equivalent hexamer was developed to model the 1T structure, with results outlined in the next section.

Calculating the PhD modulations for the hexamer structures was quick as a result of their low number of scattering interactions. Thus the use of grid searches are not so computationally expensive, therefore feasible for the structure. The first of these being the relationship between upper and lower S angles with R-factor, depicted in a 2D colourmap in **Figure 5.14**. This image shows a clear minimum at angles for upper and lower S atoms of 96° , and 280° , respectively, thus a bond angle of 174° . This is far larger than the literature value of 120° , suggesting a large inaccuracy within the model. Similarly to **Figure 5.15**, there is a much more prominent dependence on the lower S angle, over the upper S angle, reminding us of the greater dominance of backscatterer positioning on resulting modulation. This grid search could have benefitted from calculations involving sulfur data, which, despite likely resulting in higher R-factors, might have probed the position of the upper S atoms to a greater

extent due to the sulfur modulation having a large dependence on Mo backscatterer with upper S geometry. Plots of dependence of individual upper S and lower S angle passing through the minimum of the 2D colourmap can be found in **Appendix A.11 & A.10**, respectively.

The second of these grid searches measured the relationship being between upper and lower S radius with R-factor, depicted in a 2D colourmap in **Figure 5.15**. This image shows a minima for radius of upper and lower S atoms of 1.66 \AA and 1.70 \AA , respectively, which correspond to bond lengths of 2.38 \AA and 2.35 \AA . These are smaller than measured and predicted by literature value of 2.43 \AA for both 1T and 1H configurations[102]. The resulting minimum in this grid search therefore lies away from literature values., once more indicating an incomplete model. Similarly to the previous image, this image also conveys a greater dominance of the lower S radius on R-factor compared to that of the upper S. Again, highlighting the dominance of the 180° backscattering on the resulting PhD modulation, as the lower S atom is closer to this geometry than the upper S. Additionally, inclusion of sulfur data within these calculations could have increased the dependence on upper S position, and predicted it more accurately, to give more realistic bond lengths for Upper S atoms. Plots of dependence of individual upper S and lower S radius passing through the minimum of the 2D colourmap can be found in **Appendix A.9 & A.8**, respectively.

The final relevant grid search completed for this structure was a 1D scan of Mo-Mo separation with respect to R-factor, seen in **Figure 5.16**. This revealed a simple relationship between the Mo - Mo separation and R-Factor, with a strong dependence on the parameter that is unsurprising considering the large scattering cross section of Mo [118]. There exists a distinct minima in Mo - Mo separation of 3.30 \AA which is similar to that identified by the PSO, of 3.34 \AA .

1T Configuration

The structure of the 1T hexamer is shown in **Figure 5.17**. This structure was optimised using PSO, producing the resulting structure seen in **Figure 5.18**, with parameters tabulated in **table 5.6**. The PhD modulations of this structure can be found in **Appendix A.5**. Similar to the 1H hexamer model, there is also a substantial improvement in R-Factor, though slightly higher than that of 1H at 0.56. Intriguingly, the optimised structural parameters for the 1T structure are much closer to those of literature than 1H. The upper and lower S bond lengths of 2.47 \AA and 2.49 \AA are close to the literature value of 2.42 \AA [102], and the bond angle of 145° which is much closer than that of 1H, although still far from the literature value of 120° . Finally, the Mo - Mo separation of 3.17 \AA is matching that of literature of 3.18 \AA . This

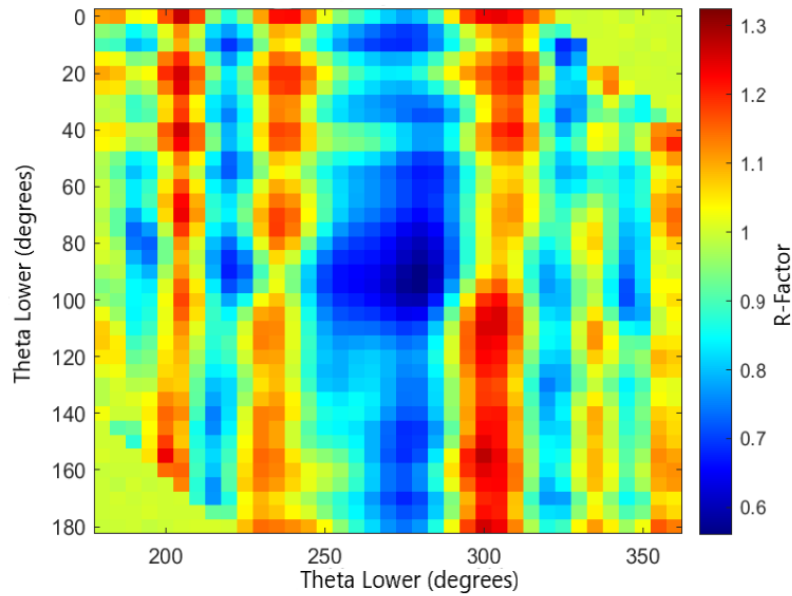


Figure 5.14: 2D colour map of R-factors for angles of upper and lower S atoms for the 1H hexamer model, where theta of the upper S atom is θ_1 , and for the lower S atom, θ_2 , in the 1H hexamer model diagram of **Figure 5.12**. 2D slices at the minimum R-factor of the two angles can be found in the Appendix. The other parameters for this model were that of the PSO optimised values including: a Mo-Mo separation of 3.34 Å, and bond lengths of 1.70 Å and 1.66 Å for lower and upper sulfurs, respectively

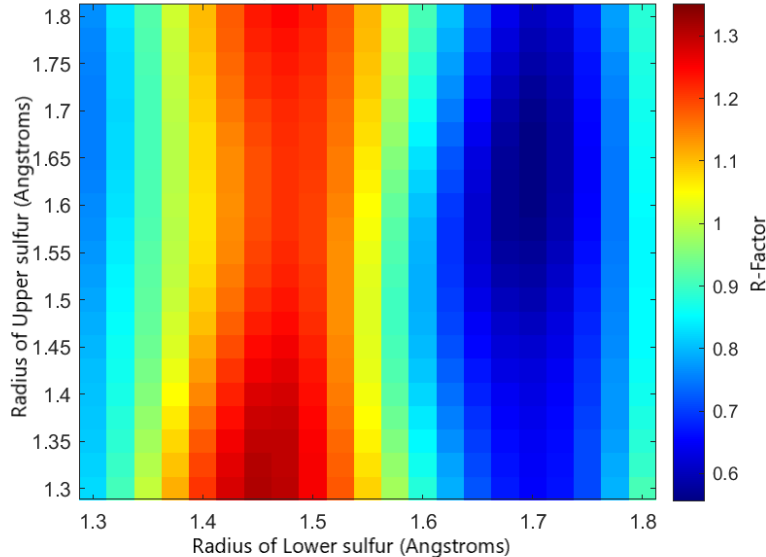


Figure 5.15: 2D colour map of R-factors for radii of upper and lower S atoms for the 1H hexamer model, where the radii for the upper S is R_1 , and the lower S R_2 in the hexamer model diagram of **Figure 5.12**. 2D slices at the minimum R-factor of the two radii can be found in the Appendix. The other parameters for this model were that of the PSO optimised values including: a Mo - Mo separation of 3.34 Å, and a bond angle of 174°.

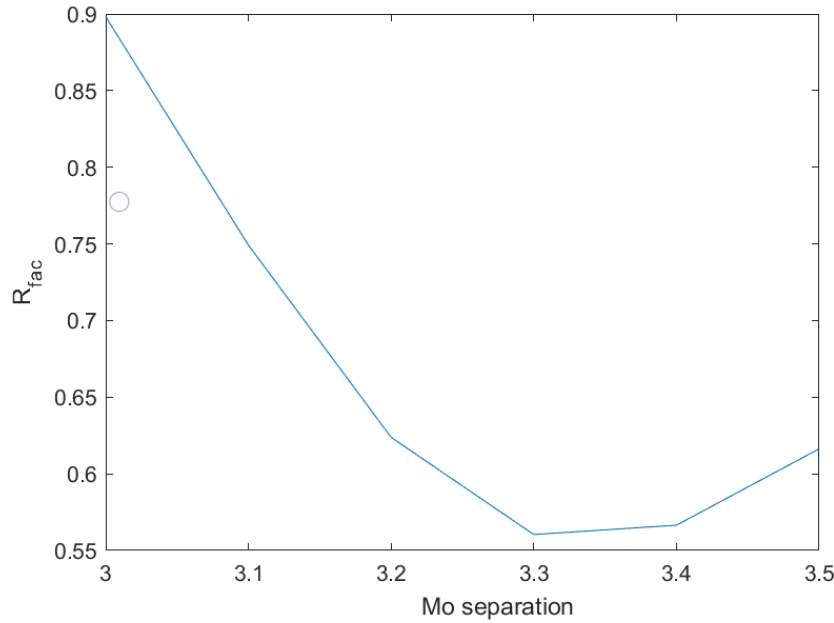


Figure 5.16: Plot of R-Factor with respect to Mo - Mo separation for the 1H hexamer model, where Mo-Mo separation is ΔMo in the hexamer model diagram of **Figure 5.12**. The other parameters for this model were a bond angle of 174° , and bond lengths of 1.70 \AA and 1.66 \AA for lower and upper sulfurs, respectively

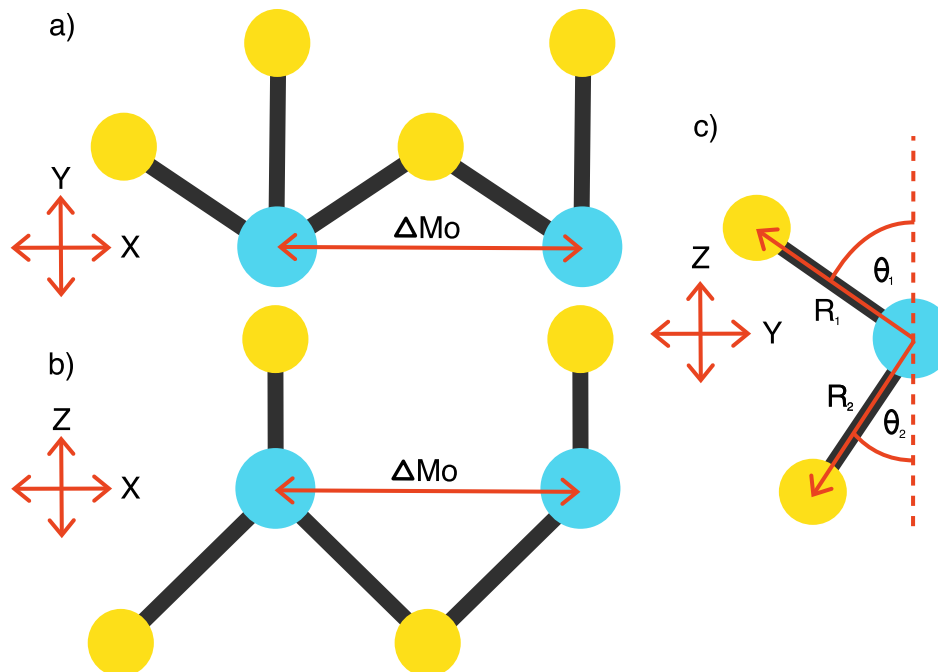


Figure 5.17: Diagram of hexamer 1T model, with perspectives from the a) Z axis (Vertical), b) Y axis (Side), and c) X axis (End), denoting key parameters of the model.

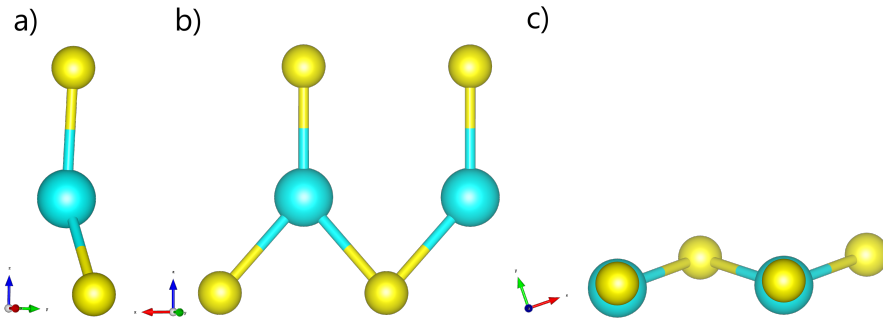


Figure 5.18: PSO optimised structure of 1T hexamer structure from different perspectives: a) End, b) Side, c) Vertical.

$R =$	0.56	Literature Values[102]
	Model	1H
Upper Bond Length (\AA)	2.47	2.42[102]
Lower Bond Length (\AA)	2.49	2.42[102]
Bond Angle ($^\circ$)	145	120[102]
Mo - Mo Separation (\AA)	3.17	3.18[102]

Table 5.6: Table of model parameters from optimisation of PhD modulations of 1T hexamer compared to literature values from various sources. No literature parameters are of MoS_2 on gold(111) substrate.

better match of structural parameters with literature is promising when paired with the near-equivalently low R-factor of the 1T.

Despite the better match of 1T, the R-factors of both hexamer models are much larger than one would desire for a good model of an experimental structure, particularly if the inherent structure of the experimental system was matching one of the two. This is likely a result of insufficient modelling of the experimental system, suggesting the system is not of 1H or 1T individually, but feasibly a heterostructure including those two alongwith other intermediate or meta stable configurations that could exist between them[107, 122]

5.3.9 Conclusions

The results of this PhD structural determination of MoS_2 on Au(111) were not able to identify the configuration of the structure, due to insufficient correlation, with a lowest achieved R-Factor of 0.51 for the 1H Hexamer structure. However, this study highlighted the lack of a key aspect from the aforementioned models, preventing the strong correlation with exper-

imental PhD modulations. The next steps would be to identify the missing features of these models, of which there are several possibilities outlined below.

Whilst unlikely due to the weak scattering cross section of Gold [118] and several Angstrom separation between Mo and Au surface, it is possible that that the model was limited by the exclusion of gold, despite only considering molybdenum modulations. It is also worth considering that solving the structure using only molybdenum modulations may not have been entirely reliable due to their weak dependence on the upper S layer, as highlighted in the 1H hexamer grid searches. Re[inclusion of sulfur modulations into these calculations may be able to compensate for this, due to their dependence on S positioning, in general. This would require inclusion of the Au(111) surface within the model. In either case, the missing feature in the models attempted in this study be the lack of modelling the variable registry of the Moire structure predicted in the previous study of these MoS_2 samples[1]. To do so, one could predict various common corrugation structures, for example, a sinusoidal oscillation in height, varying equally in both x and y, with amplitude defined by a small number of parameters. Another possible method of modelling this variable registry would be to carry out an incoherent average of the calculated modulation over several different heights using the same feature in the PhD software that is used to averaging over the symmetries of a system.

As mentioned previously, the 1H and 1T configurations of MoS_2 are those most commonly found in literature. It is, however, possible that a MoS_2 sample is made up a heterostructure of various different configurations of MoS_2 , as has been seen before between the 1T and 1H structures before [107]. There also exists several configurations of MoS_2 , including metastable states theorised using DFT calculations[122]. What may be more likely is that the structure is a combination of the various configurations structures, not only across the entire surface, but perhaps even distributed across the various sites within the supercell of MoS_2 on Au(111) depending on the strength of interaction with the surface at the sites. Modelling these structures could be done using the incoherent averaging function over the modulations produced by the different structures. These may also require a dominance factor to control the quantity and contribution of each of different structural configurations to the .

Described in this chapter were one of the first attempts of modelling a 2D material using PhD, only being preceded by a study of an h-BN sheet on rhodium(111) [123] which, aside from the substantial differences between the two materials, is also inherently a different type of 2D material; being 1 atom thick as opposed to the 3 atoms composing an MoS_2 sheet. Generally, PhD has been used to solve molecules adsorbed on surfaces. Consequently, understanding around solving these structures is minimal, and some valuable information for successful modelling of the structure are not available, as with molecular studies using the

technique. This study has provided a greater understanding of the limitations of the PhD optimisation software, but also the provided insight into potential improvements and features that could be added to the software in future, to allow easier modelling of 2D materials, for example, mechanisms to model corrugation in structure, or different orientations of sheets. If the technique were developed further, use of PhD to study 2D materials could be extremely valuable to the study of 2D materials, thanks to its ability to determine internal structural parameters of surfaces, to a high degree of accuracy, whilst bypassing convolutions of structure seen when studying the structures of materials using other popular surface techniques, such as STM.

General next steps in the study of this data would be to explore more exotic possibilities for the model. The relatively high R-factors even for the best models produced, suggest a major difference in structure, perhaps relating to orientation, registry, or even configuration. Furthermore, a broader optimisation of the structure may help identify this, with fewer structural restrictions as it appears that the current structures and constraints do not match the reality of the system. In future, solving this structure could prove to be a promising novel use of PhD for structural determination of a 2D system, expanding possibilities of it as a valuable technique for study of 2D materials, with the ability to probe the underlying structure of often materials. Furthermore, to identify the composition of these MoS_2 samples may reveal a valuable insight into the true structure of the material. If the aforementioned theories of a complex heterostructure is found to be true, then this would provide a previously unseen perspective on this modern material.

Appendix A

PhD Chapter Supporting Information

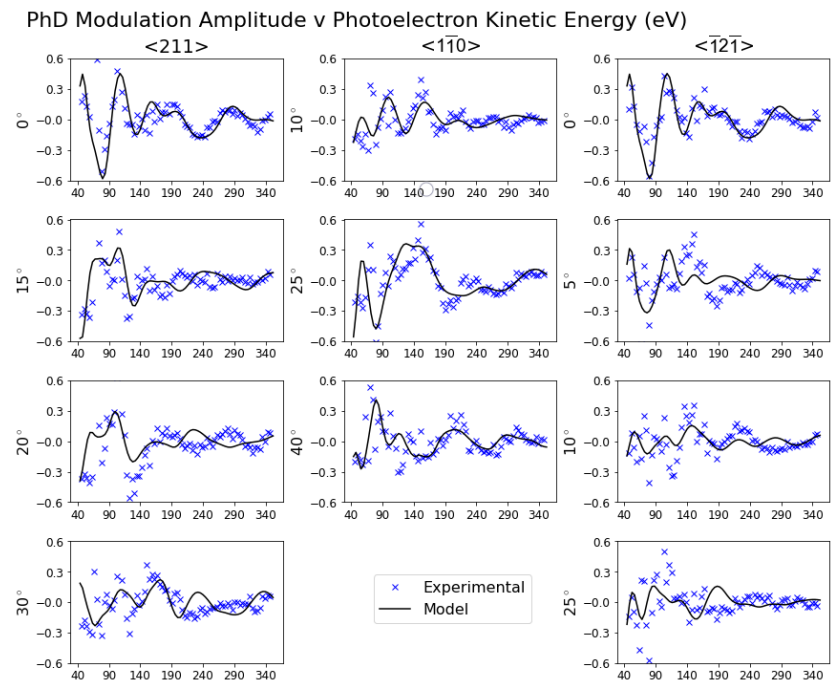


Figure A.1: PhD modulations of PSO optimised structure of 1H full structure overlayed onto experimental modulations of molybdenum at varying polar angle (y label) and crystallographic direction (x label).

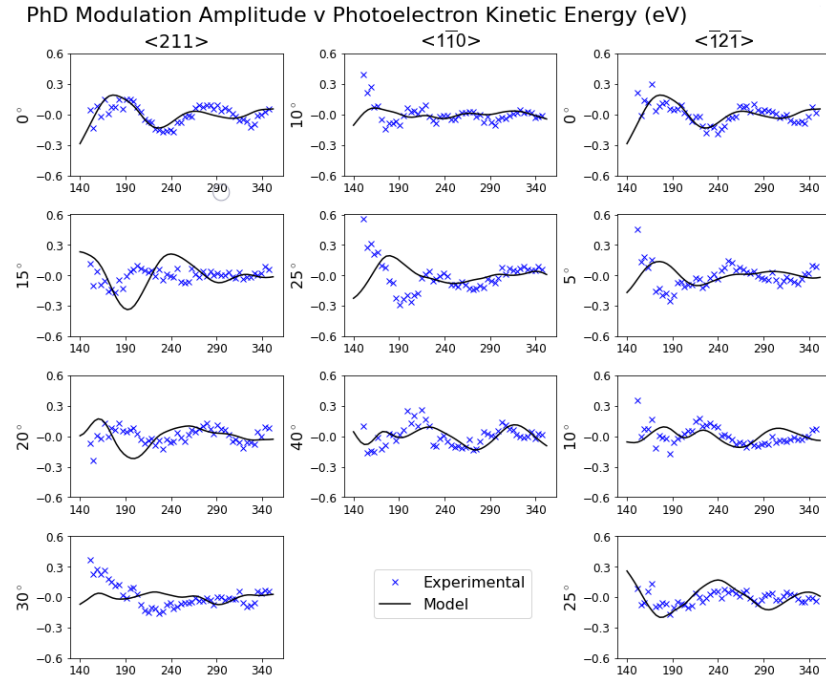


Figure A.2: PhD modulations of PSO optimised structure of 1T full structure overlayed onto experimental modulations of molybdenum at varying polar angle (y label) and crystallographic direction (x label).

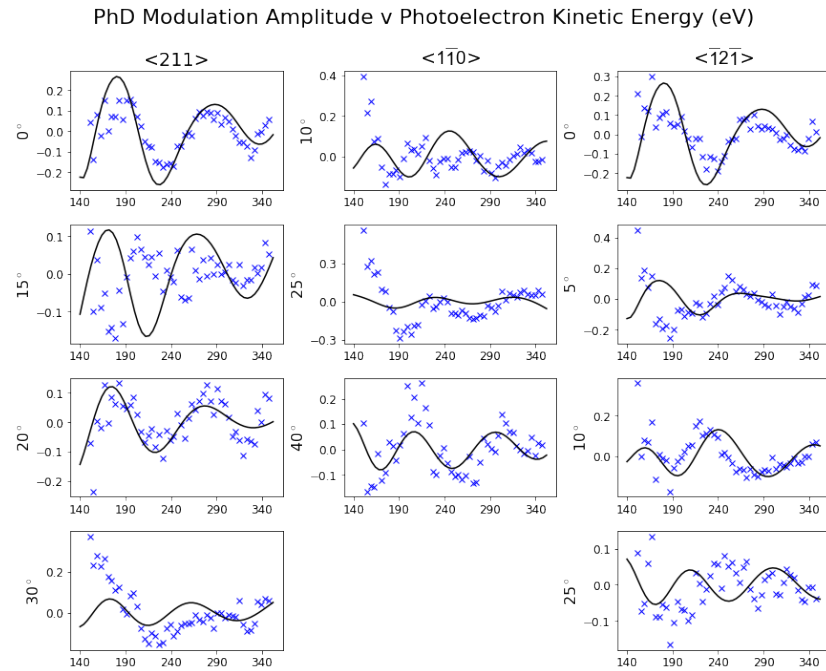


Figure A.3: PhD modulations of PSO optimised structure of the MoS_2 trimer overlayed onto experimental modulations of molybdenum at varying polar angle (y label) and crystallographic direction (x label).

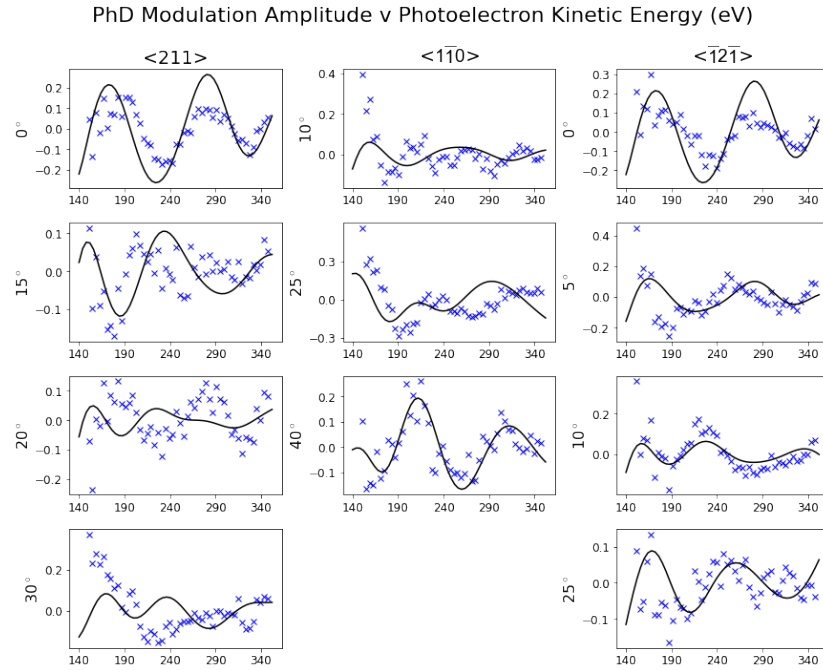


Figure A.4: PhD modulations of PSO optimised structure of 1H hexamer overlayed onto experimental modulations of molybdenum at varying polar angle (y label) and crystallographic direction (x label).

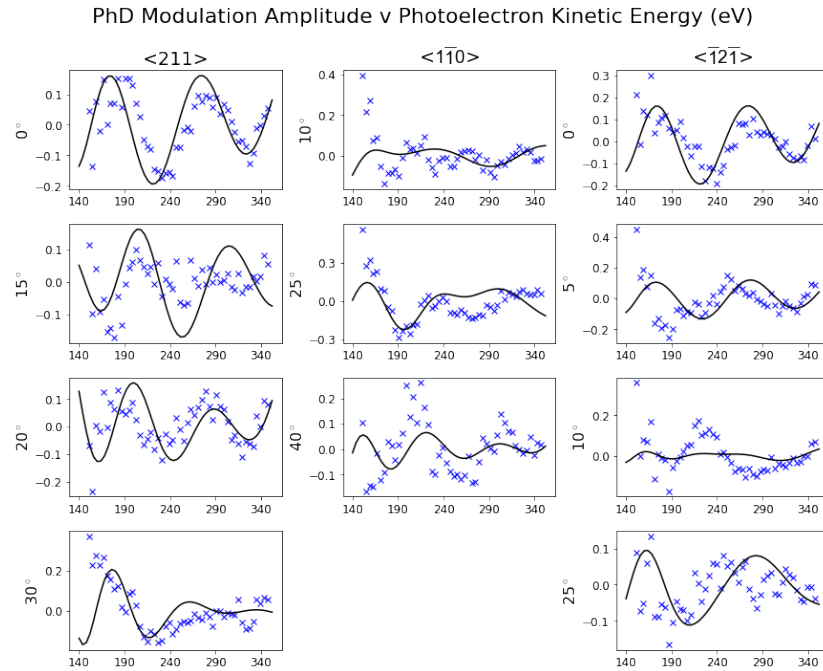


Figure A.5: PhD modulations of PSO optimised structure of 1T hexamer overlayed onto experimental modulations of molybdenum at varying polar angle (y label) and crystallographic direction (x label).

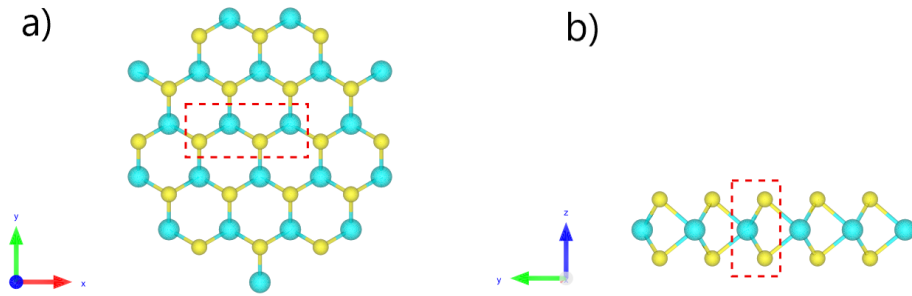


Figure A.6: Diagram showing the section of the 1H full structure that is modelled by the 1H hexamer

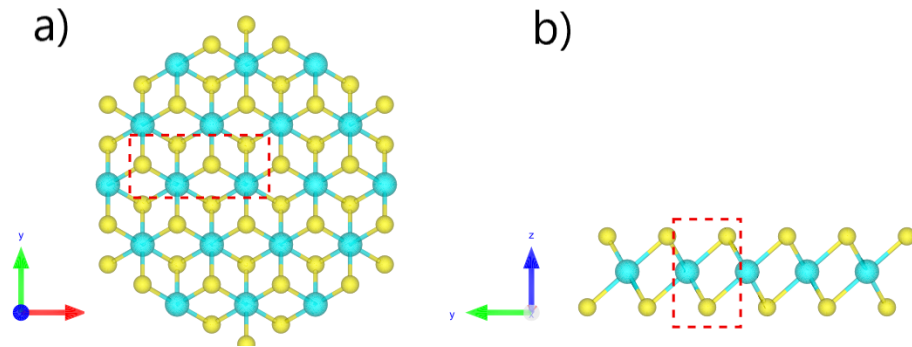


Figure A.7: Diagram showing the section of the 1T full structure that is modelled by the 1T hexamer

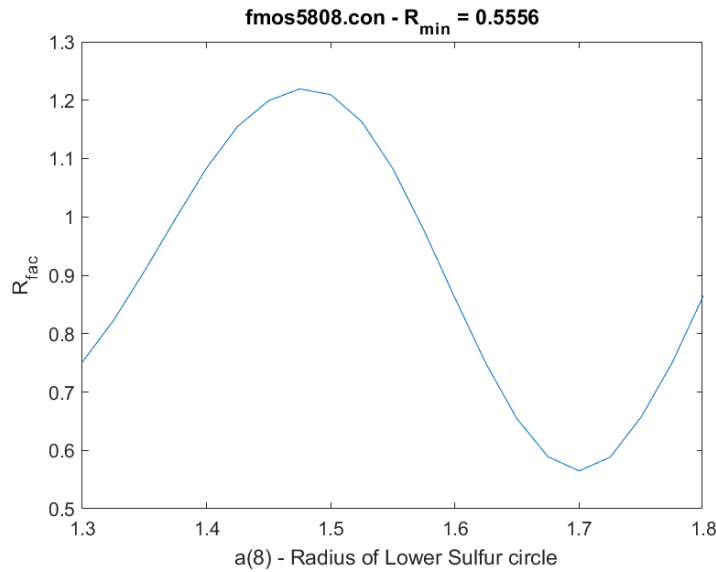


Figure A.8: Plot of R-Factor with respect to lower S radius for the 1H hexamer model, where S lower radius is R_2 within the hexamer model diagram of **Figure 5.12**. The other parameters for this model were a bond angle of 174° , a Mo - Mo separation of 3.34 \AA , and a bond length of 1.70 \AA for upper sulfurs.

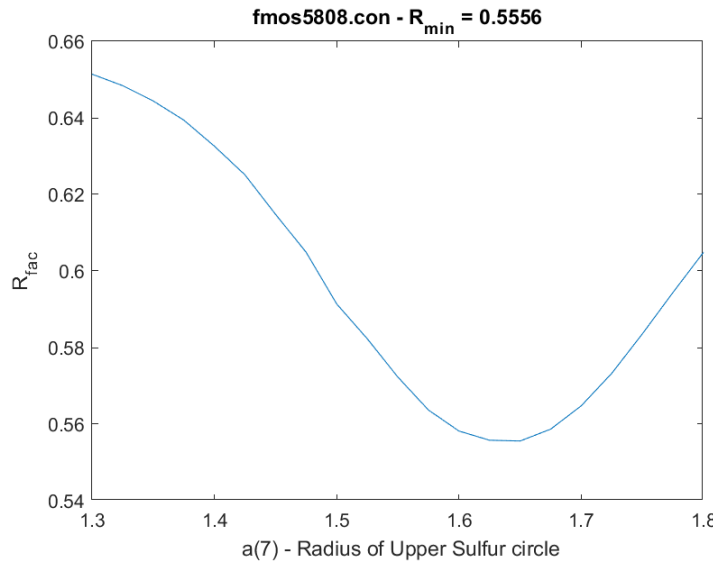


Figure A.9: Plot of R-Factor with respect to upper S radius for the 1H hexamer model, where S lower radius is R_2 within the hexamer model diagram of **Figure 5.12**. The other parameters for this model were a bond angle of 174° , a Mo - Mo separation of 3.34 \AA , and a bond length of 1.66 \AA for lower sulfurs.

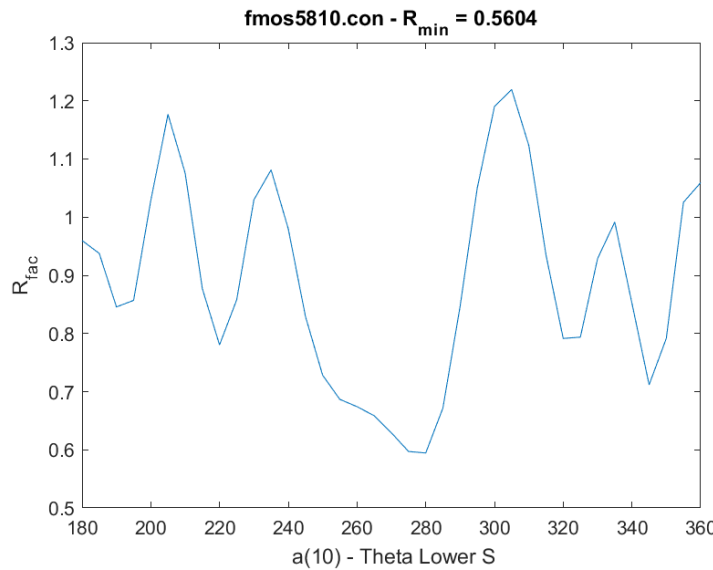


Figure A.10: Plot of R-Factor with respect to lower S angle for the 1H hexamer model, where theta lower is θ_2 within the hexamer model diagram of **Figure 5.12**. The other parameters for this model were a upper S angle of 95° , a Mo - Mo separation of 3.34 \AA , and a bond length of 1.66 \AA for lower sulfurs.

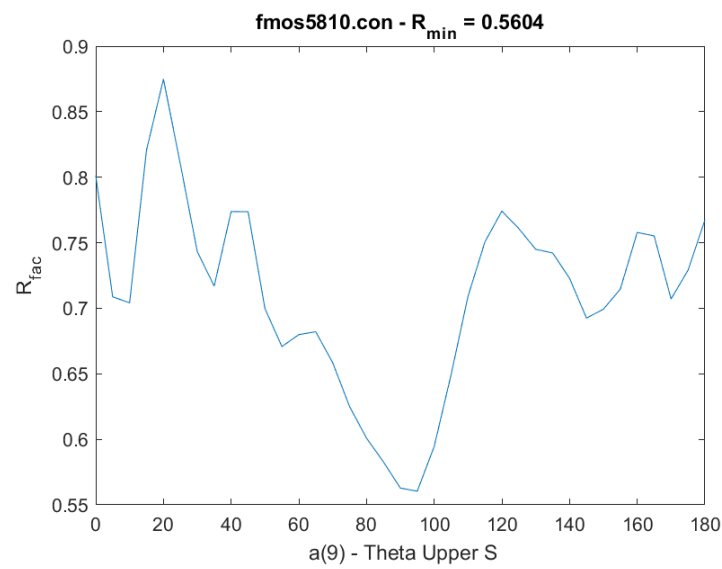


Figure A.11: Plot of R-Factor with respect to upper S angle for the 1H hexamer model, where theta upper is θ_1 within the hexamer model diagram of **Figure 5.12**. The other parameters for this model were a lower S angle of 280° , a Mo - Mo separation of 3.34 \AA , and a bond length of 1.66 \AA for lower sulfurs.

Bibliography

- [1] Caio Silva, Daniela Dombrowski, Nicolae Atodiresei, Wouter Jolie, Ferdinand Hagen, Jiaqi Cai, Paul Ryan, Pardeep Thakur, Vasile Caciuc, Stefan Blügel, David Duncan, Thomas Michely, Tien-Lin Lee, and Carsten Busse. Spatial variation of geometry, binding, and electronic properties in the moiré superstructure of mos 2 on au(111). *2D Materials*, 9, 01 2022.
- [2] Matthew Coz, Hugo Shiers, Andrew Miller, and Richard Howard. *Dimaond Vacuum System Manual*. Diamond Light Source Ltd Diamond House Harwell Science and Innovation Campus Didcot Oxfordshire OX11 0DE United Kingdom, 2019.
- [3] Tien-Lin Lee and David A Duncan. A two-color beamline for electron spectroscopies at diamond light source. *Synchrotron Radiation News*, 31(4):16–22, 2018.
- [4] M. P. Seah and W. A. Dench. Quantitative electron spectroscopy of surfaces: A standard data base for electron inelastic mean free paths in solids. *Surface and Interface Analysis*, 1(1):2–11, 1979.
- [5] Stefano Gottardi, Kathrin Muller, Luca Bignardi, Juan Carlos Moreno Lopez, Tuan Anh Pham, Oleksii Ivashenko, Mikhail Yablonskikh, Alexei Barinov, Jonas Bjork, Petra Rudolf, et al. Comparing graphene growth on cu (111) versus oxidized cu (111). *Nano letters*, 15(2):917–922, 2015.
- [6] Benedikt P Klein, Nadine J Van Der Heijden, Stefan R Kachel, Markus Franke, Claudio K Krug, Katharina K Greulich, Lukas Ruppenthal, Philipp Müller, Phil Rosenow, Shayan Parhizkar, et al. Molecular topology and the surface chemical bond: alternant versus nonalternant aromatic systems as functional structural elements. *Physical Review X*, 9(1):011030, 2019.
- [7] Dhananjay I Patel, Brian I Johnson, Dhruv Shah, Neal Fairley, and Matthew R Linford. Xps peak fitting.
- [8] DP Woodruff. Surface structure determination using x-ray standing waves. *Reports on Progress in Physics*, 68(4):743, 2005.

- [9] DP Woodruff. Adsorbate structure determination using photoelectron diffraction: Methods and applications. *Surface Science Reports*, 62(1):1–38, 2007.
- [10] D.A. Duncan. Adsorbate structure determination using energy scanned photoelectron diffraction. *Thesis*, 2012.
- [11] Xiao-Feng Yang, Aiqin Wang, Botao Qiao, Jun Li, Jingyue Liu, and Tao Zhang. Single-atom catalysts: a new frontier in heterogeneous catalysis. *Accounts of chemical research*, 46(8):1740–1748, 2013.
- [12] Niels R Walet. Advanced quantum mechanics 2: Graphene.
- [13] Paul McEuen and C Kittel. Introduction to solid state physics. 2005.
- [14] Florian Banhart, Jani Kotakoski, and Arkady V. Krasheninnikov. Structural defects in graphene. *ACS Nano*, 5(1):26–41, 2011. PMID: 21090760.
- [15] Harold W Kroto, James R Heath, Sean C O’Brien, Robert F Curl, and Richard E Smalley. C₆₀: Buckminsterfullerene. *nature*, 318(6042):162–163, 1985.
- [16] Sumio Iijima. Helical microtubules of graphitic carbon. *nature*, 354(6348):56–58, 1991.
- [17] K. S. Novoselov, A. K. Geim, S. V. Morozov, D. Jiang, Y. Zhang, S. V. Dubonos, I. V. Grigorieva, and A. A. Firsov. Electric field effect in atomically thin carbon films. *Science*, 306(5696):666–669, 2004.
- [18] Deepika Gupta, Vishnu Chauhan, and Rajesh Kumar. A comprehensive review on synthesis and applications of molybdenum disulfide (mos₂) material: Past and recent developments. *Inorganic Chemistry Communications*, 121:108200, 2020.
- [19] Philip Moriarty. Nanostructured materials. *Reports on Progress in Physics*, 64(3):297–381, feb 2001.
- [20] Qu Yue, Shengli Chang, Jun Kang, Xueao Zhang, Zhengzheng Shao, Shiqiao Qin, and Jingbo Li. Bandgap tuning in armchair mos₂ nanoribbon. *Journal of physics: condensed matter*, 24(33):335501, 2012.
- [21] Ruben Mas-Balleste, Cristina Gomez-Navarro, Julio Gomez-Herrero, and Felix Zamora. 2d materials: to graphene and beyond. *Nanoscale*, 3(1):20–30, 2011.
- [22] Yang Guo, Bin Li, Yuan Huang, Shuo Du, Chi Sun, Hailan Luo, Baoli Liu, Xingjiang Zhou, Jinlong Yang, Junjie Li, et al. Direct bandgap engineering with local biaxial strain in few-layer mos₂ bubbles. *Nano Research*, 13(8):2072–2078, 2020.

- [23] R Mas-Balleste, C Gomez-Navarro, and F Gomez-Herrero, Zamora. 2d materials: to graphene and beyond. *Nanoscale*, 3:20, 2011.
- [24] D. Phil Woodruff. *Modern Techniques of Surface Science*. Cambridge University Press, 3 edition, 2016.
- [25] Kurt W. Kolasinski. *Experimental Probes and Techniques*, page 51–111. Wiley, 3 edition, 2020.
- [26] J Kelly, T Lee, S Alcock, and H Patel. Design, build & test of a double crystal monochromator for beamlines i09 & i23 at the diamond light source. In *Journal of Physics: Conference Series*, volume 425, page 052009. IOP Publishing, 2013.
- [27] Ernesto Paparazzo. *Electron energy loss spectroscopy in the electron microscope*. Elsevier, 2005.
- [28] VM Dwyer and JAD Matthew. The effect of elastic scattering on the effective inelastic mean free path. *Vacuum*, 33(10-12):767–769, 1983.
- [29] Clinton Davisson and Lester H Germer. Diffraction of electrons by a crystal of nickel. *Physical review*, 30(6):705, 1927.
- [30] DR Symes, JM Cole, JC Wood, SPD Mangles, and Z Najmudin. Comparison of the properties of laser-driven x-ray sources to existing compact x-ray sources.
- [31] P. H. Citrin and D. R. Hamann. Phonon broadening of x-ray photoemission line shapes in solids and its independence of hole state lifetimes. *Phys. Rev. B*, 15:2923–2928, Mar 1977.
- [32] George H Major, Neal Fairley, Peter MA Sherwood, Matthew R Linford, Jeff Terry, Vincent Fernandez, and Kateryna Artyushkova. Practical guide for curve fitting in x-ray photoelectron spectroscopy. *Journal of Vacuum Science & Technology A: Vacuum, Surfaces, and Films*, 38(6):061203, 2020.
- [33] Woldemar Voigt. Über das gesetz der intensitätsverteilung innerhalb der linien eines gasspektrums, 1912.
- [34] Sunjic Doniach and M Sunjic. Many-electron singularity in x-ray photoemission and x-ray line spectra from metals. *Journal of Physics C: Solid State Physics*, 3(2):285, 1970.
- [35] Boris W Batterman and Henderson Cole. Dynamical diffraction of x rays by perfect crystals. *Reviews of modern physics*, 36(3):681, 1964.

- [36] DP Woodruff, DL Seymour, Christopher F McConville, CE Riley, MD Crapper, NP Prince, and Robert G Jones. A simple x-ray standing wave technique for surface structure determination-theory and an application. *Surface Science*, 195(1-2):237–254, 1988.
- [37] DP Woodruff. Normal incidence x-ray standing wave determination of adsorbate structures. *Progress in surface science*, 57(1):1–60, 1998.
- [38] DP Woodruff. Analysis of photoelectron diffraction spectra using single scattering simulations. *Surface Science*, 166(2-3):377–390, 1986.
- [39] John J Barton. Photoelectron holography. *Physical review letters*, 61(12):1356, 1988.
- [40] A Szoke. Short wavelength coherent radiation: generation and applications. 147:361, 1986.
- [41] V Fritzsche. A new spherical-wave approximation for photoelectron diffraction, exafs and meed. *Journal of Physics: Condensed Matter*, 2(6):1413, 1990.
- [42] V Fritzsche and P Rennert. A reduced angular momentum expansion in the multiple-scattering theory. *physica status solidi (b)*, 135(1):49–60, 1986.
- [43] V Fritzsche. Consequences of a finite energy resolution for photoelectron diffraction spectra. *Surface science*, 265(1-3):187–195, 1992.
- [44] V Fritzsche. Approximations for the scattering of excited electrons in solids. *physica status solidi (b)*, 147(2):485–494, 1988.
- [45] D.A. Duncan, J.I.J. Choi, and D.P. Woodruff. Global search algorithms in surface structure determination using photoelectron diffraction. *Surface Science*, 606(3):278–284, 2012.
- [46] JB Pendry. Reliability factors for leed calculations. *Journal of Physics C: Solid State Physics*, 13(5):937, 1980.
- [47] NA Booth, R Davis, R Toomes, DP Woodruff, C Hirschmugl, Karl-Michael Schindler, Oliver Schaff, V Fernandez, Andreas Theobald, Ph Hofmann, et al. Structure determination of ammonia on cu (110)—a low-symmetry adsorption site. *Surface science*, 387(1-3):152–159, 1997.
- [48] A Pancotti, N Barrett, LF Zagonel, and GM Vanacore. Multiple scattering x-ray photoelectron diffraction study of the srtio 3 (100) surface. *Journal of Applied Physics*, 106(3):034104, 2009.
- [49] Maurice Clerc. *Particle swarm optimization*, volume 93. John Wiley & Sons, 2010.

- [50] Von B Nascimento, VE De Carvalho, CMC De Castilho, BV da Costa, and EA Soares. The fast simulated annealing algorithm applied to the search problem in leed. *Surface Science*, 487(1-3):15–27, 2001.
- [51] M. Kottcke and K. Heinz. A new approach to automated structure optimization in leed intensity analysis. *Surface Science*, 376(1):352–366, 1997.
- [52] Gerd Binnig, Heinrich Rohrer, Ch Gerber, and Eddie Weibel. Tunneling through a controllable vacuum gap. *Applied Physics Letters*, 40(2):178–180, 1982.
- [53] Donald M Eigler and Erhard K Schweizer. Positioning single atoms with a scanning tunnelling microscope. *Nature*, 344(6266):524–526, 1990.
- [54] Wolfgang Moritz, B Wang, M-L Bocquet, T Brugger, T Greber, J Wintterlin, and S Günther. Structure determination of the coincidence phase of graphene on ru (0001). *Physical review letters*, 104(13):136102, 2010.
- [55] Esin Soy, Zhu Liang, and Michael Trenary. Formation of pt and rh nanoclusters on a graphene moiré pattern on cu(111). *The Journal of Physical Chemistry C*, 119(44):24796–24803, 2015.
- [56] Botao Qiao, Aiqin Wang, Xiaofeng Yang, Lawrence F Allard, Zheng Jiang, Yitao Cui, Jingyue Liu, Jun Li, and Tao Zhang. Single-atom catalysis of co oxidation using pt 1/feo x. *Nature chemistry*, 3(8):634–641, 2011.
- [57] Rui Lang, Tianbo Li, Daiju Matsumura, Shu Miao, Yujing Ren, Yi-Tao Cui, Yuan Tan, Botao Qiao, Lin Li, Aiqin Wang, et al. Hydroformylation of olefins by a rhodium single-atom catalyst with activity comparable to rhcl (pph3) 3. *Angewandte Chemie International Edition*, 55(52):16054–16058, 2016.
- [58] Chee Kok Poh, San Hua Lim, Jianyi Lin, and Yuan Ping Feng. Tungsten carbide supports for single-atom platinum-based fuel-cell catalysts: first-principles study on the metal–support interactions and o₂ dissociation on w x c low-index surfaces. *The Journal of Physical Chemistry C*, 118(25):13525–13538, 2014.
- [59] Shuhui Sun, Gaixia Zhang, Nicolas Gauquelin, Ning Chen, Jigang Zhou, Songlan Yang, Weifeng Chen, Xiangbo Meng, Dongsheng Geng, Mohammad N Banis, et al. Single-atom catalysis using pt/graphene achieved through atomic layer deposition. *Scientific reports*, 3(1):1–9, 2013.
- [60] Anu Baby, Laura Trovato, and Cristiana Di Valentin. Single atom catalysts (sac) trapped in defective and nitrogen-doped graphene supported on metal substrates. *Carbon*, 174:772–788, 2021.

- [61] N David Mermin and Herbert Wagner. Absence of ferromagnetism or antiferromagnetism in one-or two-dimensional isotropic heisenberg models. *Physical Review Letters*, 17(22):1133, 1966.
- [62] Jian-Hao Chen, Chaun Jang, Shudong Xiao, Masa Ishigami, and Michael S Fuhrer. Intrinsic and extrinsic performance limits of graphene devices on sio2. *Nature nanotechnology*, 3(4):206–209, 2008.
- [63] Alexander A Balandin, Suchismita Ghosh, Wenzhong Bao, Irene Calizo, Desalegne Teweldebrhan, Feng Miao, and Chun Ning Lau. Superior thermal conductivity of single-layer graphene. *Nano letters*, 8(3):902–907, 2008.
- [64] Changgu Lee, Xiaoding Wei, Jeffrey W Kysar, and James Hone. Measurement of the elastic properties and intrinsic strength of monolayer graphene. *science*, 321(5887):385–388, 2008.
- [65] Si Zhou and Angelo Bongiorno. Origin of the chemical and kinetic stability of graphene oxide. *Scientific reports*, 3(1):1–7, 2013.
- [66] Lipei Fu, Kaili Liao, Bo Tang, Lujun Jiang, and Weiqiu Huang. Applications of graphene and its derivatives in the upstream oil and gas industry: A systematic review. *Nanomaterials*, 10(6):1013, 2020.
- [67] University of Sheffield Mark Winter and WebElements Ltd. Copper: Crystal structures.
- [68] L Li, S Reich, and J Robertson. Defect energies of graphite: Density-functional calculations. *Physical Review B*, 72(18):184109, 2005.
- [69] Sondes Karoui, Hakim Amara, Christophe Bichara, and François Ducastelle. Nickel-assisted healing of defective graphene. *ACS nano*, 4(10):6114–6120, 2010.
- [70] AV Krasheninnikov, PO Lehtinen, AS Foster, and RM Nieminen. Bending the rules: Contrasting vacancy energetics and migration in graphite and carbon nanotubes. *Chemical Physics Letters*, 418(1-3):132–136, 2006.
- [71] JC Hamilton and SM Foiles. First-principles calculations of grain boundary theoretical shear strength using transition state finding to determine generalized gamma surface cross sections. *Physical Review B*, 65(6):064104, 2002.
- [72] Gregory Mills, Hannes Jónsson, and Gregory K Schenter. Reversible work transition state theory: application to dissociative adsorption of hydrogen. *Surface Science*, 324(2-3):305–337, 1995.

- [73] Martin Amft, Biplab Sanyal, Olle Eriksson, and Natalia Skorodumova. Small gold clusters on graphene, their mobility and clustering: A dft study. *Journal of physics. Condensed matter : an Institute of Physics journal*, 23:205301, 05 2011.
- [74] A.J. Stone and D.J. Wales. Theoretical studies of icosahedral c₆₀ and some related species. *Chemical Physics Letters*, 128(5):501–503, 1986.
- [75] Oleg V. Yazyev, Ivano Tavernelli, Ursula Rothlisberger, and Lothar Helm. Early stages of radiation damage in graphite and carbon nanostructures: A first-principles molecular dynamics study. *Phys. Rev. B*, 75:115418, Mar 2007.
- [76] Sondes Karoui, Hakim Amara, Christophe Bichara, and François Ducastelle. Nickel-assisted healing of defective graphene. *ACS nano*, 4(10):6114–6120, 2010.
- [77] H. W. Kroto, J. R. Heath, S. C. O'Brien, R. F. Curl, and R. E. Smalley. C₆₀: Buckminsterfullerene. *Nature*, 318(6042):162–163, Nov 1985.
- [78] A.V. Krasheninnikov, P.O. Lehtinen, A.S. Foster, and R.M. Nieminen. Bending the rules: Contrasting vacancy energetics and migration in graphite and carbon nanotubes. *Chemical Physics Letters*, 418(1):132–136, 2006.
- [79] Ovidiu Cretu, Arkady V Krasheninnikov, Julio A Rodríguez-Manzo, Litao Sun, Risto M Nieminen, and Florian Banhart. Migration and localization of metal atoms on strained graphene. *Physical review letters*, 105(19):196102, 2010.
- [80] A. V. Krasheninnikov, P. O. Lehtinen, A. S. Foster, P. Pyykkö, and R. M. Nieminen. Embedding transition-metal atoms in graphene: Structure, bonding, and magnetism. *Phys. Rev. Lett.*, 102:126807, Mar 2009.
- [81] DW Boukhvalov and MI Katsnelson. Chemical functionalization of graphene with defects. *Nano letters*, 8(12):4373–4379, 2008.
- [82] Raphael Mmaduka Obodo, Ishaq Ahmad, and Fabian Ifeanyichukwu Ezema. Introductory chapter: Graphene and its applications. In Ishaq Ahmad and Fabian I. Ezema, editors, *Graphene and Its Derivatives*, chapter 1. IntechOpen, Rijeka, 2019.
- [83] L. Miglio and A. Sassella. Epitaxy. In Franco Bassani, Gerald L. Liedl, and Peter Wyder, editors, *Encyclopedia of Condensed Matter Physics*, pages 157–166. Elsevier, Oxford, 2005.
- [84] Chapter 1 - deposition technologies: An overview. In Peter M. Martin, editor, *Handbook of Deposition Technologies for Films and Coatings (Third Edition)*, pages 1–31. William Andrew Publishing, Boston, third edition edition, 2010.

- [85] Choon-Ming Seah, Siang-Piao Chai, and Abdul Rahman Mohamed. Mechanisms of graphene growth by chemical vapour deposition on transition metals. *Carbon*, 70:1–21, 2014.
- [86] G.A. López and E.J. Mittemeijer. The solubility of c in solid cu. *Scripta Materialia*, 51(1):1–5, 2004.
- [87] Oleg V. Yazyev and Alfredo Pasquarello. Effect of metal elements in catalytic growth of carbon nanotubes. *Phys. Rev. Lett.*, 100:156102, Apr 2008.
- [88] M. H. Zwietering, I. Jongenburger, F. M. Rombouts, and K. van 't Riet. Modeling of the bacterial growth curve. *Applied and environmental microbiology*, 56(6):1875–1881, Jun 1990. 16348228[pmid].
- [89] Johannes Halle, Alexander Mehler, Nicolas Néel, and Jörg Kröger. Preparation of graphene bilayers on platinum by sequential chemical vapour deposition. *Phys. Chem. Chem. Phys.*, 21:3140–3144, 2019.
- [90] University of Sheffield Mark Winter and WebElements Ltd. Copper: Crystal structures.
- [91] Martin Schmid. Wavemetrics.
- [92] Li Gao, Jeffrey R Guest, and Nathan P Guisinger. Epitaxial graphene on cu (111). *Nano letters*, 10(9):3512–3516, 2010.
- [93] Stoodley. M Klein. B. Azupyrene. 2022.
- [94] Benedikt P Klein, Alexander Ihle, Stefan R Kachel, Lukas Ruppenthal, Samuel J Hall, Lars Sattler, Sebastian M Weber, Jan Herritsch, Andrea Jaegermann, Daniel Ebeling, et al. Topological stone–wales defects enhance bonding and electronic coupling at the graphene/metal interface. *ACS nano*, 2022.
- [95] Benedikt P Klein, Juliana M Morbec, Markus Franke, Katharina K Greulich, Malte Sachs, Shayan Parhizkar, Francois C Bocquet, Martin Schmid, Samuel J Hall, Reinhard J Maurer, et al. Molecule–metal bond of alternant versus nonalternant aromatic systems on coinage metal surfaces: Naphthalene versus azulene on ag (111) and cu (111). *The Journal of Physical Chemistry C*, 123(48):29219–29230, 2019.
- [96] Moore More. International roadmap for devices and systems (irds), 2021.
- [97] Y. P. Venkata Subbaiah, K. J. Saji, and A. Tiwari. Atomically thin mos₂: A versatile nongraphene 2d material. *Advanced Functional Materials*, 26(13):2046–2069, 2016.

- [98] Sajedeh Manzeli, Dmitry Ovchinnikov, Diego Pasquier, Oleg V Yazyev, and Andras Kis. 2d transition metal dichalcogenides. *Nature Reviews Materials*, 2(8):1–15, 2017.
- [99] Shaswat Barua, Hemant Sankar Dutta, Satyabrat Gogoi, Rashmita Devi, and Raju Khan. Nanostructured mos2-based advanced biosensors: a review. *ACS Applied Nano Materials*, 1(1):2–25, 2017.
- [100] Sohail Ahmad and Sugata Mukherjee. A comparative study of electronic properties of bulk mos2 and its monolayer using dft technique: application of mechanical strain on mos2 monolayer. 2014.
- [101] K. S. Novoselov, D. Jiang, F. Schedin, T. J. Booth, V. V. Khotkevich, S. V. Morozov, and A. K. Geim. Two-dimensional atomic crystals. *Proceedings of the National Academy of Sciences*, 102(30):10451–10453, 2005.
- [102] Eugene S Kadantsev and Paweł Hawrylak. Electronic structure of a single mos2 monolayer. *Solid state communications*, 152(10):909–913, 2012.
- [103] E. Gourmelon, O. Lignier, H. Hadouda, G. Couturier, J.C. Bernède, J. Tedd, J. Pouzet, and J. Salardenne. Ms2 ($m = w, mo$) photosensitive thin films for solar cells. *Solar Energy Materials and Solar Cells*, 46(2):115–121, 1997.
- [104] A. L. Santhosha, Prasant Kumar Nayak, Kilian Pollok, Falko Langenhorst, and Philipp Adelhelm. Exfoliated mos2 as electrode for all-solid-state rechargeable lithium-ion batteries. *The Journal of Physical Chemistry C*, 123(19):12126–12134, May 2019.
- [105] Mohammad R. Vazirisereshk, Ashlie Martini, David A. Strubbe, and Mehmet Z. Baykara. Solid lubrication with mos2: A review. *Lubricants*, 7(7), 2019.
- [106] Agnieszka Kuc and Thomas Heine. The electronic structure calculations of two-dimensional transition-metal dichalcogenides in the presence of external electric and magnetic fields. *Chem. Soc. Rev.*, 44:2603–2614, 2015.
- [107] Fanglue Wu, Zhuotong Liu, Nathaniel Hawthorne, Michael Chandross, Quentarius Moore, Nicolas Argibay, John F. Curry, and James D. Batteas. Formation of coherent 1h–1t heterostructures in single-layer mos2 on au(111). *ACS Nano*, 14(12):16939–16950, 2020. PMID: 33253530.
- [108] Xiaoyan Guo, Guohui Yang, Junfeng Zhang, and Xiaohong Xu. Structural, mechanical and electronic properties of in-plane 1t/2h phase interface of mos2 heterostructures. *AIP Advances*, 5(9):097174, 2015.

- [109] Matteo Calandra. Chemically exfoliated single-layer mos 2: Stability, lattice dynamics, and catalytic adsorption from first principles. *Physical Review B*, 88(24):245428, 2013.
- [110] Andrey N. Enyashin, Lena Yadgarov, Lothar Houben, Igor Popov, Marc Weidenbach, Reshef Tenne, Maya Bar-Sadan, and Gotthard Seifert. New route for stabilization of 1t-ws2 and mos2 phases. *The Journal of Physical Chemistry C*, 115(50):24586–24591, 2011.
- [111] Xiaoyan Guo, Guohui Yang, Junfeng Zhang, and Xiaohong Xu. Structural, mechanical and electronic properties of in-plane 1t/2h phase interface of mos2 heterostructures. *AIP Advances*, 5(9):097174, 2015.
- [112] Arnulf Maeland and Ted B. Flanagan. Lattice spacings of gold–palladium alloys. *Canadian Journal of Physics*, 42(11):2364–2366, 1964.
- [113] J.A. Wilson and A.D. Yoffe. The transition metal dichalcogenides discussion and interpretation of the observed optical, electrical and structural properties. *Advances in Physics*, 18(73):193–335, 1969.
- [114] Signe G Sørensen, Henrik G Füchtbauer, Anders K Tuxen, Alex S Walton, and Jeppe V Lauritsen. Structure and electronic properties of in situ synthesized single-layer mos2 on a gold surface. *ACS nano*, 8(7):6788–6796, 2014.
- [115] Harsh Bana, Elisabetta Travaglia, Luca Bignardi, Paolo Lacovig, Charlotte E Sanders, Maciej Dendzik, Matteo Michiardi, Marco Bianchi, Daniel Lizzit, Francesco Presel, et al. Epitaxial growth of single-orientation high-quality mos2 monolayers. *2D Materials*, 5(3):035012, 2018.
- [116] Jill A. Miwa, Søren Ulstrup, Signe G. Sørensen, Maciej Dendzik, Antonija Grubišić Čabo, Marco Bianchi, Jeppe Vang Lauritsen, and Philip Hofmann. Electronic structure of epitaxial single-layer mos₂. *Phys. Rev. Lett.*, 114:046802, Jan 2015.
- [117] Anubhav Jain, Shyue Ping Ong, Geoffroy Hautier, Wei Chen, William Davidson Richards, Stephen Dacek, Shreyas Cholia, Dan Gunter, David Skinner, Gerbrand Ceder, et al. Commentary: The materials project: A materials genome approach to accelerating materials innovation. *APL materials*, 1(1):011002, 2013.
- [118] Cedric J Powell, Aleksander Jablonski, Francesc Salvat, Angela Y Lee, et al. Nist electron elastic-scattering cross-section database, version 4.0. 2016.
- [119] Imam Abdul Rahman and Acep Purqon. First principles study of molybdenum disulfide electronic structure. In *Journal of Physics: Conference Series*, volume 877, page 012026. IOP Publishing, 2017.

- [120] Daeho Kim, Dezheng Sun, Wenhao Lu, Zhihai Cheng, Yeming Zhu, Duy Le, Talat S Rahman, and Ludwig Bartels. Toward the growth of an aligned single-layer mos2 film. *Langmuir*, 27(18):11650–11653, 2011.
- [121] Xinyue Lin, Wentong Li, Yingying Dong, Chen Wang, Qi Chen, and Hui Zhang. Two-dimensional metallic mos2: A dft study. *Computational Materials Science*, 124:49–53, 2016.
- [122] Wei Zhao, Jie Pan, Yuqiang Fang, Xiangli Che, Dong Wang, Kejun Bu, and Fuqiang Huang. Metastable mos2: crystal structure, electronic band structure, synthetic approach and intriguing physical properties. *Chemistry—A European Journal*, 24(60):15942–15954, 2018.
- [123] Luis Henrique de Lima, Thomas Greber, and Matthias Muntwiler. The true corrugation of a h.bn nanomesh layer. *2D Materials*, 7(3):035006, 2020.